

8-7-2020

Effects of Surfactants on the Generation of Sea Spray During Tropical Cyclones

Breanna L. Vanderplow
Nova Southeastern University

Follow this and additional works at: https://nsuworks.nova.edu/hcas_etd_all



Part of the [Fluid Dynamics Commons](#), [Marine Biology Commons](#), and the [Oceanography Commons](#)

Share Feedback About This Item

NSUWorks Citation

Breanna L. Vanderplow. 2020. *Effects of Surfactants on the Generation of Sea Spray During Tropical Cyclones*. Master's thesis. Nova Southeastern University. Retrieved from NSUWorks, . (12)
https://nsuworks.nova.edu/hcas_etd_all/12.

This Thesis is brought to you by the HCAS Student Theses and Dissertations at NSUWorks. It has been accepted for inclusion in All HCAS Student Capstones, Theses, and Dissertations by an authorized administrator of NSUWorks. For more information, please contact nsuworks@nova.edu.

Thesis of Breanna L. Vanderplow

Submitted in Partial Fulfillment of the Requirements for the Degree of

Master of Science Marine Science

Nova Southeastern University
Halmos College of Arts and Sciences

August 2020

Approved:
Thesis Committee

Major Professor: Alexander Soloviev, Ph.D.

Committee Member: Richard Dodge, Ph.D.

Committee Member: William Perrie, Ph.D.

Committee Member: Roger Lukas, Ph.D.

NOVA SOUTHEASTERN UNIVERSITY
HALMOS COLLEGE OF ARTS AND SCIENCES

EFFECTS OF SURFACTANTS ON THE GENERATION OF SEA SPRAY
DURING TROPICAL CYCLONES

By

Breanna Vanderplow

Submitted to the Faculty of
Halmos College of Arts and Sciences
in partial fulfillment of the requirements for
the degree of Master of Science with a specialty in:

Marine Science

Nova Southeastern University

September 8 2020

Table of Contents

<i>List of Figures</i>	4
<i>List of Tables</i>	6
<i>List of Equations</i>	6
<i>Abstract</i>	8
<i>Acknowledgements</i>	9
1. Introduction	10
<i>a. Tropical Cyclones</i>	10
<i>b. Tropical Cyclone Intensification</i>	12
<i>c. Multiscale Physics at the Air-sea Interface Under Tropical Cyclone Conditions</i>	16
<i>d. Sea Spray and Spume Generation</i>	17
<i>e. Tropical Cyclone Prediction</i>	21
<i>f. Surfactants</i>	25
2. Hypotheses	28
3. Statement of Objectives	29
4. Methods	29
<i>a. Laboratory Experiment</i>	29
<i>b. ANSYS Fluent CFD Model Theory</i>	31
<i>i. Large Eddy Simulation</i>	31
<i>ii. Volume of Fluid</i>	35
<i>iii. Discrete Phase Model</i>	38
<i>iv. VOF-to-DPM</i>	39
<i>v. Model Setup</i>	40
<i>c. Data Analysis</i>	42
<i>d. Satellite Imagery</i>	45
5. Results and Discussion	47
<i>a. Laboratory Experiment</i>	47
<i>b. Volume of Fluid to Discrete Phase Model</i>	48
<i>c. Confirmation of VOF-to-DPM with Laboratory Experiments</i>	53
<i>d. Satellite Imagery</i>	65
6. Conclusions	83
7. References	84
9. Supplementary Material	95

List of Figures

Figure 1. Anatomy of a tropical cyclone.....	11
Figure 2. Hurricane Patricia.....	11
Figure 3. The drag coefficient (aerodynamic drag well)	15
Figure 4. Whitecap coverage experiment by Holthuijsen et al. 2012	17
Figure 5. The air-sea interface under low and moderate winds	18
Figure 6. Schematic of sea spray evaporation showing heat flux	20
Figure 7. The National Hurricane Center’s track and intensity forecasting error.....	22
Figure 8. A schematic of the sea surface microlayer	25
Figure 9. Surfactant production by bacteria in the water column	26
Figure 10. Dispersant application	27
Figure 11. ASIST at University of Miami RSMAS SUSTAIN facility.....	30
Figure 12. Transition criteria from VOF lump to DPM particle in ANSYS Fluent	40
Figure 13. Initial model setup shown in ANSYS Fluent.	41
Figure 14. Data processing of images taken during the laboratory experiment at SUSTAIN..	43
Figure 15. SAR imagery	47
Figure 16. Images taken during the laboratory experiment in clean saltwater	47
Figure 17. Images taken during the laboratory experiment when surfactants were present.	48
Figure 18. air-sea interface under Category 5 wind stress.	49
Figure 19. Mesh adaption in the VOF-to-DPM model	49
Figure 20. Sensitivity experiment of the VOF-to-DPM model	50
Figure 21. Sensitivity experiment 0% surface tension reduction.....	51
Figure 22. Sensitivity experiment 10% surface tension reduction.....	51
Figure 23. Sensitivity experiment 25% surface tension reduction.....	52
Figure 24. Sensitivity experiment 50% surface tension reduction.....	52
Figure 25. Disruptions of the air-water interface under Category 1 hurricane conditions in the laboratory experiment and model	54
Figure 26. Histograms showing the spray size distribution for the laboratory experiment and the VOF-to-DPM	55
Figure 27. Model and Laboratory clean water and surfactant results with CI.....	56
Figure 28. PDF lines from histograms	56

Figure 29. Probability density of spray radius distributions	57
Figure 30. PDF including confidence intervals	58
Figure 31. Comparison of the VOF-DPM model to Veron et al. (2012).....	58
Figure 32. QQ-plot for clean water conditions	59
Figure 33. QQ-plot for surfactant conditions.....	60
Figure 34. VOF-to-DPM spray diameter size distribution with CI (Category 1).....	61
Figure 35. VOF-to-DPM spray diameter size distribution with CI (Category 3).....	61
Figure 36. VOF-to-DPM spray diameter size distribution with CI (Category 5).....	62
Figure 37. VOF-to-DPM spray size distribution from all model runs.....	62
Figure 38. Spray radius distributions for Category 1, 3, and 5 tropical cyclone conditions.....	63
Figure 39. Tropical cyclone Barbara (2019) NOAA VIIRS	66
Figure 40. Tropical cyclone Lane (2018) Aqua MODIS	67
Figure 41. Tropical cyclone Norman (2018) Aqua MODIS	68
Figure 42. Tropical cyclone Olivia (2018) Aqua MODIS	69
Figure 43. Tropical cyclone Sergio (2018) Aqua MODIS.....	70
Figure 44. Tropical cyclone Kenneth (2019) Aqua MODIS	71
Figure 45. Tropical cyclone Kyarr (2019) Aqua MODIS.....	72
Figure 46. Tropical cyclone Marcus (2018) Aqua MODIS	73
Figure 47. Tropical cyclone Dorian (2019) NOAA VIIRS	74
Figure 48. Zoomed tropical cyclone Dorian (2019) NOAA VIIRS	75
Figure 49. Tropical cyclone Florence (2018) NOAA VIIRS.....	76
Figure 50. Tropical cyclone Irma (2017) NOAA VIIRS	77
Figure 51. Tropical cyclone Lorenzo (2019) Aqua MODIS.....	78
Figure 52. Tropical cyclone Michael (2018) Aqua MODIS	79
Figure 53. Tropical cyclone Maria (2017) Aqua MODIS	80
Figure 54. Tropical cyclone Wutip (2019) Aqua MODIS	81
Figure 55. SAR satellite image of the Taylor Energy Platform.....	82

List of Tables

Table 1. Saffir-Simpson Scale for Tropical Cyclones.....	12
Table 2. Raw ANSYS Fluent model spray data.....	44
Table 3. Confidence intervals between model and laboratory data.....	45

List of Equations

Equation 1. Maximum potential intensity	14
Equation 2. Drag coefficient.....	14
Equation 3. Total enthalpy flux	19
Equation 4. Incompressible flow filtered Navier Stokes	32
Equation 5. Incompressible flow filtered Navier Stokes	32
Equation 6. Stress tensor caused by molecular viscosity	32
Equation 7. Subgrid-scale stress for incompressible flows	32
Equation 8. Boussinesq hypothesis subgrid-scale turbulence	33
Equation 9. Rate-of-strain tensor.....	33
Equation 10. Compressible flow filtered Navier Stokes	33
Equation 11. Subgrid stress tensor for compressible flows.....	33
Equation 12. Isotropic and deviatoric parts of stress tensor	33
Equation 13. Smagorinsky model.....	33
Equation 14. Rate-of-strain tensor.....	34
Equation 15. Subgrid-scale turbulent Prandtl number.....	34
Equation 16. Wall-Adapting Local Eddy-Viscosity	34
Equation 17. L_s term of eddy viscosity	34
Equation 18. S_{ij}^d term of eddy viscosity	34
Equation 19. Continuity equation calculated for the volume fraction of each phase in the VOF model.....	35
Equation 20. Explicit solver of the VOF model	35
Equation 21. Momentum equation for the VOF model.....	35
Equation 22. Energy equation for the VOF model.....	36

Equation 23. Mass-averaged energy in the VOF model.....	36
Equation 24. E_q term of mass-averaged energy equation.....	36
Equation 25. Froude number	36
Equation 26. Wave speed	36
Equation 27. Incident wave profile.....	37
Equation 28. Wave number in the x direction.....	37
Equation 29. Wave number in the y direction.....	37
Equation 30. Wave number	37
Equation 31. Effective wave frequency.....	37
Equation 32. Intrinsic wave frequency	37
Equation 33. Droplet trajectories in DPM.....	38
Equation 34. Drag force in DPM.....	38
Equation 35. Reynolds number	38
Equation 36. Smooth particle drag coefficient	38
Equation 37. Spray droplet size distribution	44
Equation 38. Confidence intervals between two datasets.....	45

Abstract

Despite significant improvement in computational and observational capabilities, predicting intensity and intensification of major tropical cyclones remains a challenge. In 2017 Hurricane Maria intensified to a Category 5 storm within 24 hours, devastating Puerto Rico. In 2019 Hurricane Dorian, predicted to remain tropical storm, unexpectedly intensified into a Category 5 storm and destroyed the Bahamas. The official forecast and computer models were unable to predict rapid intensification of these storms. One possible reason for this is that key physics, including microscale processes at the air-sea interface, are poorly understood and parameterized in existing forecast models.

Under tropical cyclones, the air-sea interface becomes a multiphase environment involving bubbles, foam, and spray. The presence of surface-active materials (surfactants) alters these microscale processes in an unknown way that may affect tropical cyclone intensity. The current understanding of the relationship between surfactants, wind speed, and sea spray generation remains limited. Here we show that surfactants significantly affect the generation of sea spray, which provides some of the fuel for tropical cyclones and their intensification.

A computational fluid dynamics (CFD) model was used to simulate spray radii distributions starting from a 100- μm radius as observed in laboratory experiments at the University of Miami Rosenstiel School of Marine and Atmospheric Sciences SUSTAIN facility. Results of the model were verified with laboratory experiments and demonstrate that surfactants increase spray generation by 34% under Category 1 tropical cyclone conditions ($\sim 40 \text{ m s}^{-1}$ wind). In the model, we simulated Category 1 (4 Nm^{-2} wind stress), 3 (10 Nm^{-2} wind stress), and 5 (20 Nm^{-2} wind stress) conditions and found that surfactants increased spray generation by 20-34%.

The global distribution of bio-surfactants on the earth is virtually unknown at this point. Satellite oceanography may be a useful tool to identify the presence of surfactants in the ocean in relation to tropical cyclones. Color satellite imagery of chlorophyll concentration, which is a proxy for surfactants, may assist in identifying surfactant areas that tropical cyclones may pass over. Synthetic aperture radar imagery also may assist in tropical cyclone prediction in areas of oil spills, dispersants, or surfactant slicks.

We anticipate that bio-surfactants affect heat, energy, and momentum exchange through altered size distribution and concentration of sea spray, with consequences for tropical cyclone intensification or decline, particularly in areas of algal blooms and near coral reefs, as well as in areas affected by oil spills and dispersants.

Keywords: sea spray, tropical cyclone, hurricane, air-sea interaction, spume, computational fluid dynamics, CFD, ANSYS Fluent, productivity, surfactants, surface-active materials

Acknowledgements

First, thank you to Dr. Alexander Soloviev, my major advisor and mentor, for his constant support and assistance during my master's at NSU, as well as the opportunities he gave me to complete this research and present it around the globe. Thank you to my committee member, Dr. Richard Dodge, for his continued support of our laboratory and my project. Thank you to my committee member, Dr. William Perrie, for his support, as well as writing and grammatical guidance. Thank you to Dr. Roger Lukas, for the ideas that sparked this research, continuous literature suggestions, and his many stories I have enjoyed receiving from him. I am also grateful to Dr. Brian Haus, Dr. Cayla Dean, Brian Hamilton, and Georgia Parks for their contributions to this work. I also want to thank John Kluge for his assistance in MATLAB. Lastly, thank you to Mikayla Craven, Brian Ettinger, Geoffrey Morrison, and Terry Thompson for their continued support and conversation within the lab. This thesis work was supported by the Gulf of Mexico Research Initiative (GoMRI) Award S120021: "Consortium for Advanced Research on Transport of Hydrocarbon in the Environment (CARTHE)", NOAA Award NA15OAR4310173, and ONR Award N00014-10-1-0938.

I am overwhelmingly grateful to my boyfriend, parents, stepparents, sister, grandparents, and friends for their support and encouragement throughout my education at NSU.

1. Introduction

a. Tropical Cyclones

According to NOAA, tropical cyclone is the term used to describe, “a rotating, organized system of clouds and thunderstorms that originates over tropical or subtropical waters and has closed, low-level circulation.” Tropical cyclones below 39 mph are considered tropical depressions, and those between 39 and 74 mph are tropical storms. Above 74 mph tropical cyclones move to tropical cyclone categorization (i.e. Category 1). The only differentiation between hurricanes, typhoons, and tropical cyclones is the location on earth where they occur. Storms are called hurricanes in the North Atlantic, and central and Eastern North Pacific; while storms in the Northwest Pacific are called typhoons. The term tropical cyclone is used for storms in the South Pacific and the Indian Ocean (NOAA).

While tropical cyclones are not completely understood, there are structures which are characteristic of these storms, which can be seen in Figure 1. Tropical cyclone winds move in a circular pattern, which is considered ‘closed circulation’ (Abtew 2019). This circulation can be clockwise (Southern hemisphere) or counter-clockwise (Northern hemisphere). Outside of the eye is the eyewall, which possesses the strongest winds within the storm. The eye and eyewall make up the core of the tropical cyclone. Surrounding the eyewall are rainbands of thunderstorms that move as a spiral away from the eye of the storm. These rainbands affect tropical cyclone boundary layer thermodynamics through features such as frictional updraft and locally increased surface winds (Kepert 2018). Eye formation, which occurs after banding, in tropical cyclones that have a high potential intensity, and soon after storms become a tropical cyclone (Vigh et al. 2012). Conservation of angular momentum and radial turbulent diffusion of momentum causes eye spin up, and frontal collapse of the eyewall significantly attributes to tropical cyclone evolution (Smith and Montgomery 2016, Emanuel 1997).

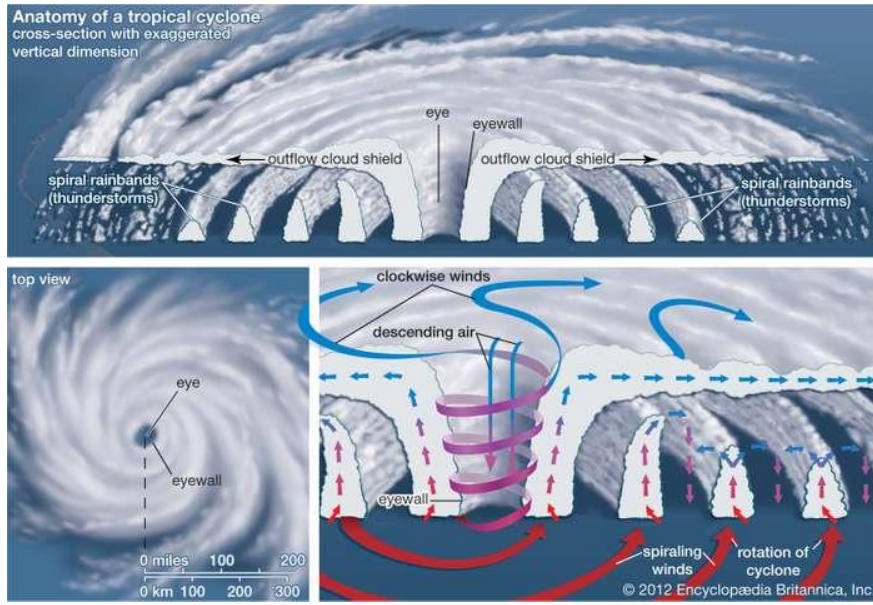


Figure 1. Anatomy of a tropical cyclone (Encyclopedia Britannica).

Tropical cyclones usually have a width of about 300 miles, but this number varies. Size does not necessarily mean the storm is intense. Hurricane Andrew (1992) was relatively small compared to other hurricanes but was one of the most destructive hurricanes to hit the United States (Rappaport & Sheets 1994). The most intense, well-measured, tropical cyclone in history, according to maximum sustained wind speed, was Hurricane Patricia, which hit Mexico and Texas in 2015, with sustained surface winds reaching ~210 mph (Fig 2). Patricia was second in intensity, following Typhoon Tip (1979), which was the most intense tropical cyclone according to its minimum pressure of 870 hPa, and the largest storm, extending for 675 miles (Rogers et al. 2017).

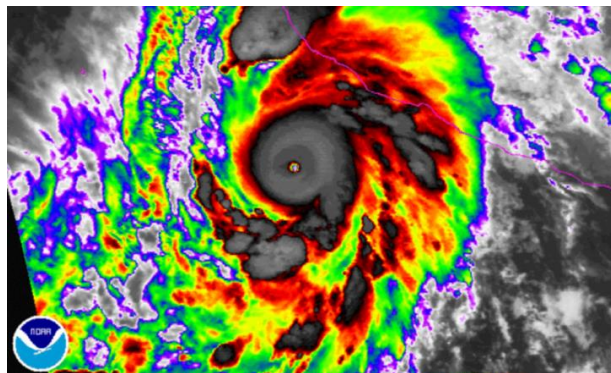


Figure 2. Hurricane Patricia, the strongest tropical cyclone on record with wind speeds topping 215 mph (NOAA).

b. Tropical Cyclone Intensification

Categories of tropical cyclones are classified according to the Saffir–Simpson Scale (Table 1). This scale rates tropical cyclones on a scale of 1 to 5 based on their 10-min average sustained 10m wind speed (Simpson 1974).

Table 1. Saffir-Simpson Scale for Tropical Cyclones.

Category	Sustained Wind Speed	Damage Description
1	74-95 mph	Dangerous winds that will cause some damage. This could cause damage to roofs, shingles, siding, and gutters. May cause damage to tree branches and trunks. Damage to power lines leading to power outages.
2	96-110 mph	Tremendously dangerous winds that will cause widespread damage. This could cause major damage to roofs and siding of homes as well as uproot trees. Power outages are highly probable.
3 (major)	111-129 mph	Will cause overwhelming damage such as damage to frames and remove roofs. Many trees will be damaged and uprooted. Power and water outages for lengthy periods.
4 (major)	130-156 mph	Will cause disastrous damage to homes, such as removing roofs and walls. Most trees and electric poles will be ruined. Complete loss of power and water for periods up to months.
5 (major)	157 mph or higher	Will cause catastrophic damage to areas. Most homes will be destroyed completely. Areas will be isolated by fallen trees and electric poles. Complete loss of power and water for periods up to months.

Rapid intensification is defined by NOAA as “an increase in the maximum sustained winds of a tropical cyclone of at least 34 mph in a 24-h period.” Storms that rapidly intensify often jump from a Category 1 storm (74-95 mph) to a Category 5 storm (>157 mph). Storms above a Category 3 are considered ‘major’ storms (Goldenberg & Shapiro 1996). Tropical cyclones that rapidly intensify have an 80% chance of becoming a major storm and are also the storms with the most inaccurate intensity forecasting (Bhatia et al. 2019).

Tropical cyclones undergo two periods of intensification: a primary slow intensification period and a subsequent rapid intensification period (Sitkowski and Barnes 2009). Tropical cyclones require certain environmental conditions to develop and intensify. These include sea surface temperature >26.5° C, high ocean heat content, high relative humidity, low vertical wind shear, deep convection, and an initial vortex of the right rotation roughly $\pm 5^\circ$ latitude from the equator (Merrill 1988, Tory et al. 2003, Kaplan et al. 2010, Jiang and Ramirez 2013, Fudeyasu et al. 2018). Presence of the salt-stratified barrier layer (Lukas & Lindstrom 1991) is relatively new, but important factor in the problem of tropical cyclone prediction (see, *e.g.*, Grodsky et al.

2012, Kao & Lagerloef 2020). Bio-surfactants have not been previously considered as a factor in tropical cyclone thermodynamics. Heating both within the core and the radius of maximum wind also contribute to intensification of tropical cyclones. Storms that have a large intensity shift in a short period of time (12 hours) or that have a disparity between their current intensity and MPI also have a high chance of intensifying (Fudeyasu et al. 2018).

Internal processes including spiral rainband dynamics, asymmetric deep convection, eye/eyewall mixing, and eyewall replacement cycles of tropical cyclones have also proven important to rapid intensification (Hendricks et al. 2010, Hendricks 2012). Inner-core processes such as convection and precipitation are directly related to the release of latent heat, which fundamentally motivates tropical cyclone development through positive feedback between diabatic heating and moisture convergence from radial circulation (Jiang and Ramirez 2013). There remains a debate on whether symmetric or asymmetric convection and circulation is more important to storm intensification (Ooyama 1969, Smith 1969, Smith 1981, Shapiro and Willoughby 1982, Montgomery and Smith 2011). Jiang and Ramirez (2013) found that rapidly intensifying tropical cyclones do not always have more inner-core convection than storms which do not rapidly intensify. Their results did find that rapidly intensifying storms required a minimum threshold of the precipitation area, volume of precipitation, and convective intensity in the inner-core, meaning the storm must be organized in order to intensify and/or rapidly intensify.

Researchers estimate the limits on tropical cyclone intensity through the approximation of Maximum Potential Intensity (MPI). Miller (1958) first estimated MPI using maximum air temperature in the eyewall caused by sinking air. Malkus and Riehl (1960) calculated parcel trajectories of available energy to counteract momentum loss. Emanuel (1986, 1995) estimated MPI using the storms energy cycle to approximate the maximum surface wind speed. More recently, Shay & Brewster (2010) and Lin et al. (2013) included ocean heat content to MPI estimations. Calculations of MPI combine dynamics and thermodynamics (Holland 1997). These include momentum, or the amount of motion measured as a product of mass and velocity, hydrostatic balance, where the horizontal pressure gradient is at equilibrium with the Coriolis and centripetal accelerations (Marks 2004), temperature, or heat intensity, and pressure, or the physical force exerted on an object. Enthalpy, the total heat content of a system, is also crucial to tropical cyclones and air-sea interaction processes. Latent (heat required to convert a liquid to

vapor) and sensible (heat that changes temperature) heat fluxes contribute to enthalpy, along with pressure and volume.

MPI helps to estimate the upper limit of tropical cyclone intensity as follows:

$$V^2 = (k^* - k) \frac{(\bar{T} - T_0) C_k}{T_0 C_d} \quad (1)$$

where V is wind speed, C_k the enthalpy coefficient, C_d the drag coefficient, k^* the saturation enthalpy at the sea surface, k the enthalpy, \bar{T} the pre-cyclone depth-averaged temperature, and T_0 the outflow temperature at the top of the tropical cyclone. MPI is proportional to the ratio C_k/C_d , thus controlling the maximum tropical cyclone intensity for given other variables. Air-sea exchanges play an important role in tropical cyclone intensity because it depends on momentum and enthalpy transfers at the air-sea interface (Emanuel, 1986; Ooyama, 1969).

C_k may not strongly depend on wind speed for winds $U_{10} > 10 \text{ m s}^{-1}$ at 10 m height (Jeong et al. 2012). The laboratory result from Jeong et al. (2012) was limited to the maximum equivalent neutral stratification wind speed of $U_{10} = 40 \text{ m s}^{-1}$, which was in part corroborated by aircraft-based flux measurements (Drennan et al. 2007) and extended by Richter and Stern (2014) and Bell et al. (2012) to $U_{10} = 70 - 75 \text{ m s}^{-1}$ using dropsonde data or by utilizing the conservation of azimuthally averaged absolute angular momentum, respectively. The laboratory experiment by Komori et al. (2018) conducted in the high-speed wind-wave tank at Kyoto University reported substantial increase in C_k above a 35 m s^{-1} wind speed, which could be due to intense spray generation.

The drag coefficient (C_d) is a determining factor in tropical cyclone intensity and is crucial to the estimation of MPI. It can be calculated by:

$$C_{10} = \frac{\tau}{\rho_a U_{10}^2} \quad (2)$$

where U_{10} is the wind speed at 10 m height, τ is the wind stress, and ρ_a is the air density (Stewart 2002). Recent studies show that C_d , which increases with wind speed until $\sim 30 \text{ m s}^{-1}$, is a determining factor in tropical cyclone intensity (Bell et al., 2012, Jarosz et al., 2007, Kossin et al. 2013, Donelan et al., 2018). Between 30 and 60 m s^{-1} C_d decreases, which is favorable for

tropical storm intensification, because the KH instability at the air-sea interface leads to an absence of short surface waves (the instability grows more quickly due to large shear for short waves), and the two-phase near surface layer thickens. Around 60 m s^{-1} , where C_d stops decreasing, is considered the aerodynamic drag well (Soloviev et al. 2017). The aerodynamic drag well (Fig. 3) also demonstrates why many storms do not progress to Category 5, because the slope (against wind speed) of C_d is positive above 60 m s^{-1} , which does not provide favorable conditions for further intensification since the sea surface momentum loss increases dramatically. Instead of intensifying, the aerodynamic drag well likely (depending on MPI) leads to a storm remaining at Category 3 intensity (at the bottom of the drag well), which explains bi-modal distribution of maximum intensity found by Kossin et al. (2013), as shown in Figure 3.

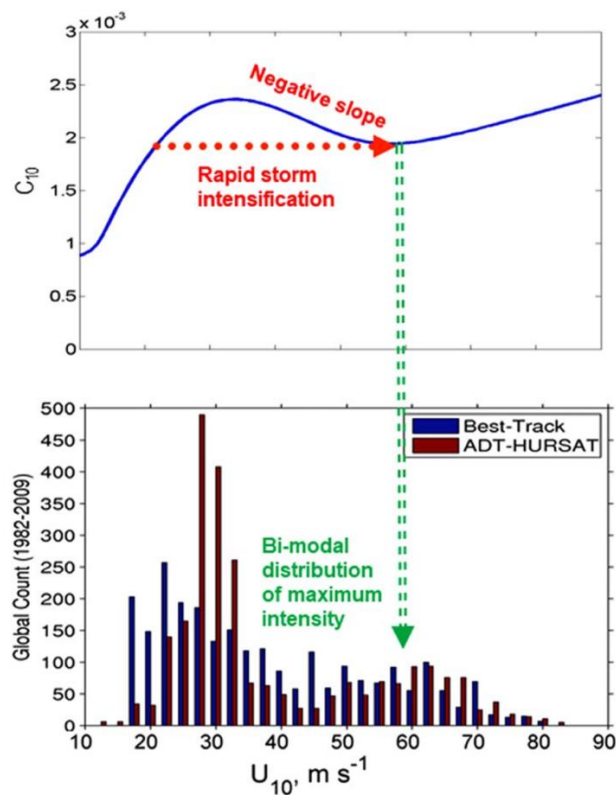


Figure 3. (top) The drag coefficient displaying the aerodynamic drag well at $\sim 60 \text{ m s}^{-1}$. (bottom) Bimodal distribution of lifetime maximum intensity for tropical cyclones (Kossin et al. 2013). (figure from Soloviev et al. 2017).

Above 60 m s^{-1} , the increase of C_d could be caused by the entrainment of large amounts of sea spray (Andreas & Emanuel 2001), which was implemented into the concept of rapid intensification and the aerodynamic drag well (Soloviev et al. 2017). It is uncertain how C_d behaves above 120 m s^{-1} wind speeds. Soloviev et al. 2014 found that it increased, while Takagaki et al. 2012 found that it approached a constant value. If sea spray is a significant factor in the increase of C_d above 60 m s^{-1} , the continued increase of spray generation as winds increase above 120 m s^{-1} may also lead to further increase of C_d . Takagaki et al. 2012 acknowledged that there are differences between field and laboratory measurements of spray (which may or may not influence drag at high wind speeds) and a better understanding of spray is necessary. Further understanding, based on measurements and observations, of enthalpy and momentum flux physics will aid in improved tropical cyclone intensity forecasting.

c. Multiscale Physics at the Air-sea Interface Under Tropical Cyclone Conditions

Within tropical cyclones, the atmosphere and ocean are strongly coupled. The air-sea interface controls and is controlled by momentum, heat, mass, and energy exchanges between the ocean and atmosphere. Tropical cyclones gain heat and moisture from, as well as transfer momentum and kinetic energy to the ocean, through the air-sea interface. In the high wind conditions of tropical cyclones, a two-phase environment is created near the sea surface. In this environment, spray droplets are generated by white caps on breaking waves and in waves that have not broken, in a process that resembles the Kelvin-Helmholtz (KH) instability (Koga 1981, Soloviev & Lukas 2010, Soloviev et al. 2017). Most spray is formed at wave crests, either with or without a whitecap, but spray drops are also formed elsewhere in this environment. The two-phase environment produces a white sheet, or ‘white out’, which consists of air-bubbles in the water, spray droplets in the air, and foam on the sea surface (Soloviev et al. 2017). Spray and bubbles increase the effective surface area at the air-sea interface, which affects heat and momentum fluxes. According to Holthuijsen et al. 2012, in tropical cyclones wave-breaking whitecaps, which are a mixture of bubbles and spray, only cover ~4%, while the ‘white out’ associated with foam and spray streaks covers ~96% of the sea surface. Whitecapping with spray and bubble formation occurs once wind speeds exceed $7\text{-}9 \text{ m s}^{-1}$, but the formation of a continuous two-phase environment is only observed when wind speeds are above $\sim 30 \text{ m s}^{-1}$. The replacement of whitecaps with ‘white out’ on the sea surface alters momentum exchange

between the ocean and atmosphere. The development of the two-phase environment also produces additional drag near the sea surface.

It previously was thought that C_d monotonically increases with wind speed, but since has been found to peak at wind speeds of $\sim 35 \text{ m s}^{-1}$ and actually decline until $\sim 60 \text{ m s}^{-1}$ (Soloviev et al. 2014, 2017). This behavior of the drag coefficient corresponds to the change from whitecap to ‘white out’ conditions under high wind speeds, as shown in Figure 4 (Holthuijsen et al. 2012).

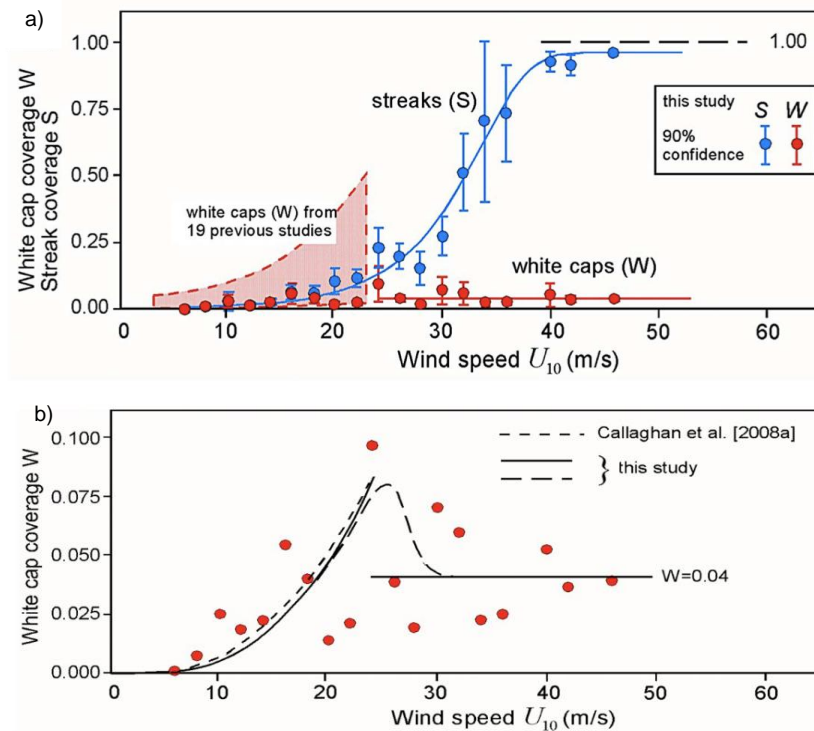


Figure 4. Experiment by Holthuijsen et al. 2012. (a) Whitecap coverage observed to increase to a maximum at about $U_{10}=24 \text{ m s}^{-1}$, then decrease and remain limited. Meanwhile, streaks (‘white out’) are shown to increase to almost 100% coverage. (b) Another schematic showing the whitecap coverage increasing to a maximum at $U_{10}=24 \text{ m s}^{-1}$. The whitecapping then decreases to a limited value.

d. Sea Spray and Spume Generation

Under light winds, the KH instability of the air-water interface contributes to surface wave generation in the gravity-capillary range (Fig. 5a) (Miles 1959). Under wind speeds above $4\text{-}5 \text{ m s}^{-1}$ short wavelets steepen and break internally, causing ‘microscale wave breaking’, which does not disrupt the air-sea interface enough to eject spray (Siddiqui, & Loewen 2007, Banner

& Phillips 1974, Jessup et al. 1997, Siddiqui et al. 2001). Under tropical cyclone force winds, the gravity and surface tension forces are overcome by pressure fluctuations due to KH instability in the air flow, which disrupt the air-sea interface leading to sheets, fingers, and intense sea spray generation (Fig. 5b) (Soloviev & Lukas 2010, Hoepffner et al. 2011).

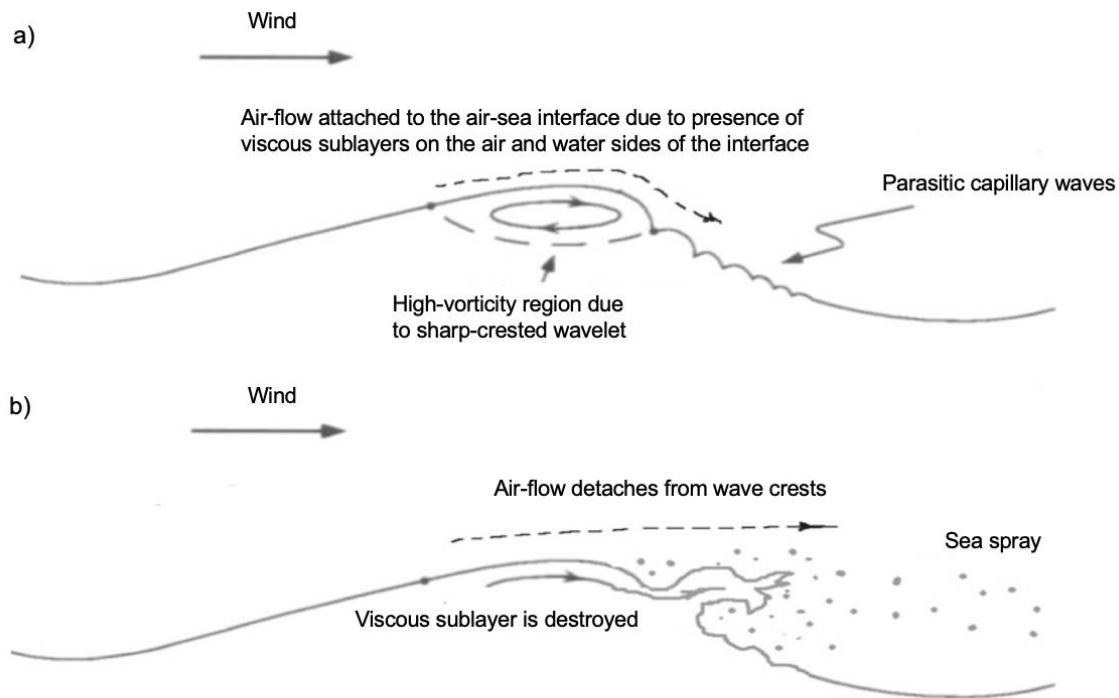


Figure 5. (a) Under moderate winds – wave surface with capillary waves. (b) Under high winds – waves break, which disrupts the air-sea interface and produces spray (Soloviev & Lukas 2010).

In laboratory experiments, radii of sea spray have been observed in the range of less than 1 μm to up to 6 mm (Andreas 1992, Veron et al. 2012). Small sea spray particles, which are typically sub-micrometer to tens of micrometers in diameter, are mostly generated by bursting air-bubbles (Spiel 1997, 1998), which produce film and jet spray droplets. Film droplets typically range from 0.5 to 5 μm . Jet spray droplets are produced by the water jet breakup formed by the bubble (Blanchard 1963, Wu 1981) and range from 3 to 20 μm in diameter (Gall et al. 2008). Another mechanism of spray generation is ‘bag-breakup’ fragmentation (Troitskaya et al. 2017) in which bag like pieces of water inflate and then quickly burst into spray droplets.

Larger spray droplets, above 20 μm (spume), are produced by breaking waves (Gall et al. 2008). Under moderate winds ($\sim 7\text{-}11 \text{ m s}^{-1}$), ‘tearing of water’ from wave crests (Monahan et al. 1983) form spume droplets. When waves curl over and break, another type of spume droplet is formed -- splash droplets (Kepert et al. 1999). Koga (1981) and Veron et al. (2012) found that near the wave crest, where the wind stress is usually the highest, small convoluted projections of the water surface develop and break up to form spume droplets. The projections resume the KH instability at an interface with a very large density difference, which is characterized by strong asymmetry (Hoepffner et al. 2011). The majority of the disturbance to the air-sea interface occurs on the air side; in fact, the KH instability generates spray and spume in the air but very few bubbles are produced in the water. At the same time, air-bubbles are mainly associated with whitecaps produced by longer breaking waves interacting with shorter, steeper gravity waves driven by local wind fluctuations (Thorpe 1986).

Spray droplets are either entrained in the turbulent air flow or return to the sea surface (Andreas 1992, Soloviev et al. 2014). Small spray droplets are typically suspended in the turbulent air flow, and eventually evaporate. Spray must first cool from the sea surface temperature to its evaporation temperature, which usually occurs in less than one second because cooling only requires evaporation of less than 1% of the droplet’s mass (Kepert 1996, Andreas & Emanuel 2001). The temperature each droplet reaches depends on size, salinity, temperature, humidity, and residence time in the air (Andreas & Emanuel 2001). The droplet must then evaporate, which takes over two orders of magnitude longer to accomplish (Kepert 1996). Evaporation of spray, while it does not influence the ocean, does influence the atmosphere by changing air temperature and adding vapor to the air (Andreas & Emanuel 2001). Understanding how spray affects the enthalpy flux between the ocean and atmosphere is critical because surface enthalpy flux provides most of the energy to tropical cyclones. The total enthalpy flux is calculated as:

$$H_{s,tot} + H_{l,tot} = H_l + H_s + Q_s + Q_l \quad (3)$$

where $H_{s,tot}$ is the total sensible heat flux, $H_{l,tot}$ is the total latent heat flux, H_l is the surface latent heat flux, H_s is the bulk surface sensible heat flux, Q_s is the droplet sensible heat flux, and Q_l is the spray-air latent heat flux (Gall et al. 2008).

Evaporating spray uses sensible heat from the boundary layer air (Fig. 6). This lost heat is balanced by latent heat, which is added back to the boundary layer air through water vapor from the evaporated particles (Gall et al. 2008). Therefore, these small droplets may not contribute much to the enthalpy flux into a tropical cyclone due to the spray negative feedback phenomenon, which limits the total spray influence on total heat flux from water to air (Peng & Richter 2019). Spume droplets, which are ‘re-entrant’ spray, return to the sea surface before they are able to take enough sensible heat from the atmosphere to evaporate. Therefore, spume makes up a large part of the net spray-mediated enthalpy flux and significantly contribute to the enthalpy flux to the atmosphere under tropical cyclone winds (Andreas 1992, Kepert et al. 1999). Since tropical cyclones respond to net enthalpy fluxes, rather than the individual sensible and latent heat fluxes, it is likely that ‘re-entrant’ spray contributes to changes in tropical cyclone intensity (Andreas & Emanuel 2001).

Spray also influences drag at the air-sea interface. Momentum is taken from the atmosphere when spray is entrained in the airflow. ‘Re-entrant’ spray then gives this momentum to the ocean when it returns to the sea surface. The influence of this drag has been debated. Wu (1973) found that is insignificant, while Fairall et al. (1994) found it is only important above winds of 50 m s^{-1} . Pielke & Lee (1994) found that the drag induced by spray reduces wind speed by 15% and therefore increases surface stress.

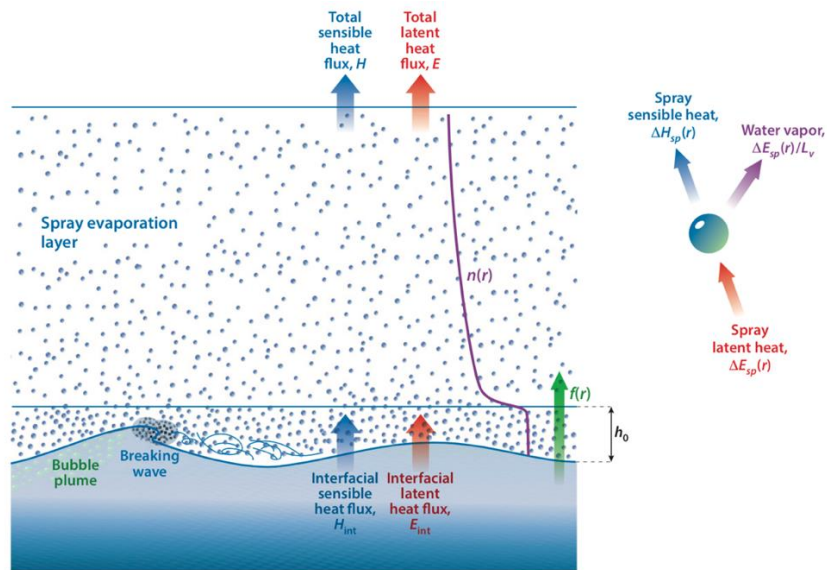


Figure 6. Schematic of sea spray evaporation showing latent and sensible heat fluxes between the ocean and atmosphere through spray evaporation (Veron et al. 2015).

Under tropical cyclone conditions, the modification of sensible and latent heat fluxes and momentum fluxes due to large amounts of spray leads to changes in tropical cyclone structure and intensity (Fairall et al. 1994, 2014, Edson & Fairall 1994, Andreas & Emanuel 2001, Gall et al. 2008, Andreas et al. 2017). Kepert et al. (1999) and Peng & Richter (2019) noted the following fundamental issues that relate to spray effects: the sea spray generation function, the feedback by which spray droplets modify the environmental conditions, and parameterization of the thermodynamic effects of sea spray for tropical cyclone models. These problems remain due to the complexity of the air-sea interaction process during tropical cyclones and difficulties in direct observations during extreme conditions. Only a few experimental or observational studies attempted to measure the heat fluxes in tropical cyclone conditions (*e.g.*, Drennan et al. 2007, Zhang et al. 2008). Tropical cyclone analysis is generally based on indirect measurements (Bell et al. 2012, Richter & Stern 2014) or laboratory experiments (Jeong et al. 2012, Komori et al. 2018).

e. Tropical Cyclone Prediction

Predicting intensities of tropical cyclones, especially their rapid intensification, remains a daunting challenge despite advances in model forecasting through increased computer power and improved observational data systems. While cyclone track prediction over all time scales has improved by over 60% in the past 30 years (Fig. 7a), there has been less improvement in the accuracy of forecasting the intensification of tropical cyclones since the 1990's (Rappaport et al. 2009, DeMaria et al. 2014, Emanuel & Zhang 2016, Masters 2020). Forecasting intensity improvement has plateaued since 2013 for 24-48 hours and has actually increased since 2018 for 96 and 120 hours, as shown in Figure 7b. The increase since 2018 is likely due to the poor prediction of Hurricane Dorian's rapid intensification (Masters 2020). Intensity error from the best available model decreased by only 1-2% per year between 1989 and 2012 (DeMaria et al. 2014). Tropical cyclones Charley 2004, Wilma 2005, Humberto 2007, Maria, 2017, and Dorian, 2019 all intensified prior to landfall, devastating unprepared communities due to rapid intensification that was missed by tropical cyclone forecast models. Effective tropical cyclone forecasting is highly complex and must account for many processes in both the atmosphere and ocean (Gopalakrishnan et al 2012). Recent model improvements include focusing on the inner-

core structural changes of the storm (Chen et al 2011), implementing cloud-resolving models (Yau et al 2004), and increasing model resolution to below 1 km (Davis et al 2011). In addition to improvements to the atmospheric component, concepts of ocean heat content (Shay et al. 2000, Lin et al. 2008), barrier layer (Lukas & Lindstrom 1991), and air-sea interface (Soloviev et al. 2017) have recently been introduced into the consideration of tropical cyclone physics.

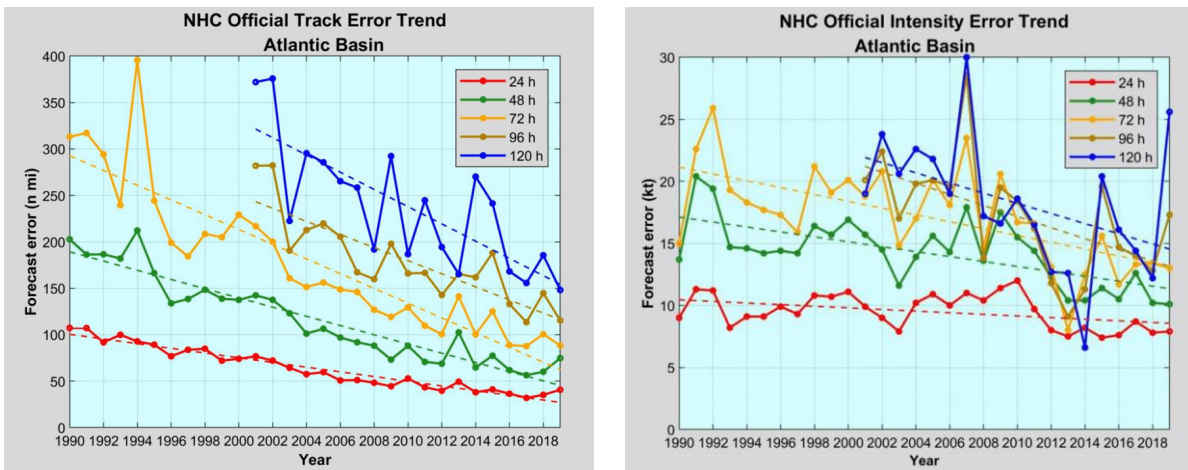


Figure 7. The National Hurricane Center’s error in (a) track forecasting and (b) intensity forecasting (Masters 2020).

Intensity forecasting remains a challenge in part due to an incomplete understanding of key physics that contribute to intensification of tropical cyclones. This includes cloud microphysics. It has been predicted that aerosols serving as cloud condensation nuclei intensify the tropical cyclone if they penetrate the central clouds of the storm but weaken it if they penetrate the clouds at the storm periphery (Shpund et al. 2019).

Microscale processes at the air-sea interface are among the processes that still need to be more adequately parameterized in existing models. Sea spray is one of the key microscale processes that struggles to be parameterized due to its complex physics and lack of measurements under strong winds. Riehl (1954) was the first to report that spray evaporation under high winds offers part of the heat required for intensification of tropical cyclones. Fairall et al. (1994) was the first to implement spray-based parameterization to a model of the tropical cyclone boundary layer and found that evaporation may be important to maintaining this boundary layer. The spray parameterization used by Fairall et al. (1994) was that spray sensible heat flux contributed 6% of the direct sensible heat flux, while the spray latent heat flux

contributed 60% of the direct latent heat flux. The negative sensible heat flux caused by spray taking energy to evaporate from the boundary layer was found to be much larger than the spray sensible heat flux. Using a continuation of Fairall's work, Kepert et al. (1999) found that spray evaporation influenced the tropical cyclone boundary layer stratification and therefore could affect intensity of the storm. Lighthill et al. (1994) found the opposite, that spray reduced intensity of tropical cyclones because of evaporative cooling. Wang et al. (1999) and Uang et al. (1999) found that spray had little to no effect tropical cyclone intensity, but they did not account for 're-entrant' spray in their models. Bao et al. (2000), using the parameterization of Fairall et al. (1994), found that if spray evaporates, it has little to no influence on tropical cyclone intensity, but if spray re-enters the ocean, intensity is affected. Andreas & Emanuel (2001) also found that spray is important to enthalpy and momentum fluxes between the ocean and atmosphere under high winds, and that 're-entrant' spray contributes most to the enthalpy flux. They also concluded that including wave drag and spray enthalpy and momentum exchange resulted in a cancellation of one another, explaining why models that are too simple to account for complex microphysics at the air-sea interface do not accurately predict intensity.

Perrie et al. (2005) included spray in the Canadian mesoscale model and found that it increased storm intensity, as well as cooled near the sea surface and warmed upper parts of the boundary layer. In contrast to this, Barnes (2006) and Gall et al. (2008) found that spray may actually warm near the sea surface of the boundary layer. Gall et al. (2008) also found that spray sensible and latent heat fluxes are enhanced as spray generation increases, which increased intensity of the storm, but spray drag slightly weakened the storm. Shpund et al. (2012) deemed the lowest 400 m of the atmosphere, which directly interacts with spray, the hurricane atmospheric mixed layer. The microphysical structure of this layer is directly impacted by the upward transport of spray by large eddies. The results from Shpund et al. (2012) also found that spray's effect depends on the initial humidity and temperature: if the humidity is low, spray evaporation cools the hurricane atmospheric mixed layer, while if the humidity is high, spray evaporation has less impact.

An effort to include bulk parameterization of the air-sea momentum flux, which was found to be of key importance to sea surface wind speeds, enhanced the parameterization of the wind-pressure relationship of major tropical cyclones in predictions models (Moon et al 2007). Bao et al. (2017) found, by implementing air-sea sensible and latent heat fluxes into their model,

that spray decreases the drag coefficient, and therefore accelerates the flow near the sea surface in the boundary layer. This in turn led to increased tropical cyclone intensity in stronger storms, but variable intensity in weaker storms. Lee et al. (2019) more carefully considered the wind-dependent drag coefficient in their model, which led to an improvement in prediction of rapid intensification within 24 hours by 16%.

Despite advances, uncertainty remains due to various challenges in modeling microscale processes involved in tropical cyclone dynamics. One major issue is a lack of observations and measurements under tropical cyclone conditions (Fairall et al. 2014). Most parameterizations of air-sea fluxes have focused on winds below 25 m s^{-1} because observations of spray above 20 m s^{-1} are lacking (Gall et al. 2008, Zhang et al. 2008, Fairall et al. 2014). This makes extrapolating these parameterizations to high wind conditions difficult. One key factor that exists at winds $>25 \text{ m s}^{-1}$ is the abundance of sea spray. Zhang et al. (2008) and Fairall et al. 2014 suggested that at high wind speeds, spray becomes abundant, which complicates enthalpy transport and may change heat and momentum coefficients. Accurate parameterization of the thermodynamic influence of spray is still a challenge (Fairall et al. 1990, 1994, Kepert et al. 1999, Bianco et al. 2011, Richter & Sullivan 2014). Fairall et al. (2014) explained that the sea spray effect is parameterized using the size dependent source function (the number of droplets of a certain size produced at the sea surface, per unit surface area, per unit time, as a function of surface forcing). The issue with this is that the source function cannot be measured directly and is therefore estimated. Spray sizes used in models also requires better parameterization. Implementing the entire range of spray sizes in models also remains a challenge. Many studies have focused on spray diameters between 0.5 and 10 mm (Shpund et al. 2012), but spray droplets often have radii below 0.5 mm, and even as small as $1 \mu\text{m}$ (Andreas 1992, Veron et al. 2012). Measurements in the ocean also have lacked those on large spray droplets ($r > 20 \mu\text{m}$), which are likely the most important to air-sea enthalpy and momentum fluxes. Gall et al. (2008) argued that a better understanding of the spray generation function is needed to fully understand how much spray is generated in the boundary layer. Shpund et al. (2012) recognized that their work still needed to account for wind speed changes, as this increases spray generation and also the amount of spray transported to upper layers of the atmosphere.

Another limitation of previous models is that they are often one dimensional, because most microscale processes occur in only tens of meters above the air-sea interface (Shpund et al.

2012). One-dimensional models may oversimplify the complexity of air-sea interaction processes. Bao et al. (2017) specified that including wave-induced drag effects on spray drag could be important to modeling efforts. Overlooking key physics in models often leads to inaccurate hurricane intensity predictions, further leading to erroneous warnings and evacuations that may cost lives. Therefore, it is essential to implement more accurate fluxes at the air-sea interface and their effect on tropical cyclone intensity into future prediction models to increase forecasting accuracy.

f. Surfactants

One factor that affects the air-sea interface are surface-active materials (surfactants). Surfactants are hydrophobic, meaning they repel water, and therefore accumulate in the sea surface microlayer (SML) if they are less dense than seawater. The SML consists of the top 1000 μm of the ocean and is defined by many molecular sublayers that have large gradients between or within them (Fig. 8). This microlayer is greatly affected by physical, chemical, and biological properties (Wurl et al. 2011, Kurata et al. 2016).

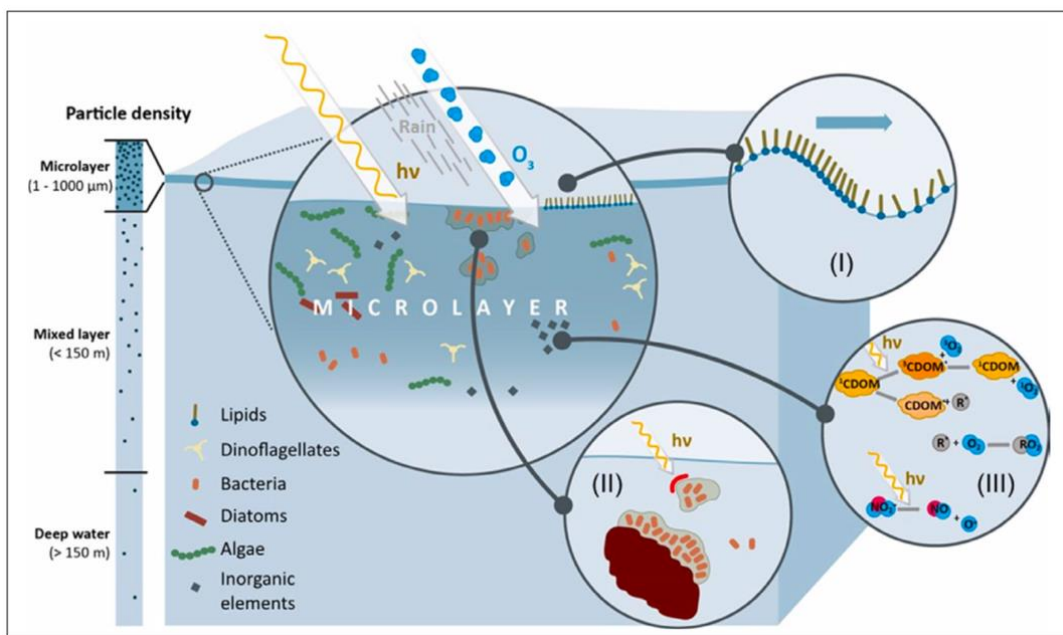


Figure 8. A schematic of the SML by Wurl et al. 2017.

Surfactants are often produced by marine organisms such as phytoplankton, zooplankton, zooxanthellae, and bacteria (Fig. 9). These compounds consist of substances such as lipids,

proteins, saccharides, and organic acids (Alpers and Espedal 2004). Carbohydrates, polysaccharides, and complex β -glucans are common surfactants found during phytoplankton blooms (Wurl et al 2011).

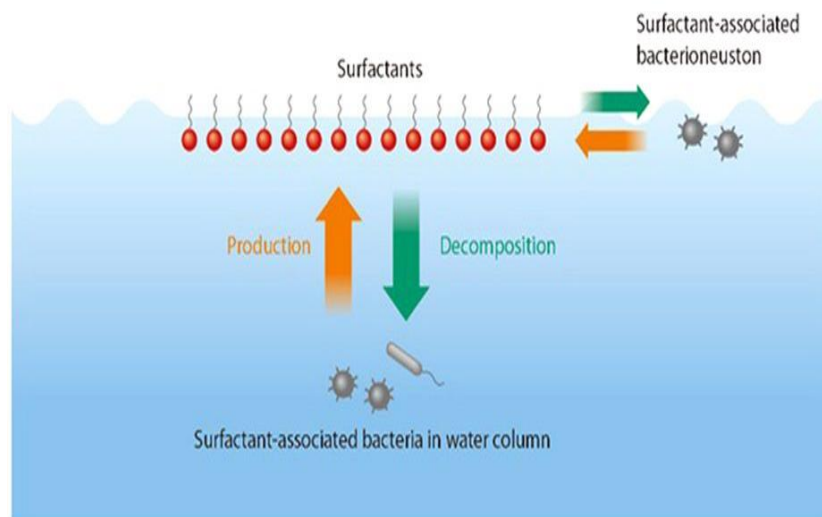


Figure 9. Surfactant production by bacteria in the water column and accumulation on the sea surface, which dampens waves (Kurata et al. 2016).

Phytoplankton are one of the major producers of biological surfactants (Wurl et al 2011). Phytoplankton are primary producers, meaning their production of surfactants depends on light energy. Therefore, when primary production is high, or during blooms, the presence of surfactants is also likely to be high (Alpers and Espedal 2004). Using primary productivity as an indication of the presence of the SML, and therefore likely surfactants, has been used in previous experiments, such as Wurl et al. (2011). During this experiment they found that the SML and primary production were positively correlated.

Coral reefs, which are highly productive environments, also produce surfactants. Deacon (1979) explored the results of a previous study on the effect of coral mucus on wind drag over a coral reef. Coral mucus contains lipids that have a high concentration of cetyl palmitate (up to 80%). When cetyl palmitate is hydrolyzed, cetyl alcohol and palmitic acid are produced. Both of these substances have a polar-nonpolar molecular structure that is common in surfactant compounds. The abundance of surfactants from coral reefs therefore may be dependent on the hydrolysis of cetyl palmitate. The pH of seawater (~8) aids in hydrolysis, but wind speeds may

also have an effect on hydrolysis and the residence time of surfactants in surface waters (Deacon 1979). Slicks, likely formed from coral mucous surfactants, have been observed using Synthetic Aperture Radar (SAR). Specifically, slicks have been observed during coral spawning in Western Australia, further indicating that coral mucous may form surfactant slicks on the sea surface (Jones et al. 2006).

Surfactants may also appear on the sea surface during oil spills and through the use of dispersants (Fig. 10).

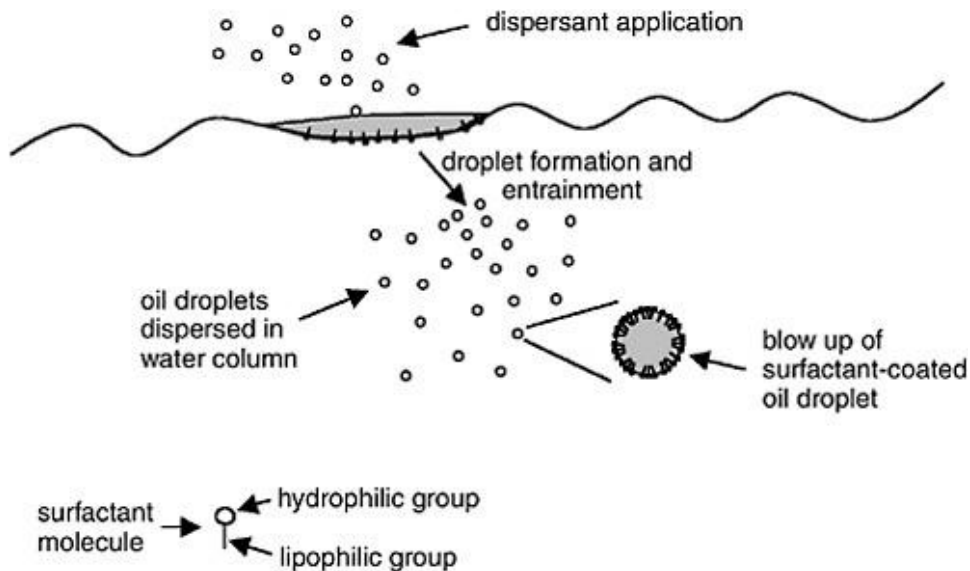


Figure 10. A schematic showing how dispersant application disperses oil spills using surfactants (National Research Council 2005).

Surfactants also modify the air-sea interface and the near-surface layer of the ocean, as they alter surface tension. Due to their effect on surface tension, surfactants dampen short gravity-capillary waves and air-sea gas exchange, suppress near-surface turbulence, and produce coherent structures (Wurl et al. 2011). Soloviev et al. (2011) found that C_d from the water side of the air-sea interface was reduced by 36% due to the effect of surfactants, meaning that momentum and other fluxes that depends on C_d between the air and water are reduced by surfactants. Surfactants often produce slicks, or films, on the sea surface under low wind speed conditions (Kurata et al. 2016). Slicks are frequently formed from one molecular layer (~3 nanometer thickness), which allows for a small quantity of surfactant material to form a slick that

covers a large area of the sea surface (Alpers and Espedal 2004). These slicks may have a significant effect on the air-sea gas exchange rates of many gases, including greenhouse gases such as carbon dioxide, methane, and nitrous oxide (Wurl et al. 2011).

The coverage, concentration, and composition of sea surface slicks caused by surfactants vary depending on wind, sea conditions, and with time. Under wind speeds above 7 to 10 m s⁻¹, breaking waves disrupt slick formation and overwhelm the effect of surfactants (Soloviev & Lukas 2014). The effect of surfactants once again becomes important under tropical cyclone conditions due to their effects on sea spray. Notably, the size distribution of sea spray is expected to depend on the presence of surfactants. During high wind speed conditions surfactants are brought to the surface by turbulence and air-bubbles with increased mixing in the water column, enhanced by upwelling under the tropical cyclone (Price 1981, Alpers & Espedal 2004, Walker et al. 2005). Once brought to the surface, bubbles that burst release some surfactant material into the air as aerosols, and the remaining may form slicks on the sea surface. Foams are often produced by bubble bursting and the reforming of slicks afterwards, which can occur within seconds (Wurl et al. 2011).

2. Hypotheses

- Surfactants influence the size distribution and abundance of sea spray under tropical cyclone conditions.
- Satellite imagery overlaid with major tropical cyclone tracks will reveal association between primary productivity (a proxy for bio-surfactants) and tropical cyclone intensity.
- In the ocean under tropical cyclone conditions, the surfactants extracted from deeper in the water column may affect heat, energy, and momentum exchange through an altered size distribution of sea spray, with possible consequences for tropical cyclone intensification or decline.

3. Statement of Objectives

- Use ANSYS Fluent Computational Fluid Dynamics (CFD) Volume of Fluid to Discrete Phase Model (VOF-to-DPM) to study the effect of surfactants on sea spray size distribution and abundance to understand if they influence the generation of spray under tropical cyclones.
- Because model results must be compared with real measurements (laboratory or field), I will confirm the VOF-to-DPM model with laboratory results on sea spray size distributions under tropical cyclone force winds from experiments at the University of Miami laboratory facility.
- Analyze MODIS, VIIRS, and SAR satellite imagery for abundance of surfactants in the path of tropical cyclones to further explore the potential association between surfactants and tropical cyclone intensity.

4. Methods

a. Laboratory Experiment

A laboratory experiment was conducted at the University of Miami Rosenstiel School of Marine and Atmospheric Science (RSMAS), using the Air-Sea Interaction Saltwater Tank (ASIST) in the SURge STRUCTure Atmosphere INTERaction (SUSTAIN) facility (Fig. 11). The tank is 15 m long, 1 m wide, and 1 m in height, and has an acrylic glass exterior, which is transparent and allows for equipment to be placed outside the tank, rather than within. The water level was set to 0.42 m for this experiment.



Figure 11. ASIST at University of Miami RSMAS SUSTAIN facility (Soloviev et al. 2011).

The ASIST tank contains various equipment to simulate ocean conditions. The wave generator produces waves with frequencies between 0.25 Hz and 3 Hz, and amplitudes between 0 and 0.1 m. The wind generator is able to produce winds up to 40 m s^{-1} (scaled to a 10 m height), while the current generator can produce current speeds up to 0.5 m s^{-1} . For our experiment, we set the wind speed (extrapolated to a 10 m height) to 40 m s^{-1} . Mechanical wave and currents were not used during the experiment. Temperature is also controlled and can be kept anywhere between 5 and 40° C . For our experiments, the measured water temperature was 23.2° C and 24.3° C . The air in the tank is circulated with either an open or closed loop. Fresh air from the troposphere is captured and expelled after passing through the tank. In the closed loop option, which was used for this experiment, the air is maintained in the tank. This option was chosen because open loop is typically used to avoid quick saturation when measuring gas transfer. Measured air temperatures were 24.5° C and 24.6° C for our experiments. Saltwater was filtered from Bear Cut inlet near the facility, resulting in a salinity of $\sim 33 \text{ psu}$ during the experiments. Temperature measurements were only taken at the beginning of the experiment.

A Digital Laser Elevation Gauge (DLEG), consisting of a line-scan camera and laser beam that crossed the tank at the water surface, was set up on the outside of the tank. Additionally, two Argon-ION air-cooled lasers were used, which contained beam splitters and mirrors. This allowed for six vertical beams to be focused on any point in the tank, which is crucial as these beams and line-scan cameras detect the water surface. In order to make the beams easier to see, Fluorescein dye was added to the water in the tank. The line-scan cameras

had 1024-pixel resolution and a 250 Hz sampling rate. Using this equipment allowed for an accurate surface elevation measurement, to a 0.2 mm resolution. A *Hisense* camera was also synchronized with the lasers to record images. To capture spray droplets, a collimated light beam was used. This beam was focused through a diffusing screen to reduce its intensity. The *Dantec* camera was then placed opposite from this diffused beam. Images of spray droplets were focused on a single plane, located at the center of the ASIST tank (Ortiz-Suslow 2016, Mehta et al. 2019). During the experiment, pairs of images were taken 500 mm apart. In total, three sets of 250 images were taken when surfactants were introduced, and one set of 250 images were taken with clean water in the tank. One set of each experiment was analyzed for this work.

Surfactant trials were conducted after clean water experiments, and the water in the tank was switched between each trial. In order to introduce surfactants, Oleic acid (31.92 mN/m surface tension) or oleyl alcohol (31.7 mN/m surface tension) were used. Both were diluted in 95% ethanol; oleic acid with an 8 mmol/liter ethanol concentration, and oleyl alcohol with a 3 mmol/liter ethanol concentration. During each trial, 60 ml of the solution was added to the tank using a syringe from the upwind side of the tank. The surfactant plume passed by the measurement area with the surface current created by the applied wind stress (Soloviev et al. 2011).

b. ANSYS Fluent CFD Model Theory

ANSYS Fluent CFD software provides a large assortment of physical model capabilities, which include flow, turbulence, multiphase, and heat transfer. To model sea spray generation under tropical cyclone conditions, we use a combination of Fluent's Large Eddy Simulation for turbulence (LES), the Volume of Fluid (VOF) for multiphase flow, and the Discrete Phase Model (DPM) for particle/droplet tracking. Recently, Fluent implemented the Volume of Fluid to Discrete Phase Model (VOF-to-DPM), which combines the two models, effectively allowing spray/droplet generation and tracking as the model progresses.

i. Large Eddy Simulation

Large Eddy Simulation (LES) models turbulence. The LES model resolves large eddies as they incorporate momentum, mass, and energy, and are heavily influenced by the geometry and boundary conditions in the model. Large eddies in this context are those comparable to the

length of the mean flow of the model (our domain length was 0.1 m). Meanwhile, small eddies are more universal when modeling turbulence. The LES governing equations are formulated from time-dependent Navier-Stokes equations, which are filtered in either Fourier (wave number) space or configuration (physical) space. Filtering removes eddies with scales that are too small for the grid spacing in Fluent. Equation 3 does not include gravity, as gravity is independently defined in the operating conditions of Fluent and is treated as a source term. Once gravity is activated, Fluent will redefine other equations to include it. Coriolis is also absent but can be added to Fluent through a User-Defined Function, which allows the addition of parameters to any Fluent model. The following equations are those used for incompressible flows.

After filtering the Navier-Stokes equations, the following equations remain:

$$\frac{\partial \rho}{\partial t} + \frac{\partial}{\partial x_i} (\rho \bar{u}_i) = 0 \quad (4)$$

$$\frac{\partial}{\partial t} (\rho \bar{u}_i) + \frac{\partial}{\partial x_j} (\rho \bar{u}_i \bar{u}_j) = \frac{\partial}{\partial x_j} (\sigma_{ij}) - \frac{\partial \bar{p}}{\partial x_i} - \frac{\partial \tau_{ij}}{\partial x_j} \quad (5)$$

where u is the fluid velocity vector, ρ is the fluid density, p is the fluid pressure, σ_{ij} is the stress tensor caused by molecular viscosity, which is defined by:

$$\sigma_{ij} \equiv \left[\mu \left(\frac{\partial \bar{u}_i}{\partial x_j} + \frac{\partial \bar{u}_j}{\partial x_i} \right) \right] - \frac{2}{3} \mu \frac{\partial \bar{u}_l}{\partial x_l} \delta_{ij} \quad (6)$$

where μ is viscosity and δ_{ij} is the Kronecker delta.

τ_{ij} is the subgrid-scale stress, which is defined by:

$$\tau_{ij} \equiv \rho \overline{u_i u_j} - \rho \bar{u}_i \bar{u}_j \quad (7)$$

Subgrid-scale stresses after filtering are not determined until after modeling. Turbulence models for subgrid-scales use the Boussinesq hypothesis, which calculates stresses from the following equation:

$$\tau_{ij} - \frac{1}{3}\tau_{kk}\delta_{ij} = -2\mu_t\bar{S}_{ij} \quad (8)$$

where μ_t is the subgrid-scale turbulent viscosity, τ_{kk} is the isotropic portion of the subgrid-scale stresses, and \bar{S}_{ij} is the rate-of-strain tensor for the resolved scale. \bar{S}_{ij} is defined as:

$$\bar{S}_{ij} \equiv \frac{1}{2}\left(\frac{\partial\bar{u}_i}{\partial x_j} + \frac{\partial\bar{u}_j}{\partial x_i}\right) \quad (9)$$

For compressible flows, the Navier-Stokes equation is filtered using a density-weighted filtering operator:

$$\tilde{\phi} = \frac{\overline{\rho\phi}}{\bar{\rho}} \quad (10)$$

where ϕ is the subgrid-scale turbulent flux of a scalar.

The subgrid stress tensor for compressible flow is as follows:

$$\tau_{ij} = \bar{\rho}\tilde{u}_i\tilde{u}_j - \bar{\rho}\tilde{u}_i\tilde{u}_j \quad (11)$$

The tensor term can be split into isotropic and deviatoric parts:

$$\tau_{ij} = \underbrace{\tau_{ij}}_{\text{deviatoric}} - \frac{1}{3}\tau_{kk}\delta_{ij} + \frac{1}{3}\tau_{kk}\delta_{ij} \quad (12)$$

deviatoric isotropic

The deviatoric part of the tensor uses the compressible method of the Smagorinsky model, which is as follows:

$$\tau_{ij}^r - \frac{1}{3}\tau_{kk}\delta_{ij} = -2\nu_t\bar{S}_{ij} \quad (13)$$

where ν_t is the turbulent eddy viscosity and \bar{S}_{ij} is the rate-of-strain tensor, which is defined as:

$$\bar{S}_{ij} = \frac{1}{2} \left(\frac{\partial \bar{u}_i}{\partial x_j} + \frac{\partial \bar{u}_j}{\partial x_i} \right) \quad (14)$$

A scalar's subgrid-scale turbulence is modeled using a subgrid-scale turbulent Prandtl number:

$$q_j = - \frac{\mu_t}{\sigma_t} \frac{\partial \phi}{\partial x_j} \quad (15)$$

where q_j is the subgrid-scale flux.

We use the Wall-Adapting Local Eddy-Viscosity (WALE) model to model eddy viscosity, which is calculated using:

$$\mu_t = \rho L_s^2 \frac{(S_{ij}^d S_{ij}^d)^{3/2}}{(\bar{S}_{ij} \bar{S}_{ij})^{5/2} + (S_{ij}^d S_{ij}^d)^{5/4}} \quad (16)$$

where L_s and S_{ij}^d are:

$$L_s = \min (\kappa d, C_\omega V^{1/3}) \quad (17)$$

and

$$S_{ij}^d = \frac{1}{2} (\bar{g}_{ij}^2 + \bar{g}_{ji}^2) - \frac{1}{3} \delta_{ij} \bar{g}_{kk}^2, \bar{g}_{ij} = \frac{\partial \bar{u}_i}{\partial x_j} \quad (18)$$

where κ is the Kármán constant (0.41) and C_ω is the WALE constant (0.325) Fluent uses a default value of 0.325 for the WALE constant because it has been tested and found to yield satisfactory results for a wide range of flows. (*ANSYS Theory Guide 19.2*, 2018). Kulyakhtin et al. (2014) used both RANS, which was previously typically used in wave modeling, as well as

LES, and reported that the results were similar. Jiang et al. (2019) also used LES to model wave interaction.

ii. Volume of Fluid

The VOF model tracks the interface between phases in the model. To do so, a continuity equation is calculated for the volume fraction of each phase. The following equation is used for the q^{th} phase:

$$\frac{1}{\rho_q} \left[\frac{\partial}{\partial t} (\alpha_q \rho_q) + \nabla \cdot (\alpha_q \rho_q \vec{v}_q) \right] = S_{\alpha_q + \sum_{p=1}^n (\dot{m}_{pq} - \dot{m}_{qp})} \quad (19)$$

where \dot{m}_{qp} is the mass transfer from the q phase to the p phase. \dot{m}_{pq} is the mass transfer from the p phase to the q phase. S_{α_q} , the source term on the right side, is zero.

We use an explicit solver, in which the standard finite-difference interpolation schemes are applied to the volume fraction values from equation 16 (*ANSYS Theory Guide 19.2*, 2018).

$$\frac{\alpha_q^{n+1} \rho_q^{n+1} - \alpha_q^n \rho_q^n}{\Delta t} V + \sum_f (\rho_q U_f^n \alpha_{q,f}^n) = [\sum_{p=1}^n (\dot{m}_{pq} - \dot{m}_{qp}) + S_{\alpha_q}] V \quad (20)$$

where $n+1$ is the index for the current time step, n is the index for the previous time step, $\alpha_{q,f}$ is the face value of the q^{th} volume fraction, V is the volume of the cell, and U_f is the volume flux through the face.

Energy and momentum are calculated throughout the domain by Fluent, which means the velocity fields are shared by the phases in the model. Because of this, the momentum equation depends on ρ and μ of the phase volume fraction, as shown below:

$$\frac{\partial}{\partial t} (\rho \vec{v}) + \nabla \cdot (\rho \vec{v} \vec{v}) = -\nabla p + \nabla \cdot [\mu (\nabla \vec{v} + \nabla \vec{v}^T)] + \rho \vec{g} + \vec{F} \quad (21)$$

where p is the static pressure, ρg and \vec{F} are the gravitational body force and external body forces.

The energy equation is as follows:

$$\frac{\partial}{\partial t}(\rho E) + \nabla \cdot (\vec{v}(\rho E + p)) = \nabla \cdot (k_{eff} \nabla T) + S_h \quad (22)$$

where κ_{eff} is the effective conductivity, S_h includes defined volumetric heat sources, and energy, E , and temperature, T , are considered mass-averaged variables in Fluent. Mass averaged energy is calculated as follows:

$$E = \frac{\sum_{q=1}^n \alpha_q \rho_q E_q}{\sum_{q=1}^n \alpha_q \rho_q} \quad (23)$$

where E_q for each phase depends on the specific heat and temperature of the phases, defined by:

$$E_q = h_q - \frac{p}{\rho_q} + \frac{v^2}{2} \quad (24)$$

where h_q for each phase is based on the specific heat of that phase and the shared temperature. The continuum surface force (CSF) model by Brackbill et al. (1992) is used to model surface tension (*ANSYS Theory Guide 19.2*, 2018).

We use Fluent's open channel flow boundary condition in the VOF model for the waves in our model. Open channel flows are controlled by gravity, inertia forces, and interfacial stresses. The Froude number, which is the ratio of inertia force and hydrostatic force, characterizes the flow:

$$Fr = \frac{V}{\sqrt{gy}} \quad (25)$$

where V is the velocity magnitude, g is gravity, and y is the distance from the bottom to the free surface. The wave speed is calculated as:

$$V_w = V \pm \sqrt{gy} \quad (26)$$

An incident wave profile is calculated as follows:

$$\zeta = A \cos(k_x x + k_y y - \omega_e t + \epsilon) \quad (27)$$

where z is the wave height, A is the wave amplitude, ϵ is the phase difference, t is the time, and k_x and k_y are the wave numbers in the x and y directions. Therefore,

$$k_x = k \cos \theta \quad (28)$$

and

$$k_y = k \sin \theta \quad (29)$$

where θ is the wave heading angle, defined as the angle between the wave front and direction of wave propagation. The wave number k is calculated as:

$$k = \frac{2\pi}{\lambda} \quad (30)$$

where λ is the wavelength and the effective wave frequency ω_e is calculated as:

$$\omega_e = \omega + kU \quad (31)$$

U is the averaged velocity of the flow current, and ω is the intrinsic wave frequency, which is defined as:

$$\omega = \sqrt{gk \tanh(kh)} \quad (32)$$

where h is the liquid height and g is the gravity magnitude (*ANSYS Theory Guide 19.2*, 2018).

The VOF model was first developed by Hirt and Nichols (1981) in order to overcome the problem of modeling two-phases. Following this approach, many researchers have used the VOF model in CFD modeling. Specifically, Kulyakhtin (2014), Hamza et al. (2015), Kim et al. (2016), Zhang et al. (2016), Jiang et al. (2019), and Uddin et al. (2020) used ANSYS Fluent's VOF model to study wave tank simulations.

iii. Discrete Phase Model

The Euler-Lagrange approach is used in Fluent's DPM. Navier-Stokes equations are again solved for this model. The dispersed phase, in our case droplets, can exchange momentum, mass, and energy with the primary phase (water). The droplet trajectories are computed by Fluent at a specified interval (in our case 20 adaptive time steps ranging from 10^{-9} to 10^{-6} s), by using force balance in a Lagrangian reference frame. This is calculated as:

$$\frac{du_p}{dt} = F_D(u - u_p) + \frac{g_x(\rho_p - \rho)}{\rho_p} + F_x \quad (33)$$

where F_x is an additional acceleration term, $F_D(\mu - \mu_p)$ is the drag force per unit particle mass and F_D is as follows:

$$F_D = \frac{18\mu}{\rho_p d_p^2} \frac{C_D Re}{24} \quad (34)$$

where u is the fluid phase velocity, u_p is the particle velocity, μ is the molecular viscosity of the fluid, ρ is the fluid density, ρ_p is the density of the particle, and d_p is the particle diameter. Re is the Reynolds number, which is calculated as:

$$Re \equiv \frac{\rho d_p |u_p - u|}{\mu} \quad (35)$$

In Fluent, the drag coefficient, C_D , for smooth particles is calculated as:

$$C_D = a_1 + \frac{a_2}{Re} + \frac{a_3}{Re} \quad (36)$$

where a_1 , a_2 , and a_3 are constants that are used over several ranges of Re by Morsi & Alexander (1972) (*ANSYS Theory Guide 19.2*, 2018). Note that this does vary from the traditional drag coefficient formula (Eq. 2).

iv. VOF-to-DPM

The VOF-to-DPM is an innovative model from Fluent that allowed us to generate sea spray down to micrometers of diameter through dynamic mesh adaption. The model combines two of Fluent's models: VOF and DPM. The DPM model tracks particles which are formed through specified parameters by Lagrangian tracking methods. Various model specific settings within the VOF-to-DPM were set as follows. Particles were set to interact with the continuous phase (water). The model tracked steady and unsteady particles and tracked the particles with the fluid flow time step. The model was set to allow secondary breakup of particles as well. Fluent injects particles as a part of DPM model, so to account for particles without injecting any material, we set the injection time at a very high start and stop time as a placeholder. This allowed the VOF-to-DPM generated particles to be tracked instead of injected material. The particle material was set to water, and density was set to that of seawater. Using the VOF model, we set two phases (air and water) with explicit formulation and sharp/dispersed interface modeling, which are recommended in Fluent when modeling multiphase environments. Explicit formulation accurately calculates curvature and is therefore crucial when modeling surface tension. Waves were set up using the open channel flow and open channel wave feature of this model. These settings allow open channel flow with inertia and gravity currents within the domain and waves to be modeled using wave theories. For our purposes, Fifth Order Stokes wave theory was used as it fit the waves set up in the model. Fifth Order Stokes theory uses Fenton's (1985) expansion term $kH/2$. Zhang et al. (2016) also used the open channel flow, but with second-order Stokes waves to study their wave tank experiments.

The phase interactions were set to a constant surface tension, dependent on whether surfactants were introduced, or the water was clean. The phase model transitions were set to transfer water parcels tracked by VOF to Lagrangian particles set by DPM. This transition was specified to allow parcels that were within the volume-equivalent sphere diameter range of 0 to 0.005 m and upper limits of asphericity, as calculated by the radius standard deviation of 0.5 and radius surface orthogonality of 0.5. It also split any lumps that exceeded the cell volume by a factor of 10. A schematic of this transition is shown in Figure 12. These settings will influence the generated spray but were set as recommended by researchers at ANSYS Fluent. DPM particles are tracked with the primary phase (air) and are not affected by the air-water interface. While they are an important factor to tropical cyclone intensity, evaporation and heat fluxes of

spray are not included in this model. The mesh was coarsened immediately after lump conversion to save computational power. Mesh adaption was set based on the curvature of the volume fraction of water within each mesh cell. It was applied to coarsen and refine every two time-steps, up to 10 levels per cell in the x, y, and z direction. When lumps are converted to DPM particles, the mesh coarsens to the original mesh size. According to Eggers (1997), the timescale for breakup of free surface flows is on the order of 10^{-2} s. The time step in the ANSYS Fluent model was in the range of 10^{-9} to 10^{-6} s, which is several orders of magnitude less than the timescale for breakup of free surface flows. This is more than enough to capture any fast transients during the interface breakup. This approach dramatically reduces the initial mesh size, which in turn allows for a larger domain (ANSYS Theory Guide 19.2, 2018).

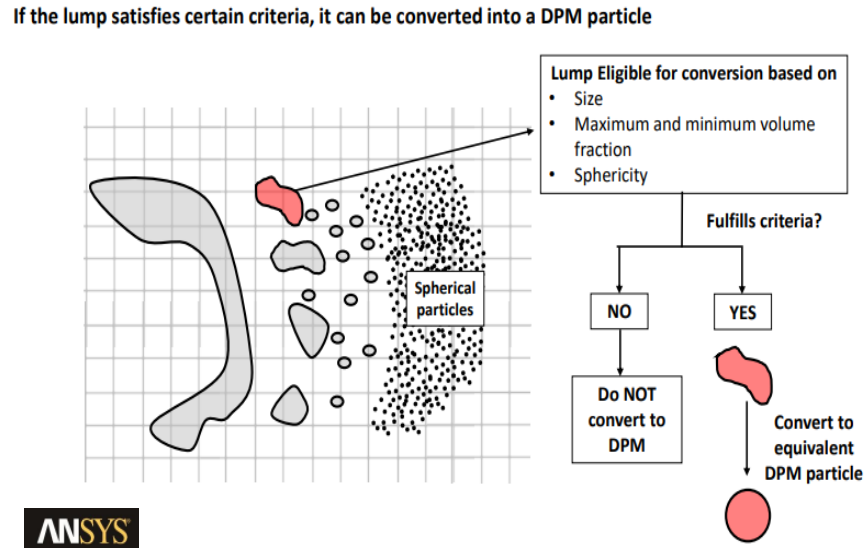


Figure 12. Transition criteria from VOF lump to DPM particle in ANSYS Fluent VOF-to-DPM model (ANSYS, Inc.).

Because the VOF-to-DPM is a new implementation by Fluent, there are no previous ocean applications of this model in the literature. We have closely collaborated with researchers at ANSYS to select the proper settings for this simulation.

v. Model Setup

The model domain, shown in Figure 13, was created in ANSYS Workbench and consisted of a 0.1 m (x) by 0.1 m (y) by 0.05 m (z) cube with an initial mesh size of 0.002 m.

Future work will increase this domain size along with implementing heat fluxes. The small domain allows us to accurately generate spray on a small scale, but of course wave processes and eddies are limited by this small domain. Increasing our domain size will generate more realistic spray droplets as waves will have time to mature. The initial mesh was then adapted, as previously described, allowing for remeshing down to tens of micrometers at the air-sea interface. Boundary conditions were set to zero shear on lateral sides and bottom of the domain. The domain contained air and water, with the water being initialized with waves with a 0.005 m height and 0.05 m length from the inlet. Wind stress was applied at the top of the domain. This was set according to the strength of tropical cyclone conditions being modeled, 4 Nm^{-2} for Category 1, 10 Nm^{-2} for Category 3, and 20 Nm^{-2} for Category 5. The initialized waves were set up before setting periodic boundary conditions at the inlet and outlet to allow the waves to propagate through the domain.

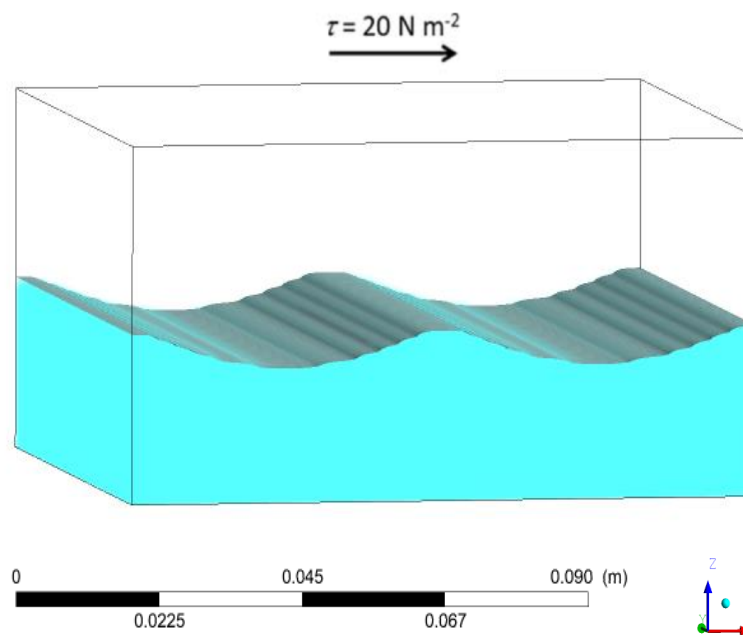


Figure 13. Initial model setup shown in ANSYS Fluent.

The model was run in parallel on 264 processors on a 564 core HPC Linux cluster with 12 compute nodes. We used a pressure-based, transient, 1st order implicit solver, and LES to model turbulence. Operating conditions were set to 20°C, 9.81 m s^{-1} gravity, and atmospheric pressure $p=101325 \text{ Pa}$. Operating conditions are used with the Boussinesq approximation in Fluent, not for specific fluid or solid materials. This is acceptable in Fluent when temperature

gradients in the model are not large. We specified the materials in our domain as water with a bulk temperature $T=298$ K, density $\rho=1000$ kg m⁻³, viscosity $\mu = 0.001003$ kg·m⁻¹·s⁻¹, and specific heat $c_p=4182$ J kg⁻¹ K⁻¹, and air with bulk temperature $T=298.15$ K, density $\rho=1.225$ kg m⁻³, viscosity $\mu = 1.7894e^{-05}$ kg·m⁻¹·s⁻¹, and specific heat $c_p=4182$ J kg⁻¹ K⁻¹. Temperatures did not change during the simulation. For this model humidity was not introduced, but when heat fluxes and evaporation are implemented, humidity will be as well. Also note that these conditions are not identical to the laboratory experiment. A future model run using the same domain size, waves, and conditions as the laboratory experiment may provide more experiment specific results for comparison.

A sensitivity model experiment with 10%, 25%, and 50% reductions were conducted. A 50% reduction of surface tension resulted in a stronger effect of surfactants on spray generation than a 25% reduction, while a 10% reduction of surface tension resulted in a lesser effect of surfactants than the 25% reduction. The 25% reduction was selected based on the King et al. (2019) report on surface tension measurements in the coastal North Sea in the presence of surfactants. The surface tension to introduce surfactants was therefore set to 0.054 N/m, while the clean water's surface tension was set to 0.072 N/m.

Time steps within the model were set to adaptive, meaning the time step was automatically adjusted based on the global Courant number. Doing this allowed the time step to determine the stability for the speed of the solution. Each case of the model was run until a flow time of 0.159 s after spray generation began was achieved. For Category 5, this was a total flow time of 0.265 s (surfactants) and 0.263 s (clean water). For Category 3 the total flow time reached 0.286 s in both surfactant and clean water cases, and Category 1 reached 0.32 s in both cases. Note that running this model for a longer time would yield variation in results (likely more realistic, since this flow time was extremely short), but due to computational limitations, this model run was already lengthy because of the very small time-step involved.

c. Data Analysis

Images from the University of Miami laboratory experiment were first processed using the *Dantec Dynamics* shadow imaging software package to remove some background noise and focus on the spray droplets taken during the experiment. The software calculated the mean light

intensity of each set of 250 images and then normalized each image based on the mean image to remove background noise, increase contrast, and make particle detection easier. The images were then analyzed using MATLAB to determine how many pixels each spray droplet image was in the x and y direction. The average diameter was calculated for each spray droplet (1 pixel = 42 μm) to determine the size distribution (in terms of radius). The diameters of the spray particles produced by the CFD models were exported from ANSYS Fluent as a data file. Data files containing CFD model spray diameters and laboratory experiment spray diameters were analyzed in MATLAB using histograms, plots, and normalization to calculate spray radius probability distributions. For model verification, probability distribution plots were created in MATLAB from the laboratory data. Images marked using this method can be seen in Figure 14. This detection method could have missed detection of very small particles but marking by hand eliminated automatic detection error and made for more accurate results.

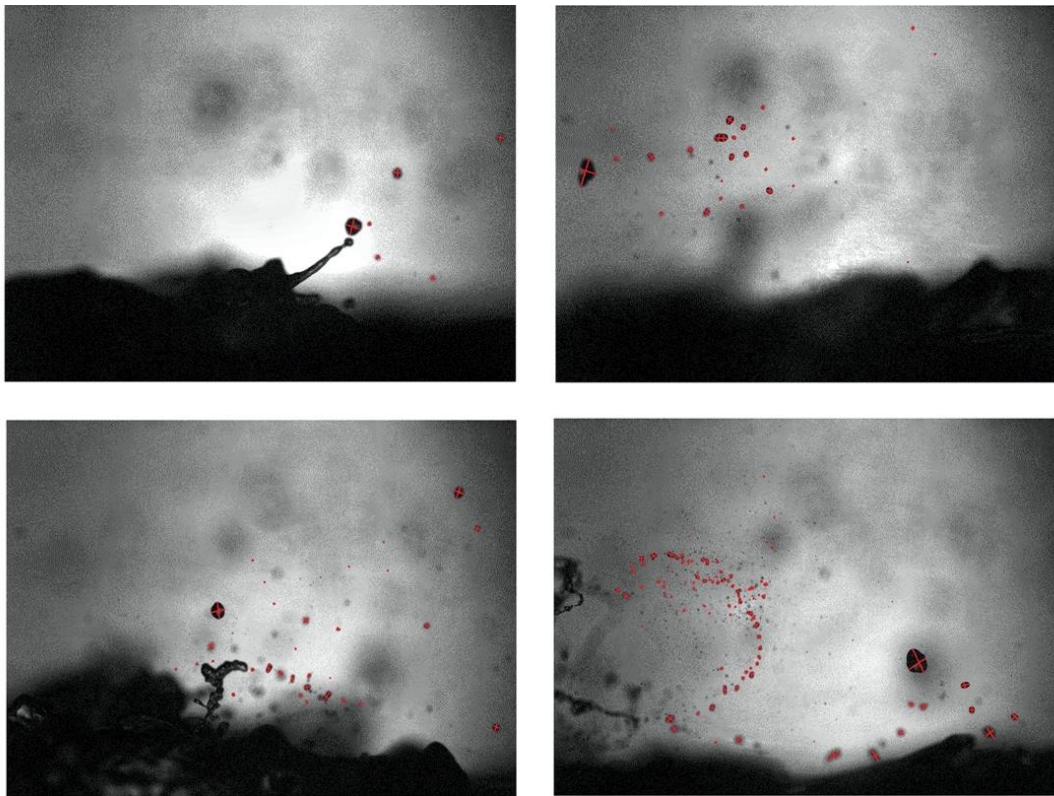


Figure 14. Data processing of images taken during the laboratory experiment at SUSTAIN.

The diameters of the spray particles produced by the CFD models were exported from ANSYS Fluent as a data file. These files were then converted to txt files for data analysis. The raw particle count for these files for the first half and second half of the trial (flow time, not time-step) is noted in Table 2. Note here that there was a drastic increase in spray generation in the second half of all trials. Files containing CFD model spray diameters and laboratory experiment spray diameters were analyzed in MATLAB using histograms, plots, and normalization to calculate spray size distributions. Probability plots were also created in MATLAB from the data.

Table 2. Raw spray data from ANSYS Fluent model.

Conditions	1st half of run	2nd half of run	Total Spray Count
Category 1 clean water	12	9522	9534
Category 1 surfactant	94	13784	13878
Category 3 clean water	94	41949	42043
Category 3 surfactant	382	55870	56252
Category 5 clean water	325	59265	59590
Category 5 surfactant	323	80728	81051

Spray droplet size distribution was calculated as:

$$n(r) = \frac{dN(r)}{dr} \quad (37)$$

where dN is the derivative of the total number drops with radius (r), and dr is the radius increment (Veron et al. 2015). Spray size distributions were completed for both surfactant and normal surface tension conditions in both the models and the laboratory results. Intra-comparison between the laboratory experiment and comparable model (Category 1) were also completed by plotting and analyzing this data together. Comparison to other laboratory experiments, including Veron et al. 2012, was also done for further verification of the model. Confidence intervals (CI)

were calculated for each trial of the laboratory experiment and model and can be viewed in the result plots. CI's were also calculated between the model and laboratory results for both clean water and surfactant cases under Category 1 tropical cyclone conditions (Table 3) using the t statistic and two sample means (M_1 and M_2) to generate an interval estimate of the difference between the two population means ($\mu_1 - \mu_2$) in the following equation:

$$\mu_1 - \mu_2 = (M_1 - M_2) \pm ts_{(M1-M2)} \quad (38)$$

Table 3. Confidence intervals between laboratory and modeling experiments

Trial	Lower CI	Upper CI
Model vs laboratory - clean water	0.00018469	0.00029131
model vs laboratory - surfactant	0.00008682	0.00016518

Further statistical comparison between the model and the laboratory experiment was done through quantile-quantile (QQ) plots of the measured and modeled spray size distributions. This aided in determining how well the modeled spray size distribution fits to the experimental data. Statistical analyses were performed using MATLAB.

d. Satellite Imagery

Analysis of color satellite images included coupling the satellite images taken from NASA Aqua MODIS and NOAA VIIRS from the NOAA ERDDAP database online and comparing with data from Weather Underground to comprehensively analyze chlorophyll concentration before, during, and after the passage of various tropical cyclones.

The NASA Aqua satellite carries six instruments and was launched in 2002. Initially, the mission was planned for a six-year lifespan, but it is currently still collecting data from five of the original six instruments (AIRS, AMSU, CERES, MODIS, and AMSR-E). The sixth instrument, HSB, stopped collecting data in 2003. Currently, NASA expects Aqua to continue operations into the 2020s, as there are no current system issues (Graham 2019). Using MODIS, the satellites are able to collect data on the chlorophyll-a concentration (in mg m^{-3}) in the near-surface waters of the ocean. This is accomplished through the use of an empirical relationship

derived from in situ chlorophyll-a measurements and blue-to-green band ratios from reflectance of remote sensors (Maccherone 2018).

The Visible Infrared Imaging Radiometer Suite (VIIRS), located onboard the Suomi NPP and NOAA-20 satellites, is a crucial data collection instrument. VIIRS uses visible and infrared imagery to collect data from land, and in the atmosphere, cryosphere, and oceans. VIIRS covers wavelengths from 0.41 to 12.5 microns using 22 imaging and radiometric bands (Bai 2019).

Satellite data were collected for the specific coordinates of the tropical cyclone path during the dates of its passage. The hurricane tracks were then drawn in Google Maps according to maximum wind speed and category and exported as an xml file. They were then imported to Google Earth and analyzed with the corresponding satellite data to emphasize and reveal any correlation between higher chlorophyll concentration and intensity of the storm. Future considerations should include considering storm radii when choosing the resolution of chlorophyll satellite data.

Synthetic aperture radar (SAR) was also looked at as a potential tool for tropical cyclone prediction. Internal waves, ship wakes, oil spills, and convergence zones are all identifiable using SAR (Alpers and Hühnerfuss 1988, Gade et al. 2013). SAR, which is an advanced remote sensing satellite, has high ground resolution and is able to work in almost any weather conditions because it can penetrate cloud cover (Gade et al. 2013). SAR captures the surface of the ocean by collecting the backscatter of microwaves (Fig. 15), which depends on sea surface roughness, and therefore wind speed (Lehner et al. 1998). Because surfactants dampen short gravity-capillary waves, surfactant slicks are visible in SAR imagery as darker areas (Alpers and Espedal 2004).

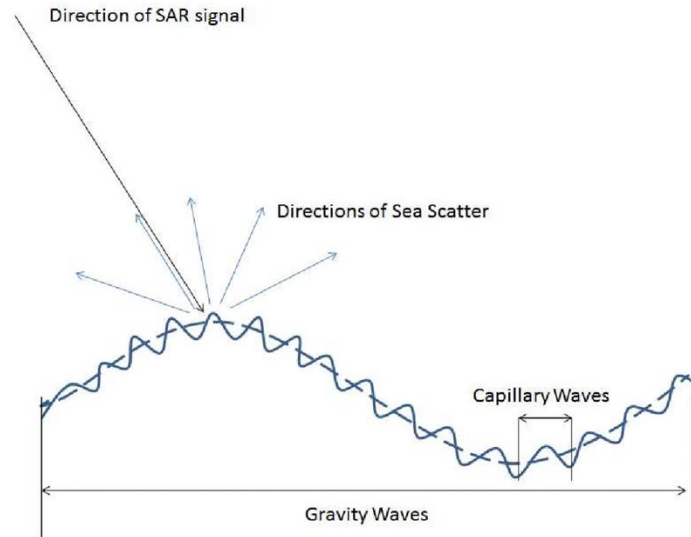


Figure 15. SAR imagery collects backscatter from the sea surface to capture images of the sea surface (Zhang et al. 2017)

5. Results and Discussion

a. Laboratory Experiment

Laboratory experiments at University of Miami SUSTAIN facility (see Methods section) revealed visible differences of spray generation when surfactants were either absent or present. Figure 16 shows images of spray generation in clean water (no surfactants), while Figure 17 shows spray generation when surfactants were present.



Figure 16. Images taken during the laboratory experiment in clean saltwater (no surfactants).



Figure 17. Images taken during the laboratory experiment when surfactants were present.

Spray generation with surfactants appeared to considerably branch out in comparison to clean water, leading to increased spray generation and variation in spray size distribution. The branch-like structures were seen 0.4% of the time in clean water images taken during the laboratory experiment. Likewise, fingerlike structures were rarely seen (1.2% of the time) when surfactants were present. This is due to the reduction of surface tension caused by surfactants. It should be noted that the tank wind stress was extrapolated to $\sim 40 \text{ m s}^{-1}$ and not directly applied. Brockmann et al. (1982) experimented with artificial release of surfactants (oleyl alcohol) on the ocean surface from a helicopter. They found that the concentration of this surfactant at the surface was 0.02 moles / liter. For comparison, our laboratory experiment used an order of magnitude smaller concentration of surfactant, which still had a prominent effect on the spray generation.

b. Volume of Fluid to Discrete Phase Model

Using ANSYS Fluent's VOF-to-DPM, we were able to explore sea spray generation under various conditions, which is difficult to do accurately in the field or laboratory. Applying wind stress to the top of the domain allows the wind to penetrate the sea surface and create turbulence, leading to spray generation, as shown in Figure 18.

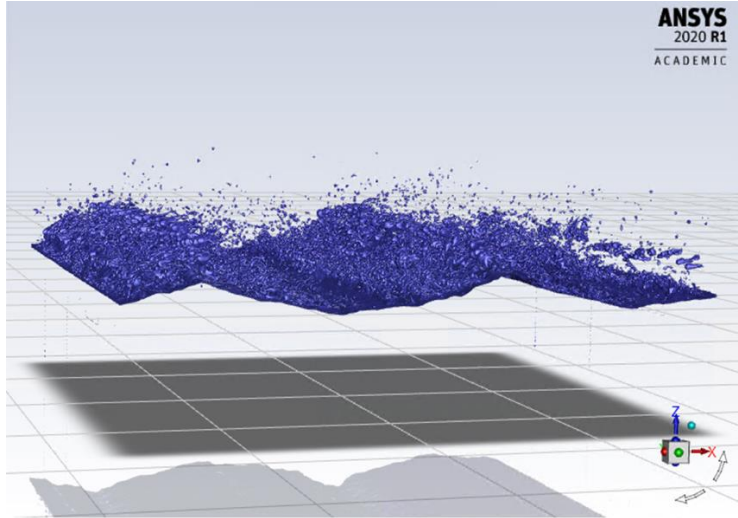


Figure 18. An image of the air-sea interface under Category 5 wind stress within the VOF-to-DPM model in ANSYS Fluent showing the turbulent projections of the water surface.

Mesh adaption, described in the materials and methods section, is crucial to the success of our results. Figure 19 shows a side view of the sea surface from our model overlaid with a cross-section of the domain’s mesh. The mesh refinement at the wave crest can be seen in Figure 19a. This is where most spray is generated, which can be seen in Figure 19b.

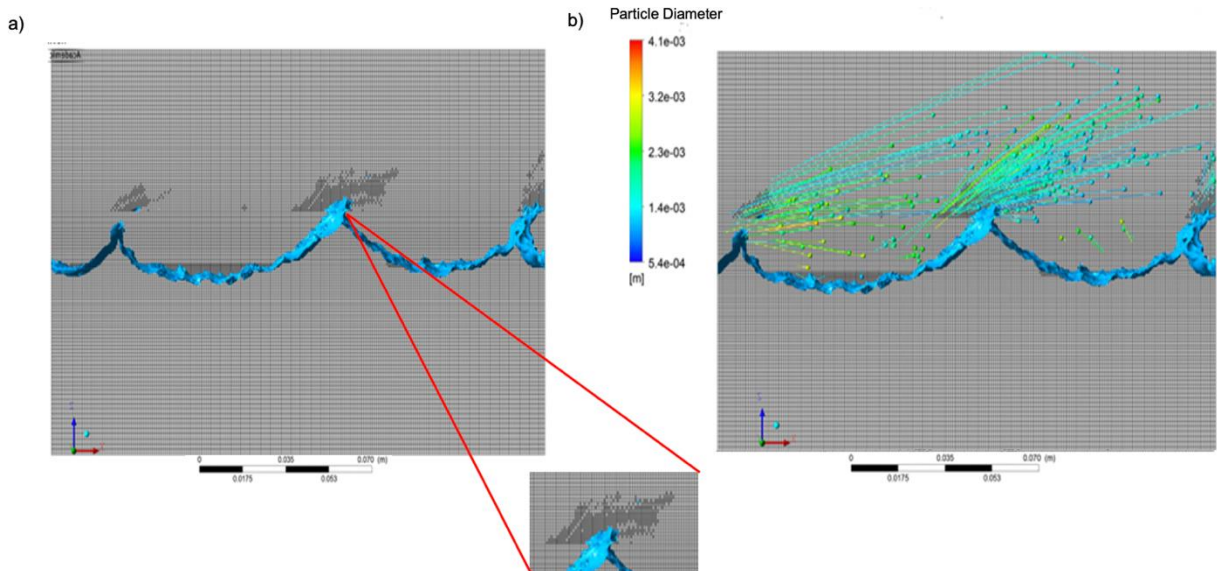


Figure 19. Mesh adaption based on water volume fraction, curvature of parcels, 10 levels of remeshing in each direction, which refines the mesh up to about 1000x in areas of high interest. Insert shows area of remeshing at the wave crest.

A sensitivity experiment was conducted to test various surface tension reductions in the CFD model. The spray generation increased with increasing surfactant reduction; the 50% reduction produced the highest amount of spray, with 25%, 10%, and 0% each producing less consecutively. Figure 20 shows the results from these trials plotted together taken from the model at 0.175 s.

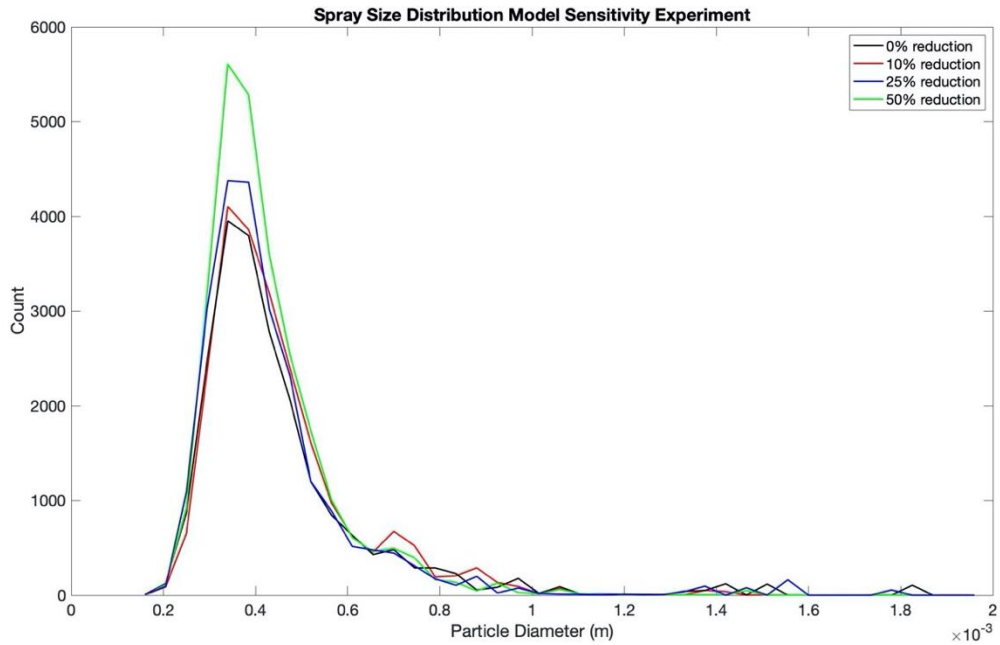


Figure 20. Sensitivity experiment of the VOF-to-DPM model using 50%, 25%, 10% and 0% reductions of surface tension.

Figures 21-24 show the individual results from each trial with confidence intervals.

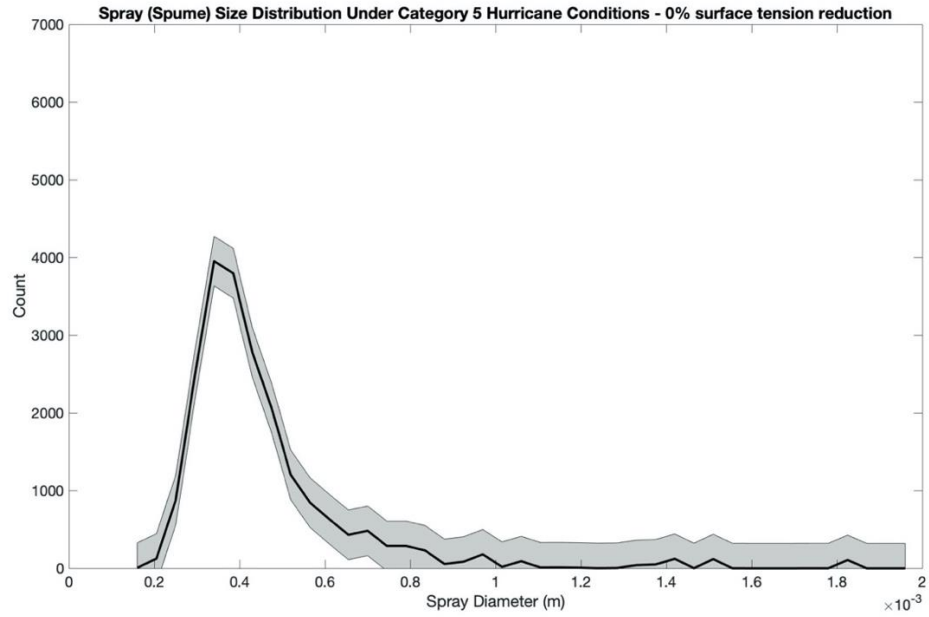


Figure 21. CFD model spray distribution with a 0% surface tension reduction (clean water).

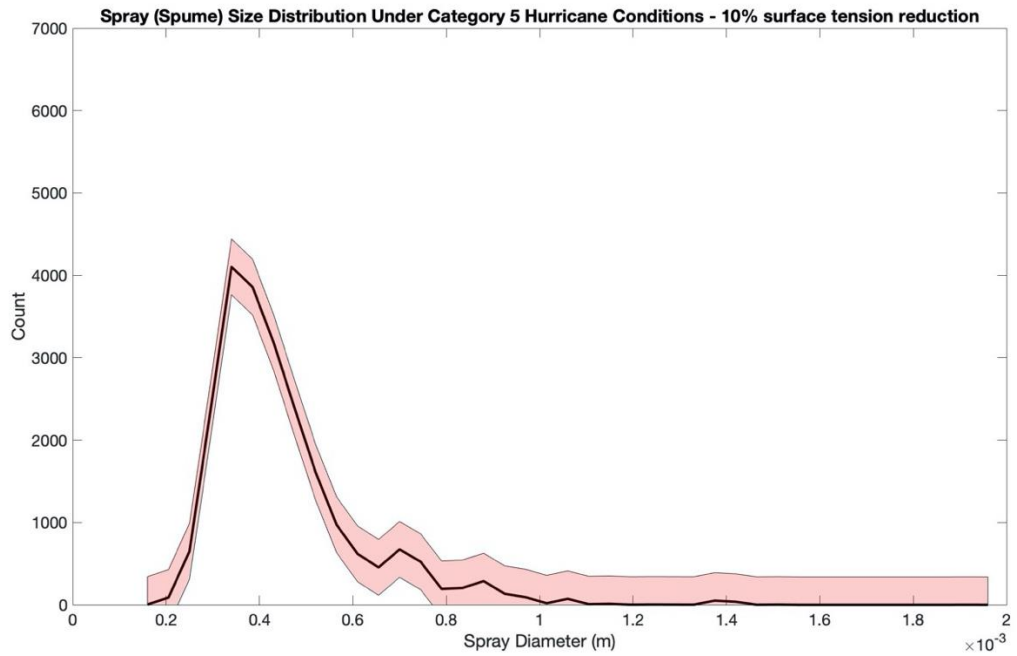


Figure 22. CFD model spray distribution with a 10% surface tension reduction.

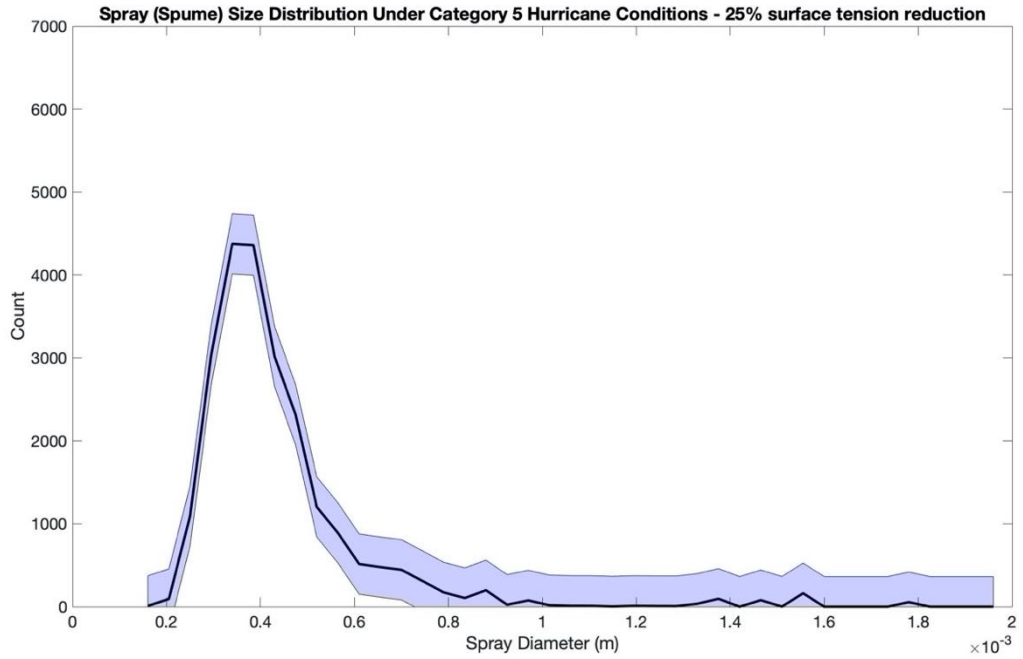


Figure 23. CFD model spray distribution with a 25% surface tension reduction.

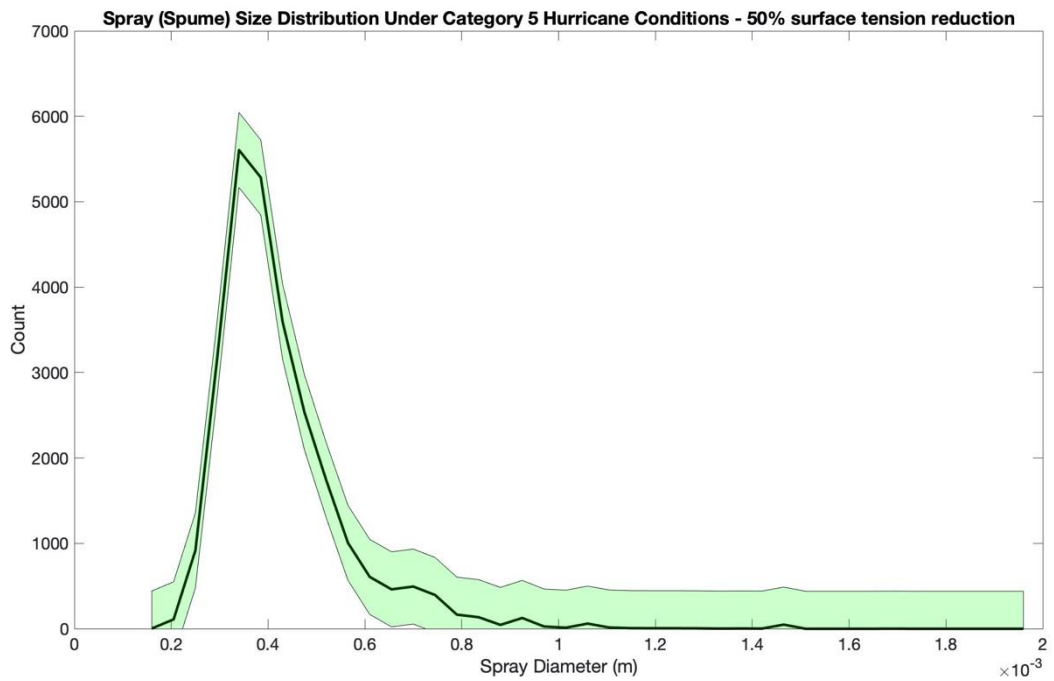


Figure 24. CFD model spray distribution with a 50% surface tension reduction.

One problem in evaluating the effect of surfactants on tropical cyclones is that the abundance of bio-surfactants in the ocean is virtually unknown on a global scale. It is, however, well known that a small amount of surfactant can cover a large surface area (Alpers and Espedal 2004). Measurements of surfactants in the ocean are extremely rare. King et al. (2019) reported surface tension measurements in the coastal North Sea in the presence of surfactants in the range from 0.053 N/m to 0.0681 N/m. Based on these measurements and our sensitivity experiment, we set the surface tension reduction due to the effect of bio-surfactants to 0.054 N/m (25% reduction) compared to the surface tension of clean water 0.072 N/m (0% reduction).

Models must always be confirmed with experimental results in order to ensure their accuracy. The following section reports comparison of this CFD model results with results from the laboratory experiment.

c. Confirmation of VOF-to-DPM with Laboratory Experiments

The laboratory experiments revealed visible differences of spray generation when surfactants were either absent or present (Fig. 25a, b). The VOF-to-DPM transition model in ANSYS Fluent CFD code reproduced similar patterns shown as an isosurface (points of constant value of 0.5 volume fraction of water in the cell) of the water surface in Figure 25c, d. In the absence of surfactants, the mechanism for spume generation resembles a finger-like structure, caused by the KH instability at an interface with a large density difference (Koga 1981, Soloviev et al. 2017, Hoepffner et al. 2011) (Fig 25a, c). When surfactants are present, altering the sea surface through reduced surface tension, the generation of spume occurs differently. Figures 25b and 25d show branch-like formation of spray. This ultimately leads to a different size distribution with a higher abundance of droplets by over 30%.

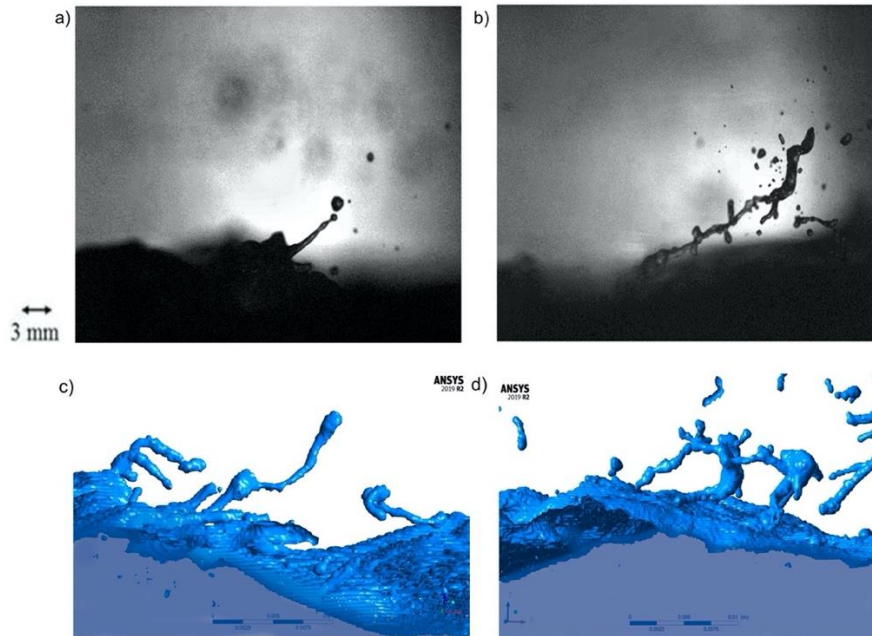


Figure 25. Disruptions of the air-water interface under Category 1 ($U_{10} = 40 \text{ m s}^{-1}$) tropical cyclone conditions a) Finger-like structure formed in the absence of surfactants during the laboratory experiment. b) Branch-like structure formed in the presence of surfactants during the laboratory experiment. c) Finger-like structure shown as an isosurface formed in the absence of surfactants in the VOF-to-DPM model. d) Branch-like structure shown as an isosurface formed in the presence of surfactants in the VOF-to-DPM model.

We compared the Category 1 tropical cyclone wind-forced VOF-to-DPM results with a 4 Nm^{-2} wind stress at the top of the numerical tank to the laboratory experiment with comparable wind stress (extrapolated $U_{10} = 40 \text{ m s}^{-1}$ wind speed used at SUSTAIN). The model shows a higher amount of spray by over 30% in both surfactant and clean water cases than the laboratory experiments (Fig. 26). This is because in the laboratory experiment, the images used for data analysis were taken at one plane of the tank, so a large amount of spray was unaccounted for in these results in comparison to a 3D model that accounts for spray throughout the domain. Increasing sampling variations in future experiments would improve the laboratory results, or sampling model droplets from a single plane (like that in the laboratory experiment) would present comparable results to the current laboratory experiment.

The laboratory experiment was conducted using saltwater ($\sim 33 \text{ psu}$) while the model fluid was set to freshwater. The Nayar et al. (2014) parameterization shows the difference in surface tension between sea and fresh water on level of 1.4%. The density difference is on the level of 2.5%, and molecular viscosity about 7.5%. These cannot explain the significant

difference in foaming between salt and freshwater observed in nature. Katsir and Marmur (2015) explained that saltwater is foamier than freshwater because of the ionic effect related to different coalescence properties of air-bubbles in sea and fresh water. The KH instability produces mostly large spray particles (spume), which is not directly related to bubble dynamics.

The initial mesh resolution in the numerical domain is 0.002 m. Dynamic mesh adaption locally increases mesh resolution allowing the VOF-to-DPM to accurately resolve spray radius distributions starting from $\sim 100 \mu\text{m}$ (Fig. 26a). Laser imaging techniques used in the laboratory experiment resolved spray radii larger than $30 \mu\text{m}$ (Fig. 26b) and were used to estimate spatial resolution of the model.

For Category 1 tropical cyclone conditions, the laboratory experiment revealed a 39% increase in spray concentration in the range of radii from $100 \mu\text{m}$ to $500 \mu\text{m}$ when surfactants were present (Fig. 26a). The model indicated a 34% increase in spray between clean water and surfactant presence for the same conditions and the same range of radii (Fig. 26b).

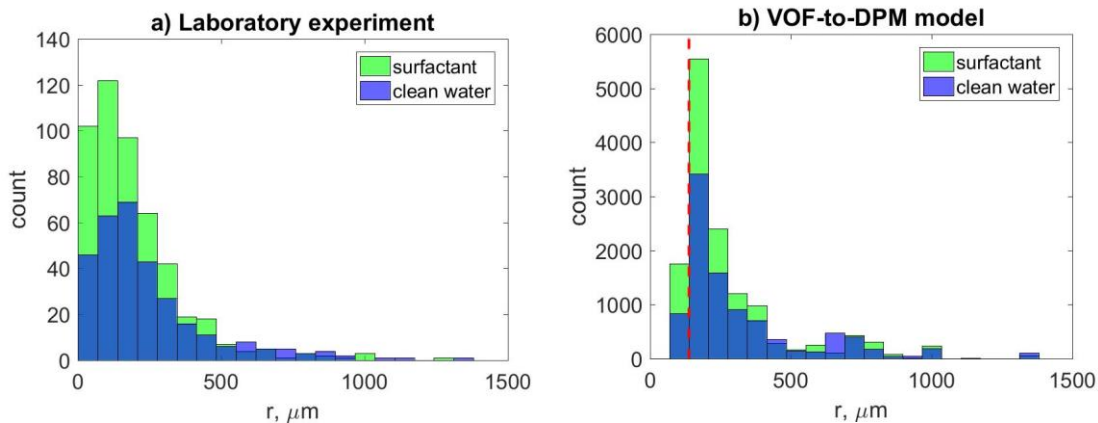


Figure 26. Histograms showing the spray radius distribution under Category 1 tropical cyclone conditions for a) the laboratory experiment and b) the VOF-to-DPM. The vertical dashed line shows the lower resolution limit of the model. The y-axis scale for the model is substantially larger than for the laboratory experiment (see explanation in the text).

Figure 27 shows the data as a line plot with the 95% confidence intervals for each case. The confidence intervals increase for spray radius distributions above $500 \mu\text{m}$, meaning this data is less informative in the comparison between laboratory and model results. Again, there is an obvious increase in spray generation when surfactants are present in both the laboratory and model results.

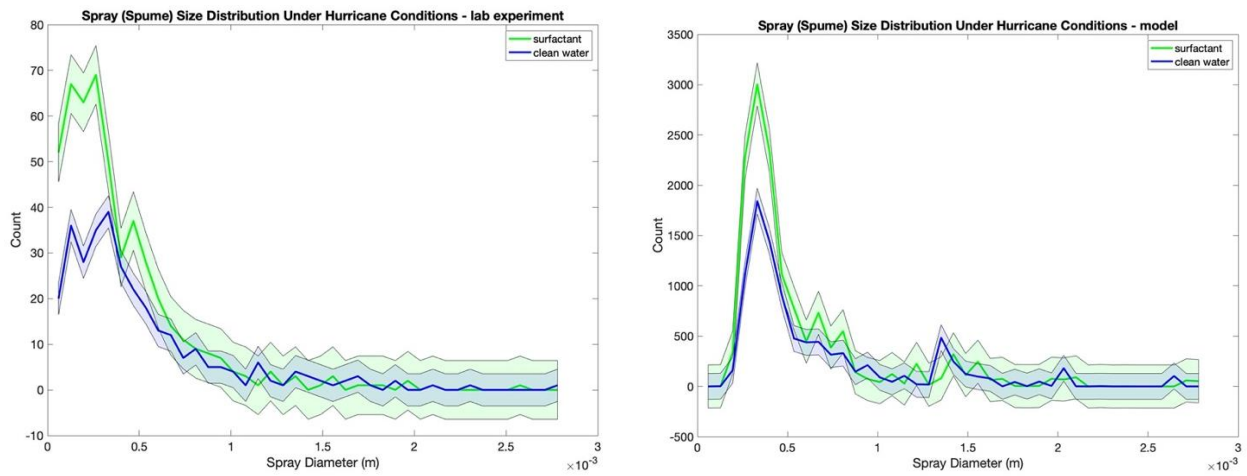


Figure 27. Line plots of the laboratory and modeling results of when surfactants were present and absent (clean water) with 95% confidence intervals.

Figure 28 shows the probability distribution function (pdf) line for the entire range of the model and laboratory results directly calculated from the histograms in Figure 19. The pdf line shows the continuous data from the experiments, while histograms show the discrete data. The pdf in Figure 28 shows the probability that the measurement lies within the range of the histogram bins.

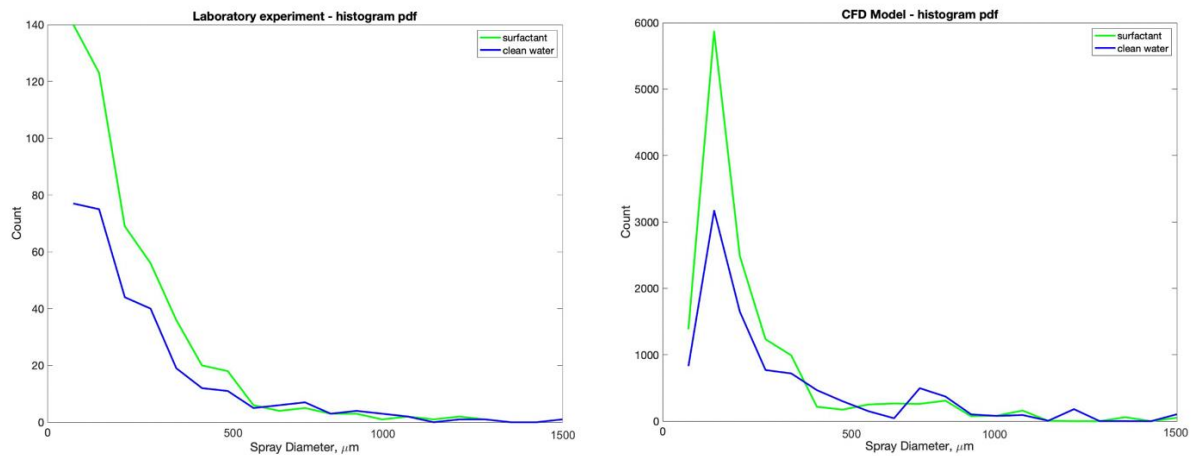


Figure 28. PDF lines from histograms of both the laboratory (left) and model (right) results for clean water and surfactant trials.

The pdf was then determined for the spray radii between 0 and 500 μm in Figure 29. This figure shows confirmation of the model with the laboratory data using the pdf of spray radii (shown on the y axis). For both clean water and surfactant cases the model results and laboratory experiment data generally follow the same pdf. The pdf specifies that probability that the spray radii lies within certain values, rather than specific values. We can see in Figure 29 that the model and laboratory spray radii when surfactants are present and absent follow similar probability, being that it is more probable for smaller ($<200 \mu\text{m}$) radii to generate. When surfactants are present, both in the laboratory and model, it is slightly (~ 0.02 for the laboratory and ~ 0.08 for the model) more likely that smaller spray will generate than in clean water. As radii increases, surfactants do not seem to impact the spray size distribution as much, but they still affect abundance as seen in Figure 26. Figure 30 shows the pdf with confidence intervals, revealing that as spray radii increases, the confidence intervals become larger, meaning the certainty for these results at higher radii is lower.

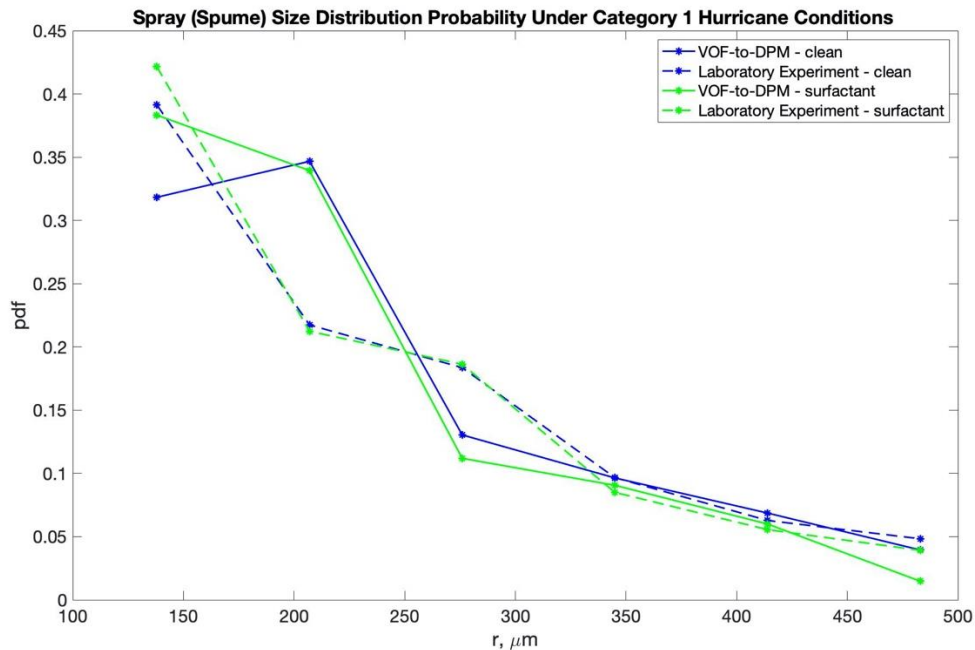


Figure 29. Probability density of spray radius distributions for clean water and surfactants in the laboratory experiment (dashed line) and VOF-to-DPM (continuous line) under Category 1 tropical cyclone conditions.

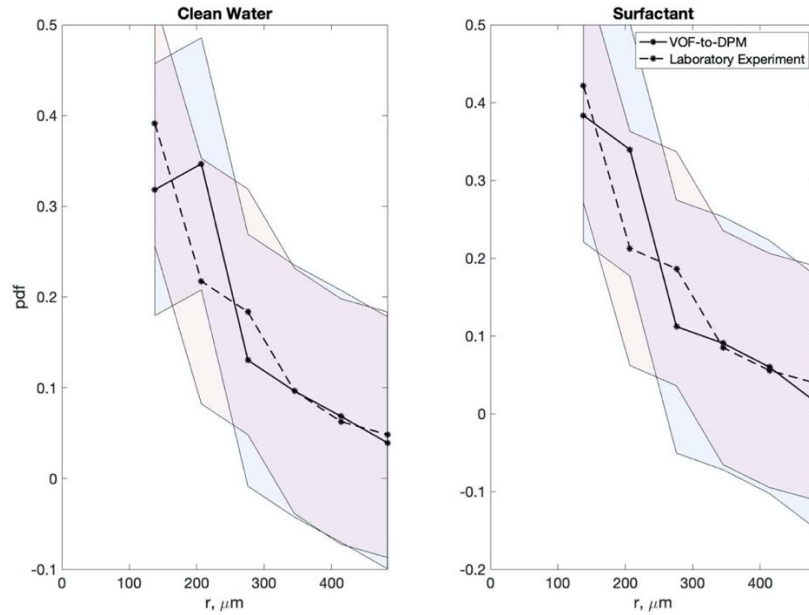


Figure 30. PDF including confidence intervals.

Comparison of the VOF-to-DPM model to the laboratory experiment by Veron et al. 2012 (Fig. 31) also tends to confirm the model, as both spray distributions show a similar peak at ~200 micrometers. Note that our model (left) shows the count (abundance) as a function of diameter, while the results Veron et al. (2012) shows the spray concentration function as a function of diameter. While these are not identical, they both do indicate an increase in the number of spray particles.

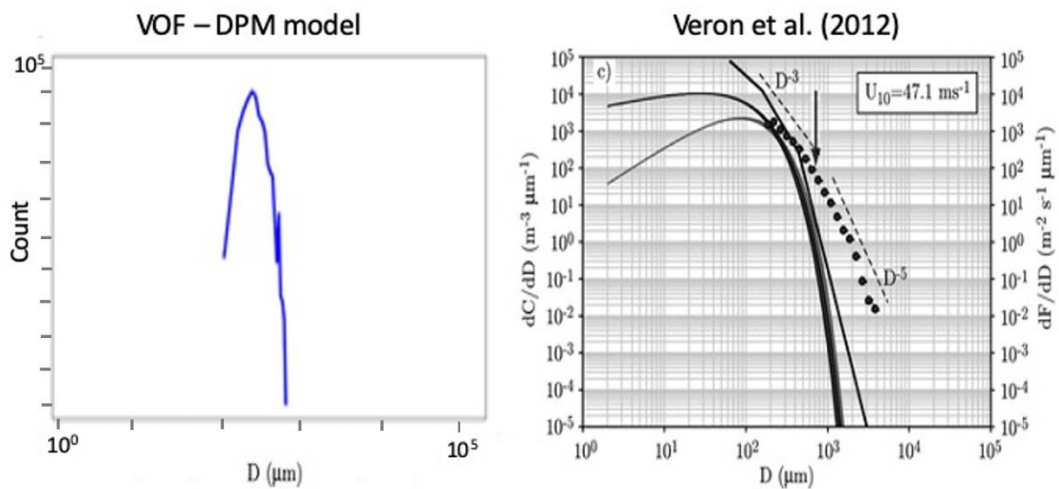


Figure 31. Comparison of the VOF-to-DPM model to a laboratory experiment conducted by Veron et al. (2012).

Further statistical model comparison was conducted through the use of QQ plots to compare probability distributions of the data. This assisted in further assessment of the model data in comparison to the experimental data. Quantiles here are values determined by dividing the probability distribution into equal intervals. Each interval has the same amount of the total data points. Based on Figure 32, the modeled data and experimental data for clean water appear to come from the same distribution below 500 μm . This makes sense, as we previously mentioned that spray radius distributions above 500 μm appear to be less reliable in our data. The deviation from the $y=x$ line may be because the distributions of both laboratory and model data are skewed (Fig. 27).

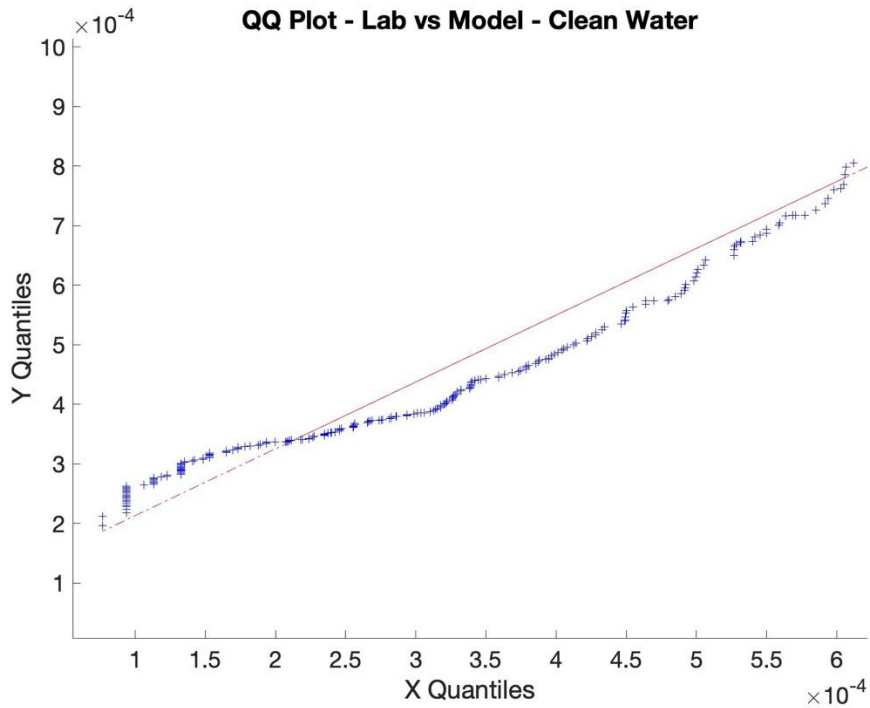


Figure 32. QQ plot for clean water conditions in the laboratory experiment and model.

Figure 33 shows a QQ plot for the surfactant conditions in the model and experimental results. The model results deviate a bit more for larger spray radii than the clean water, possibly due to the more skewed distribution than clean water as shown in Figure 27. Overall, below 500 μm , the model and experimental results appear to come from the same distribution. Above 500 μm , as previously mentioned, the data is variable and inconsistent, and is not plotted here.

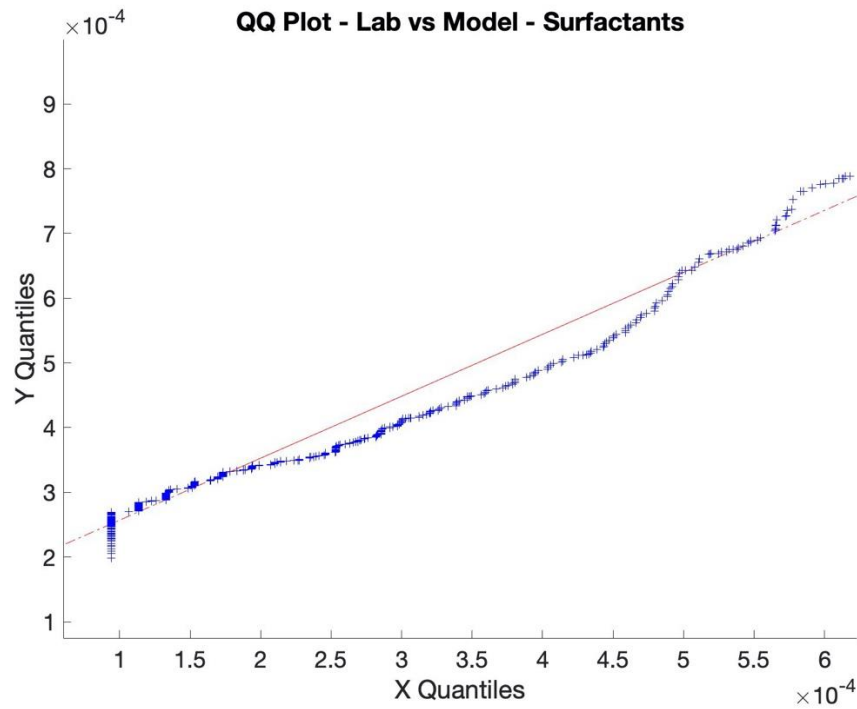


Figure 33. QQ plot for surfactant conditions in the laboratory experiment and model.

Model confirmation by observational data is crucial to modeling results, as this provides an assessment of model accuracy and errors. Using the laboratory experiment at UM and the experimental results from Veron et al. (2012), we successfully established model confirmation for the VOF-to-DPM simulation of sea spray generation under tropical cyclone conditions.

Using the confirmed VOF-to-DPM model, we calculated spray radii distributions for Category 1, 3, and 5 tropical cyclones, which would be difficult to do in a laboratory or in the field. Figures 34-36 show the individual results from each storm category conditions from the VOF-to-DPM, with confidence intervals. Overall, spray generation increased with wind speed, and in all conditions, surfactants caused a higher abundance of spray to be generated. Although data are shown for spray below 0.5 mm, this data may be affected by the spatial resolution of the model. However, spume (‘re-entrant’ spray) is likely the most significant factor in the enthalpy flux to tropical cyclones due to its short residence time, since it returns to the sea surface before it takes enough sensible heat from the atmosphere to evaporate (Peng and Richter 2019).

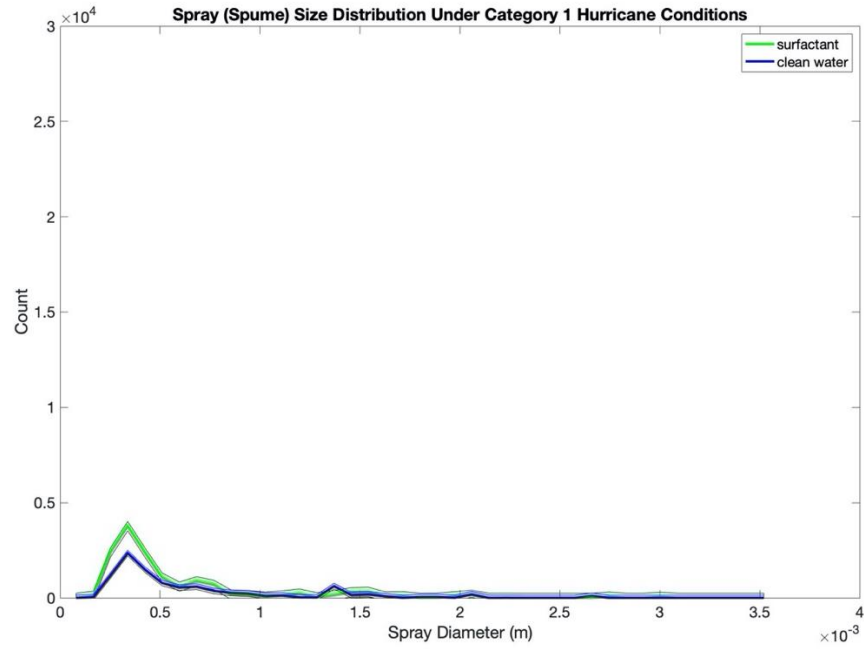


Figure 34. VOF-to-DPM spray diameter size distribution with confidence intervals under Category 1 tropical cyclone conditions, equivalent to 4 Nm^{-2} wind stress.

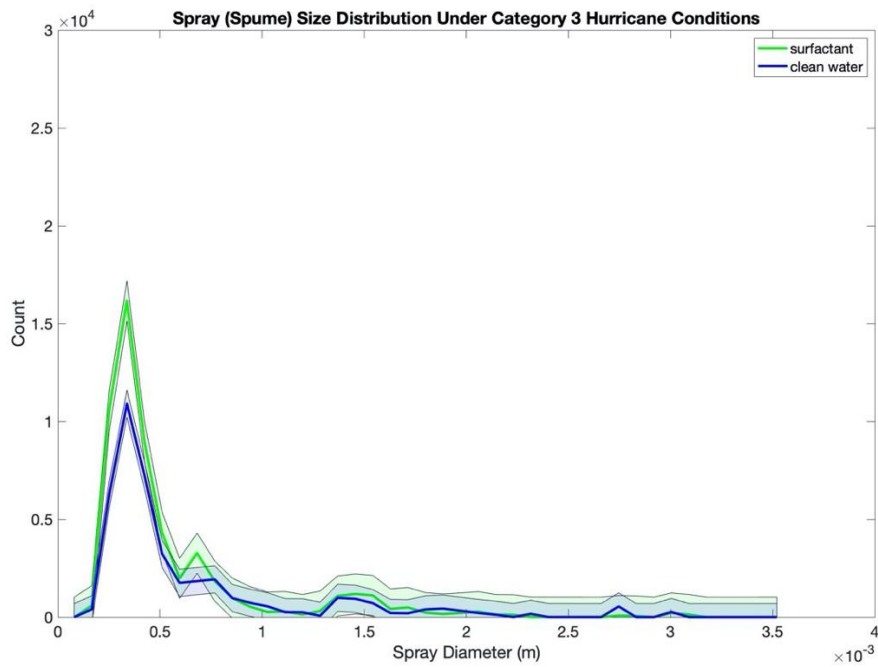


Figure 35. VOF-to-DPM spray diameter distribution with confidence intervals under Category 3 tropical cyclone conditions, equivalent to 10 Nm^{-2} wind stress.

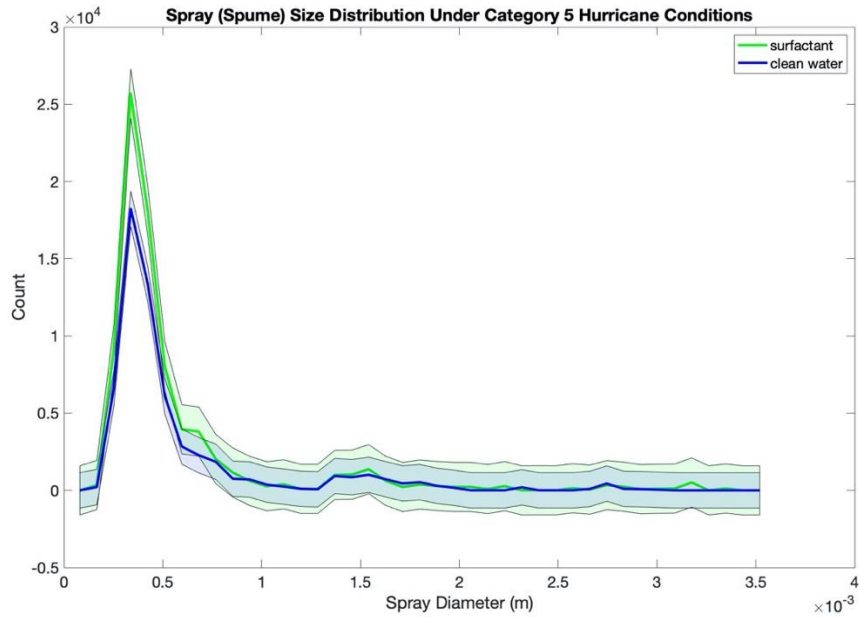


Figure 36. VOF-to-DPM spray diameter distribution with confidence intervals under Category 5 tropical cyclone conditions, equivalent to 20 Nm^{-2} wind stress.

Placing the data from the previous figures onto one plot results in Figure 37, which gives a clear visual of the positive relationship between spray abundance and wind speed from our model.

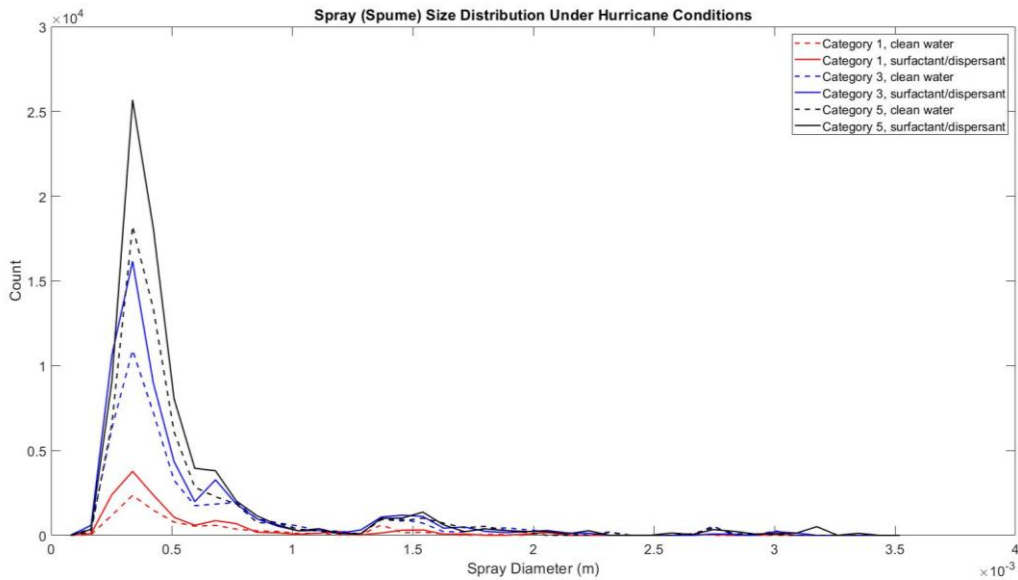


Figure 37. Spray diameter distribution from the VOF-to-DPM from all model runs.

Overall, spray generation increased with wind speed, and in all tropical cyclone categories, surfactants caused a 20-34% increase of spray concentration within the spray radii range from 100 μm to 500 μm , as shown in Figure 38.

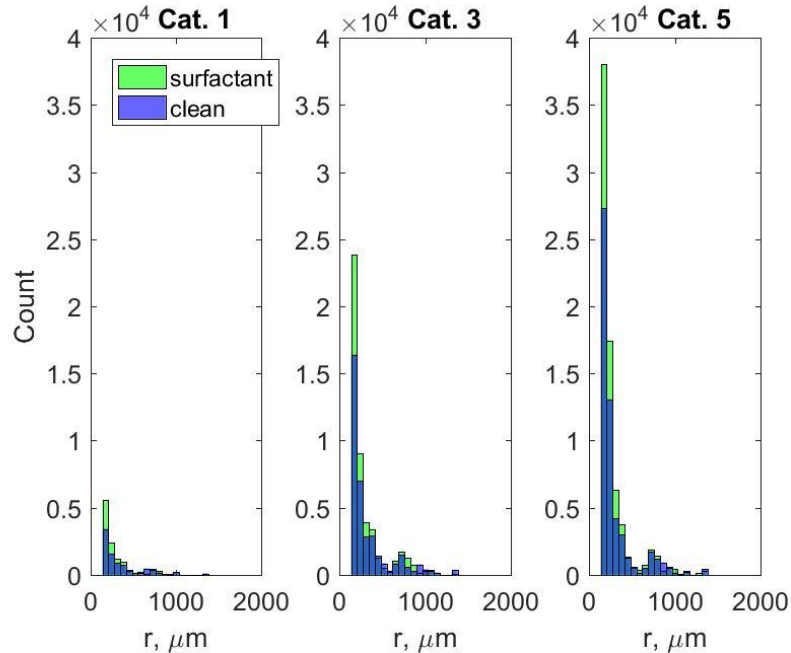


Figure 38. Spray radius distributions for Category 1 (4 Nm^{-2}), 3 (10 Nm^{-2}), and 5 (20 Nm^{-2}) tropical cyclone conditions in the VOF-to-DPM model. Scales below 100 μm are not completely resolved and have been removed from graphs.

Sea spray provides additional fuel for tropical cyclones and their intensification. Spume appears to be a significant factor in generating the enthalpy flux to tropical cyclones due to its short residence time and is less affected by the spray feedback effect, which explains spray's effect on the surrounding fluxes (Price et al. 2008, Peng & Richter 2019). Feedback occurs when outputs of a system are routed back as inputs to the system. In this case, spray's heat (turbulent, sensible, and latent) outputs are routed back to heat fluxes at the air sea interface. A positive feedback will increase the system's gain, while a negative feedback will increase the system's loss. Due to the spray feedback effect, sub-micrometer and micrometer scale sea spray particles, which have a relatively large residence time, may not significantly contribute to the air-sea flux of enthalpy into tropical cyclones.

The added momentum flux is due to the entire spectrum of spray sizes; however, the larger size droplets (spume) can produce a larger contribution to the added momentum flux

because they have a larger mass (proportional to the radius cubed). Spray takes a part of the momentum flux from wind in the near-surface layer of the marine atmosphere to accelerate, thus increasing drag (Andreas et al. 2010). ‘Re-entrant’ spray then gives this momentum to the ocean when it returns to the sea surface. This effect becomes prominent only in Category 3-5 tropical cyclones because spray stress is approximately proportional to wind speed to the fourth power (Andreas & Emanuel 2001). The drag increase due to spume can lead to a rapid decline of the major tropical cyclones above 60 m s^{-1} (Soloviev et al. 2017). The reduction of the drag coefficient in the wind speed range from approximately 30 to 60 m s^{-1} observed in laboratory and field experiments can be explained by suppression of short gravity-capillary waves by the KH type instability of the air-sea interface because the instability grows more quickly for short waves due to large shear (Koga 1981, Soloviev & Lukas 2010, Soloviev et al. 2017). Under certain environmental conditions, a combination of drag reduction from 30 to 60 m s^{-1} and drag increase above 60 m s^{-1} due to added spray stress contributes to the development of an aerodynamic drag well around a wind speed of 60 m s^{-1} (Soloviev et al. 2014).

In the presence of surfactants, the spume generation under tropical cyclone conditions is greater than in clean water (see Fig. 30). Spume droplets contribute to the heat flux between the atmosphere and ocean due to their short residence times, which affects tropical cyclone intensity. Therefore, as surfactants increase spray generation, they also increase the enthalpy flux to the atmosphere since more spume, which makes up a large part of the spray-mediated enthalpy flux, is generated (Andreas 1992, Kepert et al. 1999).

The extent of this effect might be estimated by correlating the tropical cyclone intensity changes and the presence of algal blooms identified from ocean color satellite imagery, assuming that algal blooms are favorable for the generation of bio-surfactants (see next section). The presence of bio-surfactants, as well as anthropogenic surfactants (oil spills and dispersants), can also be identified from dual-polarimetric synthetic aperture radar (SAR) imagery using the co-polarized phase difference filter (Migliaccio et al. 2009, Soloviev et al. 2011, Velotto et al. 2013), which may contribute to better understanding the anticipated effect of surfactants on tropical cyclone intensity and intensification.

d. Satellite Imagery

Satellite images provide a useful tool for collection of various oceanographic measurements, including sea surface temperature, salinity, and primary productivity. To further explore the potential relationship between primary productivity, a proxy for surfactants, and tropical cyclone intensity, I began a visual analysis of color satellite imagery. This analysis requires further quantitative work to draw any major conclusions. Chlorophyll is produced by phytoplankton, which is a major producer of bio-surfactants, and is therefore used as an indication of surfactant presence due to a lack of measurements of surfactant coverage in the world ocean (Zutic et al. 1979, Tsai & Liu 2003, King et al. 2019)

Major tropical cyclones, categorized as a Category 3 or above, from 2017-2019 are shown in the following section overlaid with chlorophyll data from either NOAA VIIRS or NASA Aqua MODIS, depending on which data provided better measurements during the date range of the storm. Satellite data were taken from the GRIIDC 8-day composite for Aqua MODIS, and GRIIDC weekly composite for NOAA VIIRS. Satellite data were taken from the beginning of the storm's formation as a tropical depression based on the Weather Underground data, to get chlorophyll data from before and during the storms passage. Most of the ocean basin has a value close to 0 mg m^{-3} with the coasts being the major exception, therefore I decided, for the purpose of this analysis, higher than normal, increased, or above average chlorophyll concentrations refer to areas that are $>0.1 \text{ mg m}^{-3}$.

The Eastern Pacific Ocean shared the highest number of major tropical cyclones in the past three years with the Indian Ocean. Tropical storm Barbara (2019), while it did not make landfall, intensified to a Category 4 storm within 24 hours. Satellite data were taken beginning on 6/28/2019. During both its time as a tropical depression (6/28-6/30), and during its time as a Category 4 storm (7/2-7/4), there were higher ($\sim 0.15 \text{ mg m}^{-3}$) than usual chlorophyll levels in the water (Fig. 39). This may have contributed to the intensification of the storm, as well as to the continuation of intensity once it reached Category 4 status, although many factors play a role in tropical cyclone intensity.

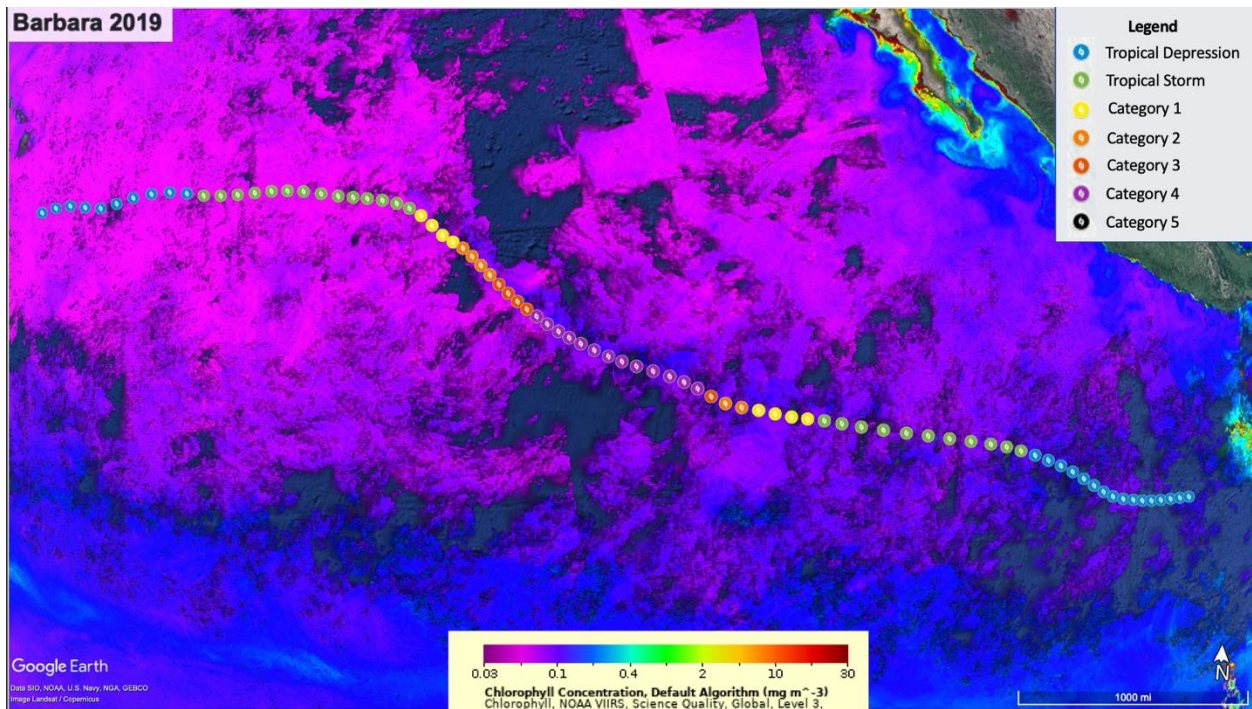


Figure 39. Tropical cyclone Barbara (2019) in the Eastern Pacific from NOAA VIIRS satellites.

Tropical cyclone Lane (2018) also did not make landfall but showed a similar pattern to Barbara (2019). Satellite data for Lane were taken beginning on 8/15/2018. Prior to intensifying to a Category 3 storm, Lane passed over an area of higher ($\sim 0.3 \text{ mg m}^{-3}$) than usual chlorophyll on 8/17/2018. Before intensifying further to a Category 5 storm on 8/18/2018, Lane passed over another patch of water with higher ($\sim 0.4 \text{ mg m}^{-3}$) than average productivity. This can be seen from the NASA Aqua MODIS images shown in Figure 40.

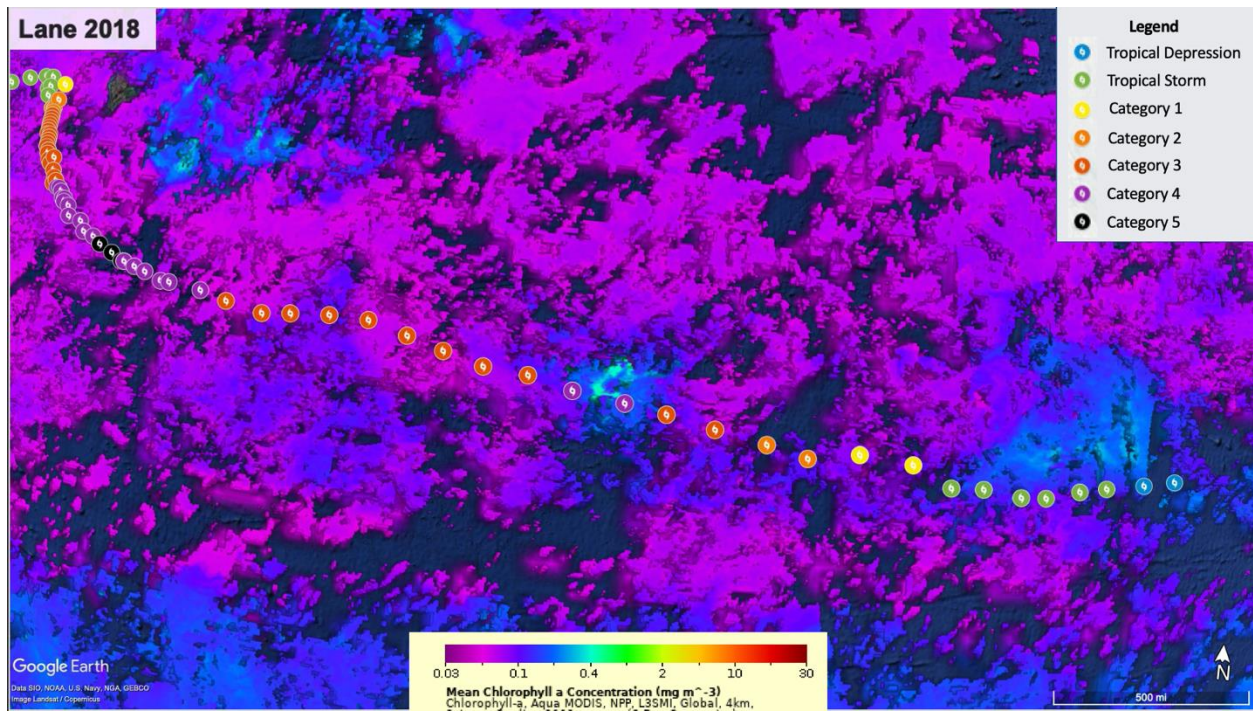


Figure 40. Aqua MODIS image of Lane (2018) showing higher than usual chlorophyll concentration in areas the storm passed prior to intensifying.

Tropical cyclone Norman (2018) also may have been influenced by surfactants. Satellite data were taken beginning on 8/28/2018. Before quickly intensifying from a Category 1 to 3 storm in only 9.5 hours on 8/30/2018, Norman passed over an area with chlorophyll concentration of ~ 0.3 to 0.35 mg m^{-3} , as shown in Figure 41.

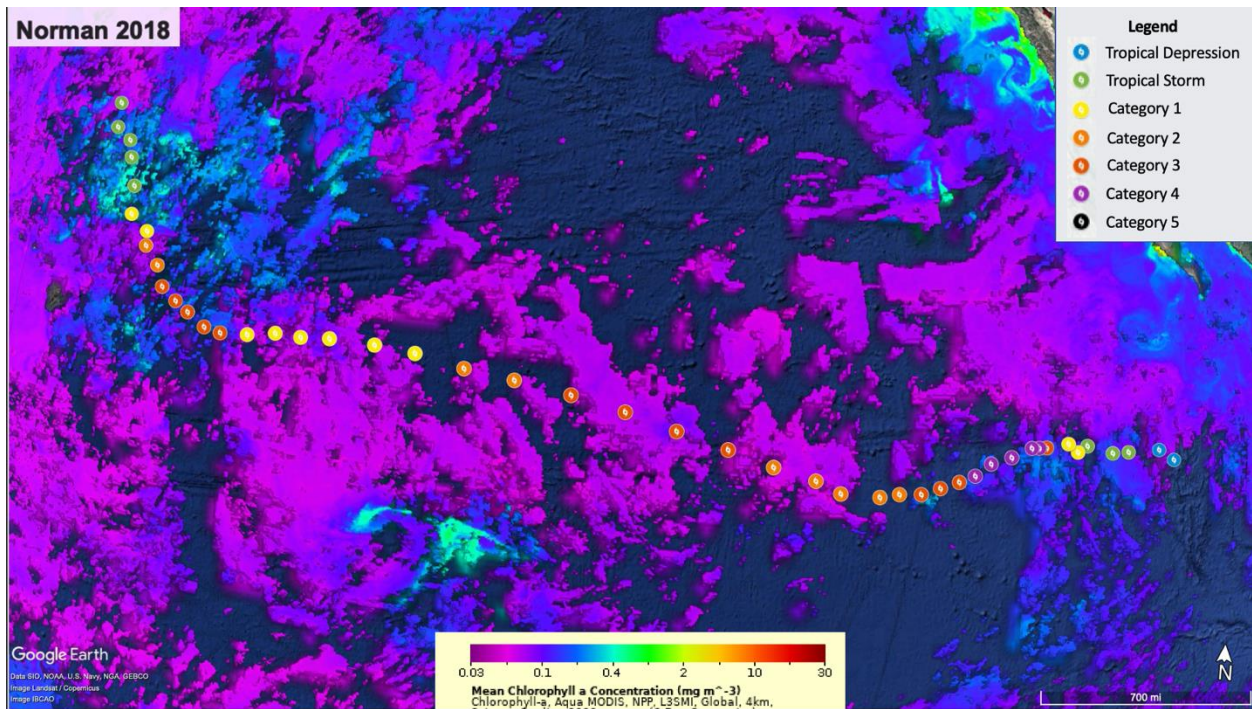


Figure 41. Tropical cyclone Norman (2018) in the Eastern Pacific from MODIS on Aqua and Terra satellites.

Tropical cyclone Olivia (2018) also intensified to a Category 4 storm on 9/4/2018 after passing through water containing higher ($\sim 0.35 \text{ mg m}^{-3}$) than average chlorophyll levels, shown in Figure 42. Satellite data were collected beginning on 9/1/2018.

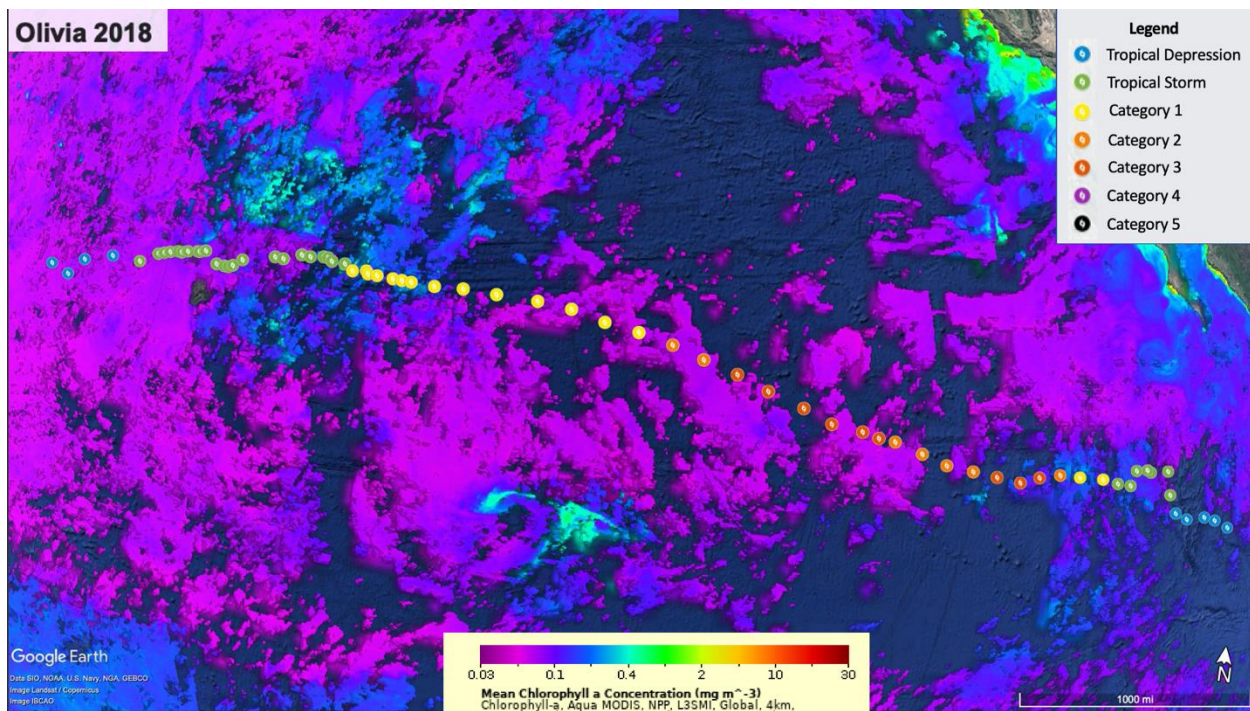


Figure 42. Tropical cyclone Olivia (2018) in the Eastern Pacific from MODIS on Aqua and Terra satellites.

Sergio (2018) also passed over water with higher than average chlorophyll levels between 9/30/2018 and 10/1/2018 before intensifying briefly to a Category 4 storm. Satellite data for Sergio was collected beginning from 9/29/2018. NASA Aqua MODIS satellite data indicates that Sergio passed over waters with chlorophyll levels of ~ 0.4 to 0.5 mg m^{-3} (Fig. 43).

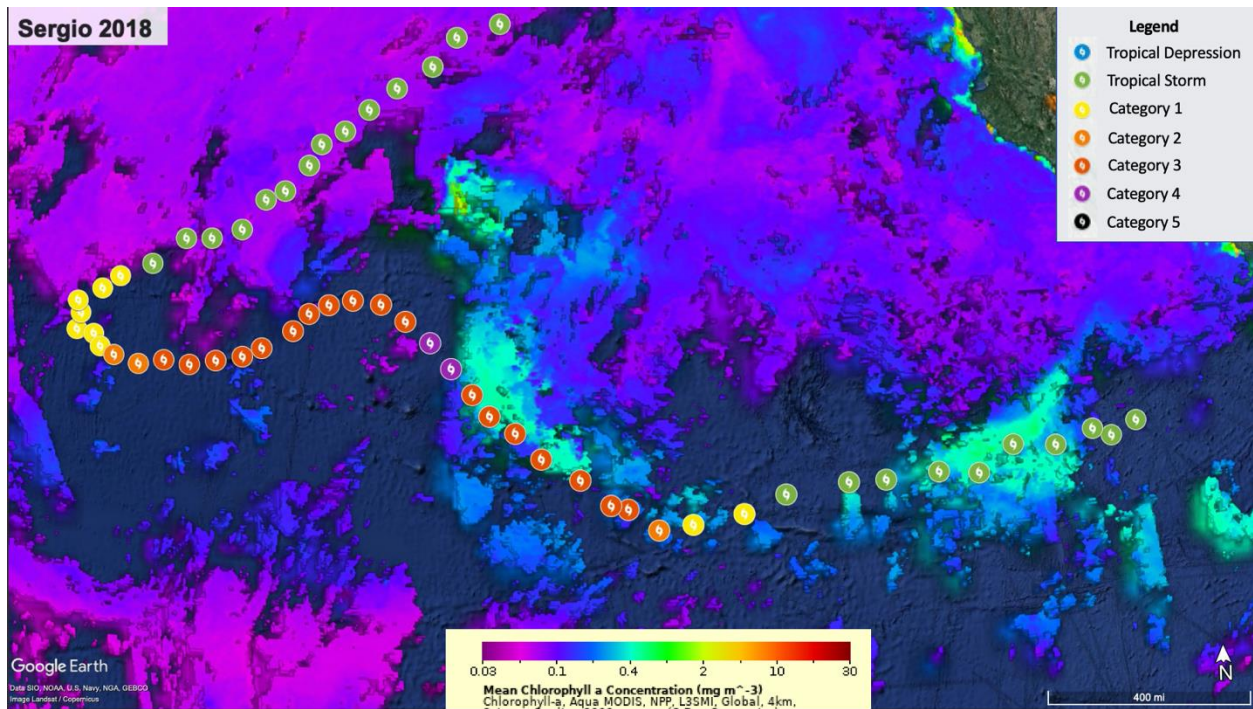


Figure 43. Aqua MODIS image of Sergio (2018) showing the higher than normal chlorophyll concentration in areas the storm passed prior to intensifying.

Eleven major storms occurred in the Indian Ocean since 2017, and only three seemed to have a potential association between increased chlorophyll levels and storm intensification. Kenneth (2019) was a short-lived storm, which passed over chlorophyll levels of $\sim 0.3 \text{ mg m}^{-3}$ on 04/23/2019 and 4/24/2019 (Fig. 44). Satellite data for this storm was collected beginning just before the storm formed, on 4/21/2019.

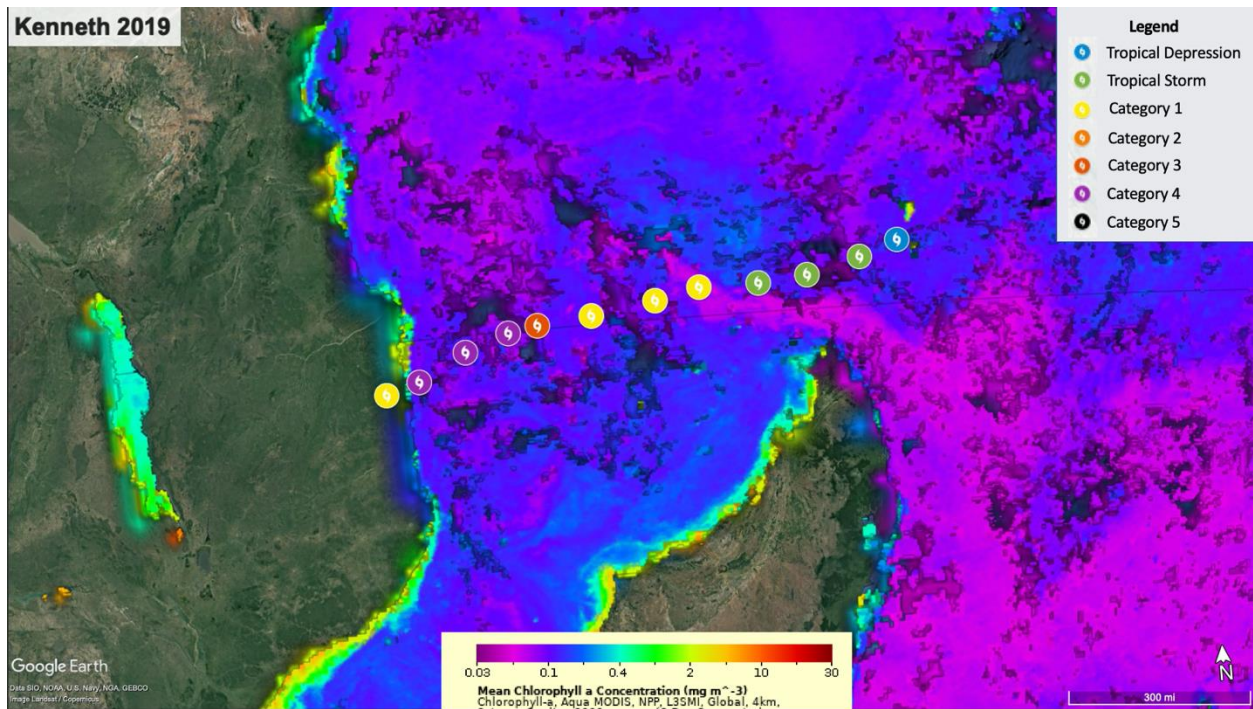


Figure 44. Tropical cyclone Kenneth (2019) in the Indian Ocean from MODIS on Aqua and Terra satellites.

Tropical cyclone Kyarr (2019), maintained Category 4 status for four days between 10/26/2019 to 10/30/2019. NASA Aqua MODIS data shows that Kyarr passed over levels of higher than normal chlorophyll during its time as a Category 4 storm from 10/26/2019 to 10/30/2019, which may have contributed to its ability to maintain intensity. Figure 45 shows that Kyarr passed over chlorophyll levels ranging from ~ 0.5 to 10 mg m^{-3} on 10/24/2019 before intensifying to a Category 4 storm within 24 hours.

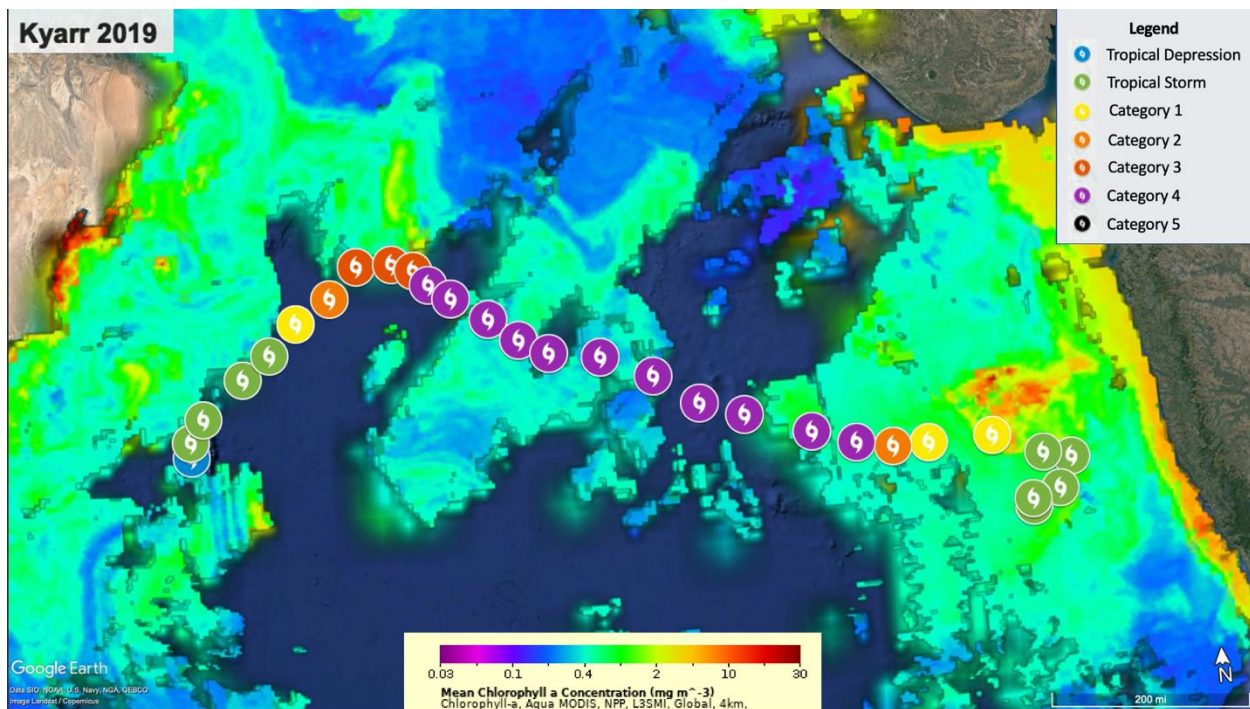


Figure 45. Tropical cyclone Kyarr (2019) in the Indian Ocean from MODIS on Aqua and Terra satellites.

Tropical cyclone Marcus (2018) only passed over land briefly as a tropical storm. Before intensifying into a Category 5 storm, it passed over multiple areas with increased chlorophyll concentration from 3/18/2018 to 3/19/2018. NASA Aqua MODIS data measured chlorophyll levels of ~ 0.4 to 2 mg m^{-3} in the areas that Marcus passed over before intensifying during 3/18/2018 to 3/19/2018, shown in Figure 46.

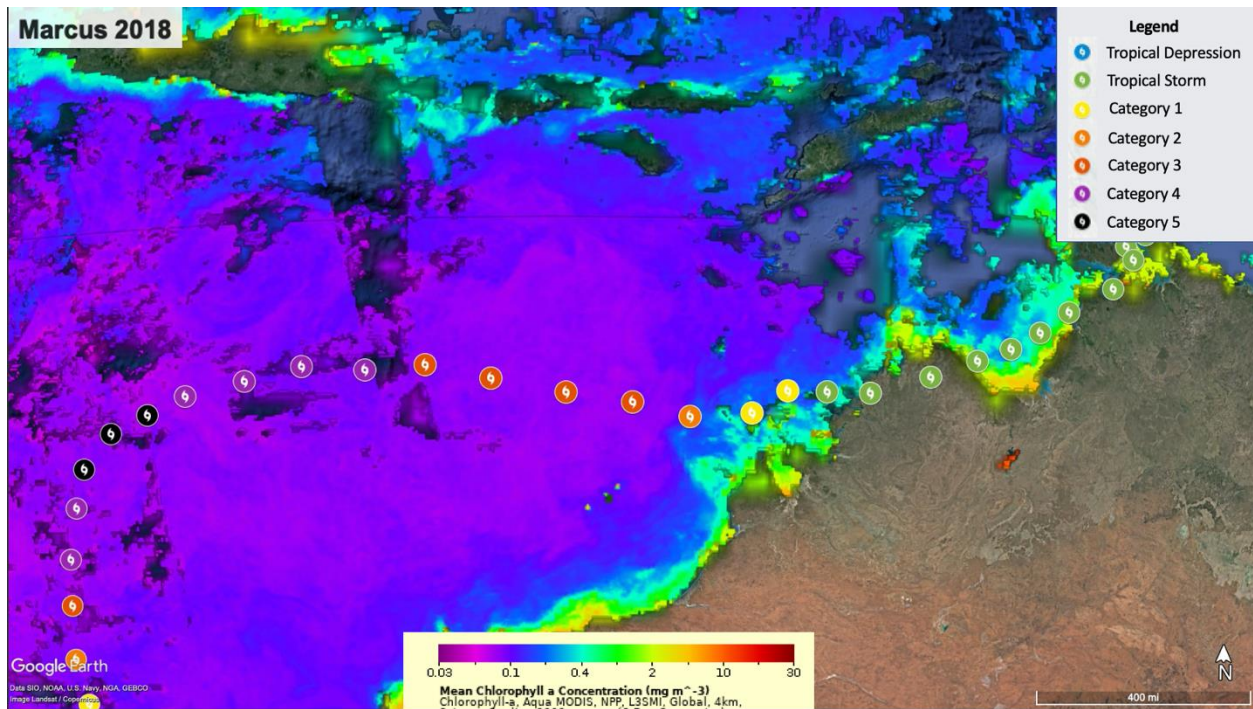


Figure 46. Aqua MODIS image of Marcus (2018) showing the above average chlorophyll concentration in areas the storm passed prior to intensifying.

While the North Atlantic Ocean only had seven major tropical cyclones since 2017, most of these storms may have had an association between passing over areas of increased chlorophyll concentration and intensifying into a major storm. Tropical cyclone Dorian (2019) lasted 11 days as a tropical cyclone, with six of those days as a major storm. Dorian is one of the strongest Atlantic hurricanes on record to hit land. NOAA VIIRS satellite data collected beginning on 8/25/2019 (Fig. 47) shows that Dorian passed over multiple areas of higher (~ 0.1 to 0.4 mg m^{-3}) than normal chlorophyll concentration around 8/27/2018 before intensifying.

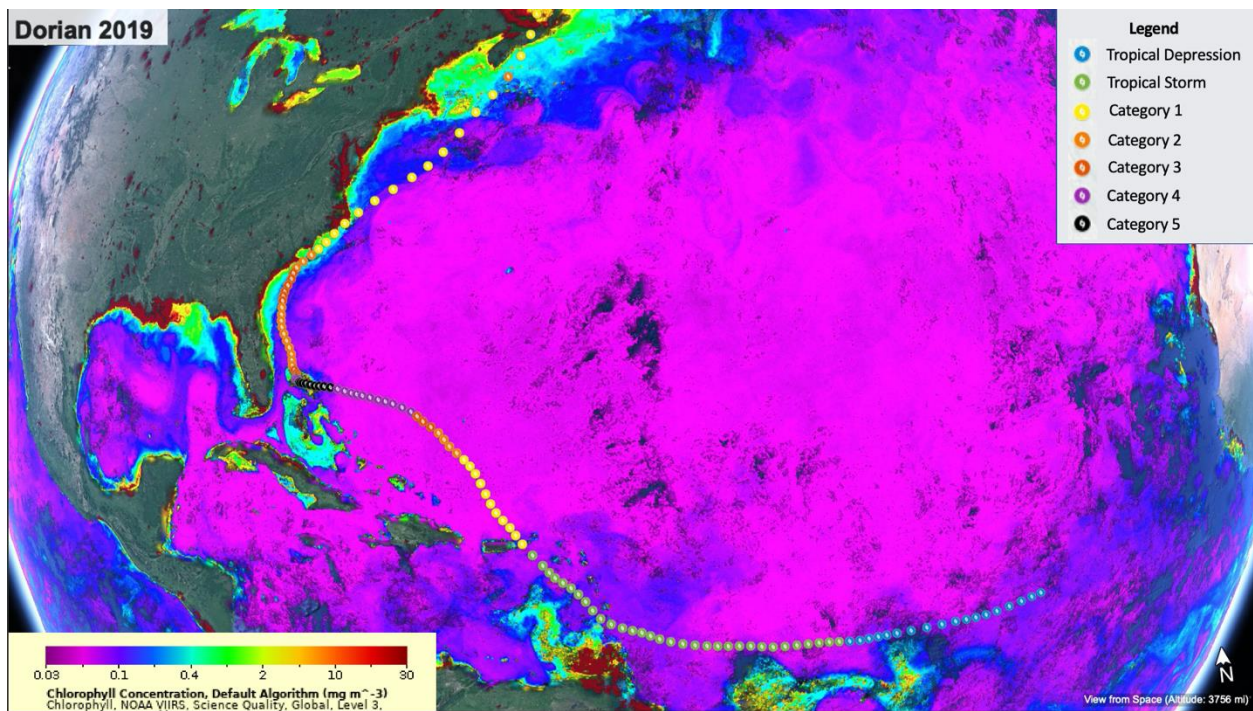


Figure 47. Tropical cyclone Dorian (2019) in the North Atlantic from NOAA VIIRS satellites.

Satellite data were taken beginning on 8/30/2019 for further analysis as the storm moved farther towards the United States. During this time, it passed over another area of high (~ 0.1 to 0.5 mg m^{-3}) chlorophyll concentration near the Bahamas (Fig. 48) between 9/2/2019 and 9/3/2019. This may have contributed to its ability to remain a major storm after landfall.

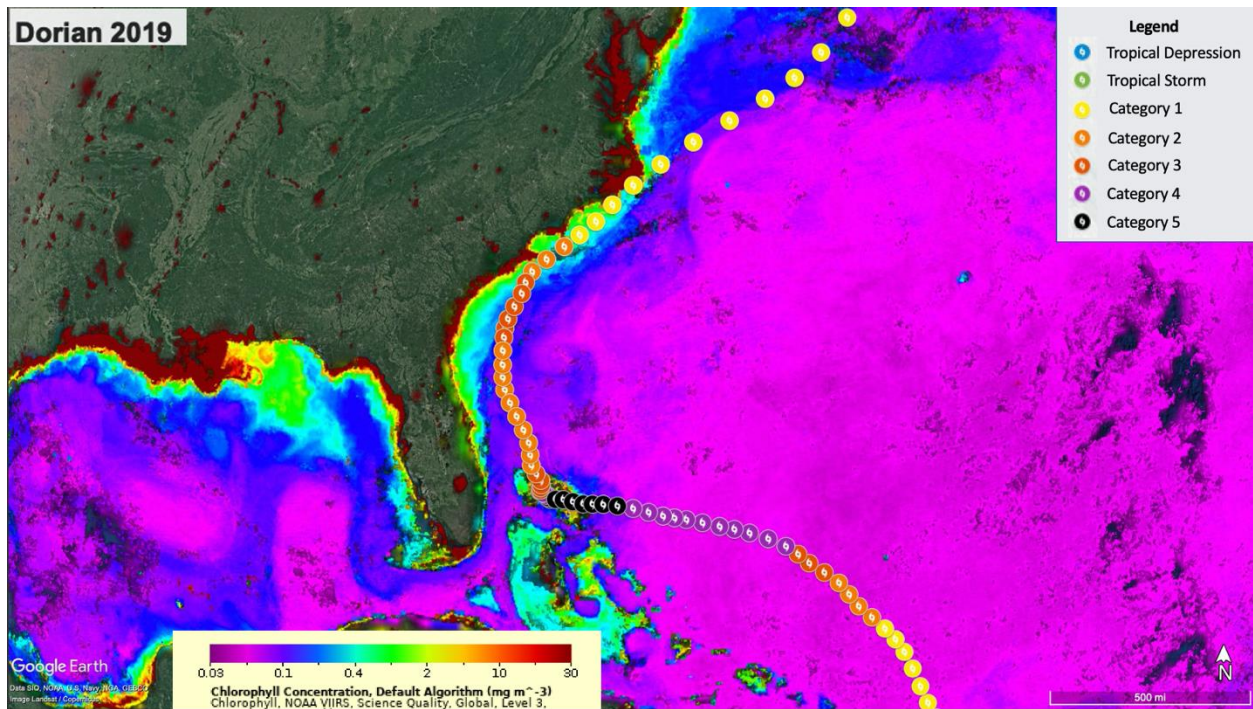


Figure 48. NOAA VIIRS image of Dorian (2019) showing the higher than usual chlorophyll concentration in areas the storm passed which may have assisted it in maintaining intensity despite traveling over land.

Tropical cyclone Florence (2018) remained a tropical storm for eight days from 9/4/2018 to 9/6/2018 and from 9/9/2018 to 9/14/2018, intensifying twice to a Category 4 storm. Figure 49 shows Florence passing over an area of above average (~ 0.1 to 0.5 mg m^{-3}) chlorophyll on 8/31/2018 before intensifying. Satellite data were taken beginning from 8/30/2018. Satellite data for the later portion of the storm were taken from 9/5/2018 but not used in this analysis as it did not contribute meaningful data.

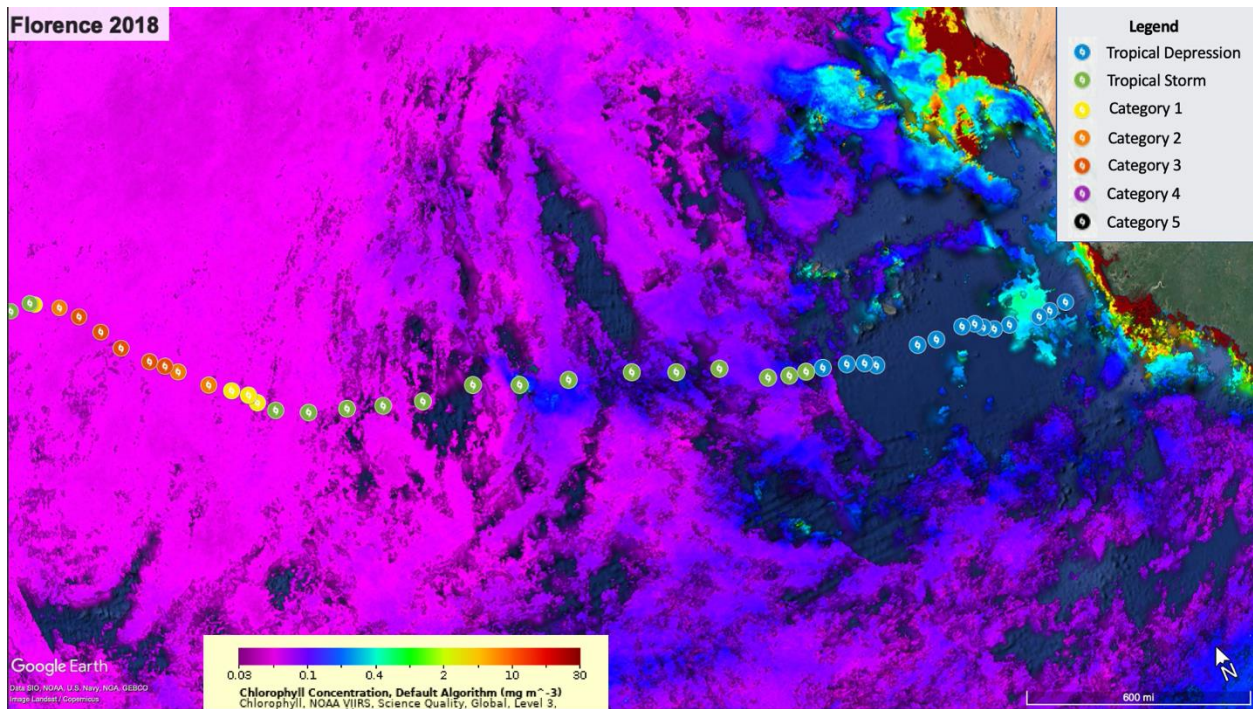


Figure 49. NOAA VIIRS image of Florence (2018) showing the above average chlorophyll concentration in areas the storm passed prior to intensifying.

Tropical cyclone Irma (2017) had devastating effects on many Caribbean islands and the Florida Keys. Before Dorian (2019), Irma was the most powerful hurricane in the Atlantic. Irma maintained tropical cyclone status for twelve days from 8/31/2017 to 9/11/2017, and all but one of those days the storm remained a major tropical cyclone (9/2/2017). Irma was able to maintain intensity as a Category 5 storm for three days between 9/5/2017 and 9/8/2017, with a brief intensification to a Category 5 again a few days later (9/9/2017). Irma first intensified to a Category 2 storm after passing an area of $\sim 0.15 \text{ mg m}^{-3}$ chlorophyll concentration around 8/30/2017. Once Irma reached Category 5 intensity, it passed once again over an area of chlorophyll concentration of ~ 0.1 to 2 mg m^{-3} (Fig. 50) on 9/6/2017. This may have aided its ability to maintain Category 5 status for so long. Before its second intensification to Category 5, Irma passed over another area of increased (~ 0.4 to 2 mg m^{-3}) chlorophyll concentration on 9/8/2017, as also seen in Figure 50.

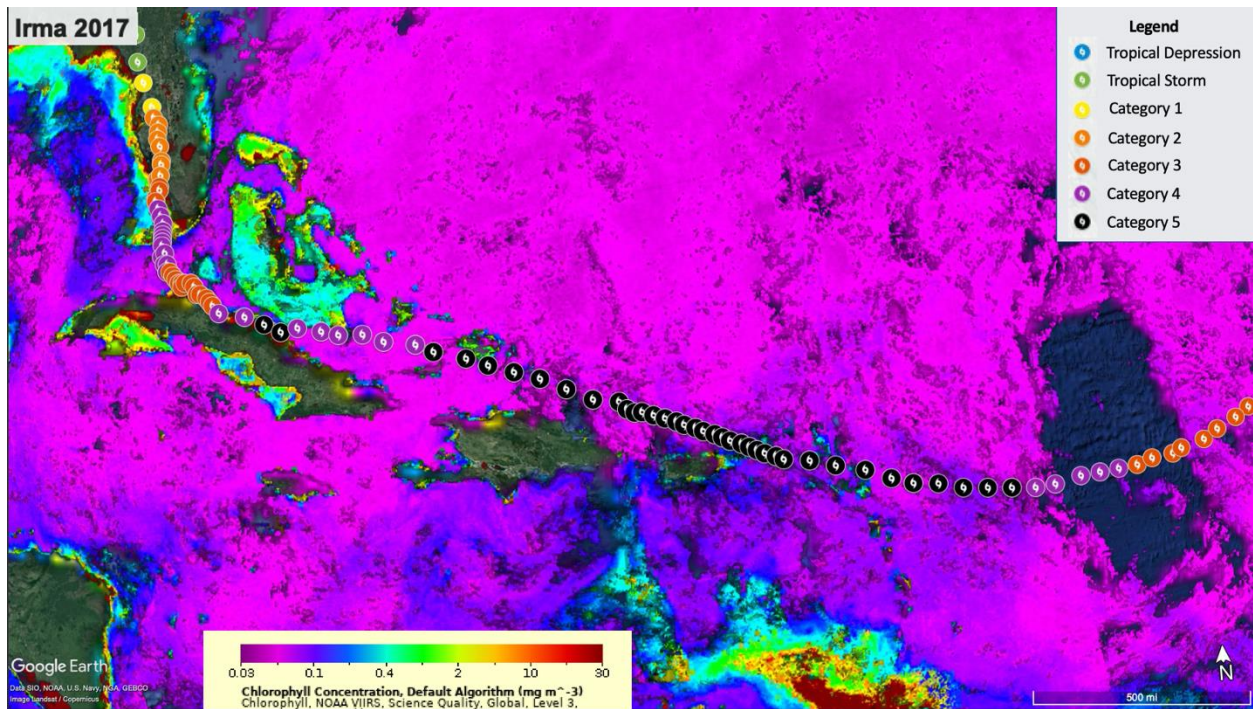


Figure 50. NOAA VIRRS image of Irma (2017) showing the higher than usual chlorophyll concentration in areas the storm passed while maintaining intensity and later regaining intensity before hitting Florida.

Lorenzo (2019), shown in Figure 51, also passed over an area of higher (~ 0.1 to 0.4 mg m^{-3}) than usual chlorophyll concentration in the Eastern Atlantic on 9/23/2019, before intensifying to a major storm and maintaining intensity for four days from 9/26/2019 to 9/29/2019. Satellite data were taken beginning from 9/22/2019.

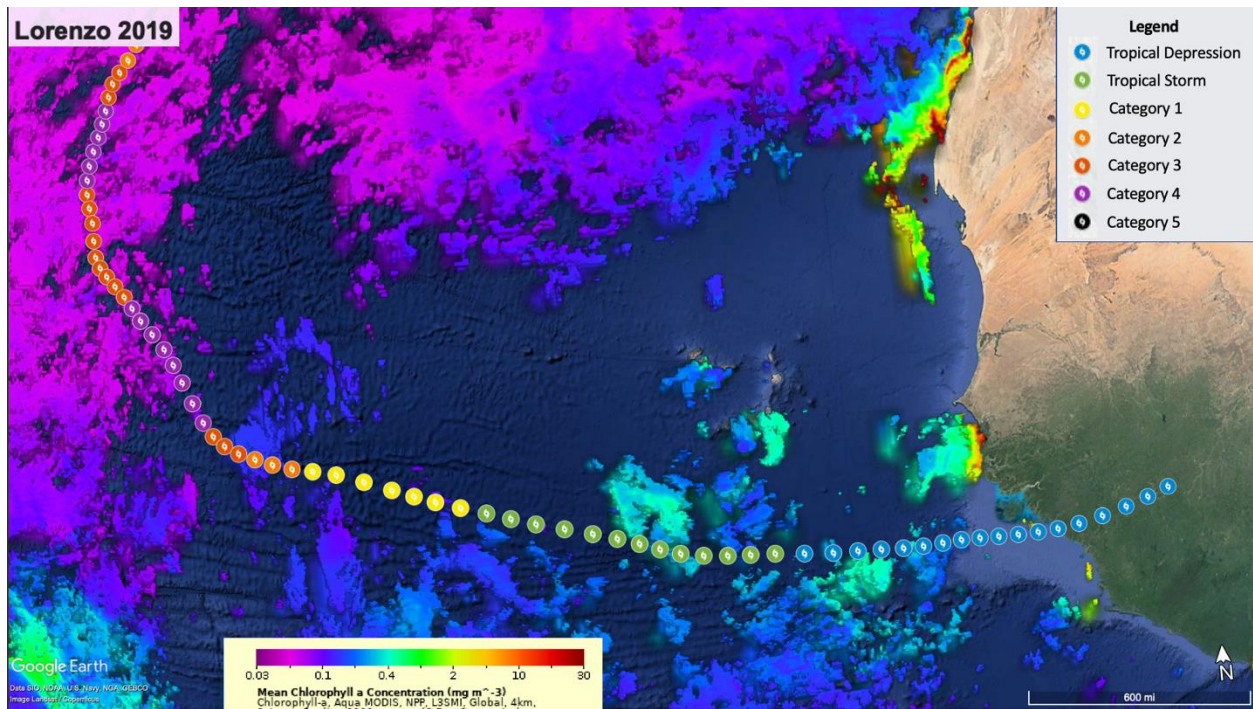


Figure 51. Aqua MODIS image of tropical cyclone Lorenzo (2019) in the North Atlantic showing the higher than usual chlorophyll concentration in areas the storm passed before intensifying.

Tropical cyclone Michael (2018) was a powerful storm that made landfall in the Florida panhandle in October 2018. Michael began picking up intensity before passing any high concentrations of chlorophyll but intensified quickly from a Category 1 storm to a Category 4 storm within 24 hours after passing an area of high ($\sim 1 \text{ mg m}^{-3}$) chlorophyll levels near Cuba on 10/8/2018. Satellite data were collected beginning on 10/7/2018. Shown in Figure 52 is the area near the coast where Michael passed over on 10/10/2018 before intensifying into a Category 5 storm. This area had a chlorophyll concentration of ~ 10 to 20 mg m^{-3} , which is much higher than most areas of the open ocean.

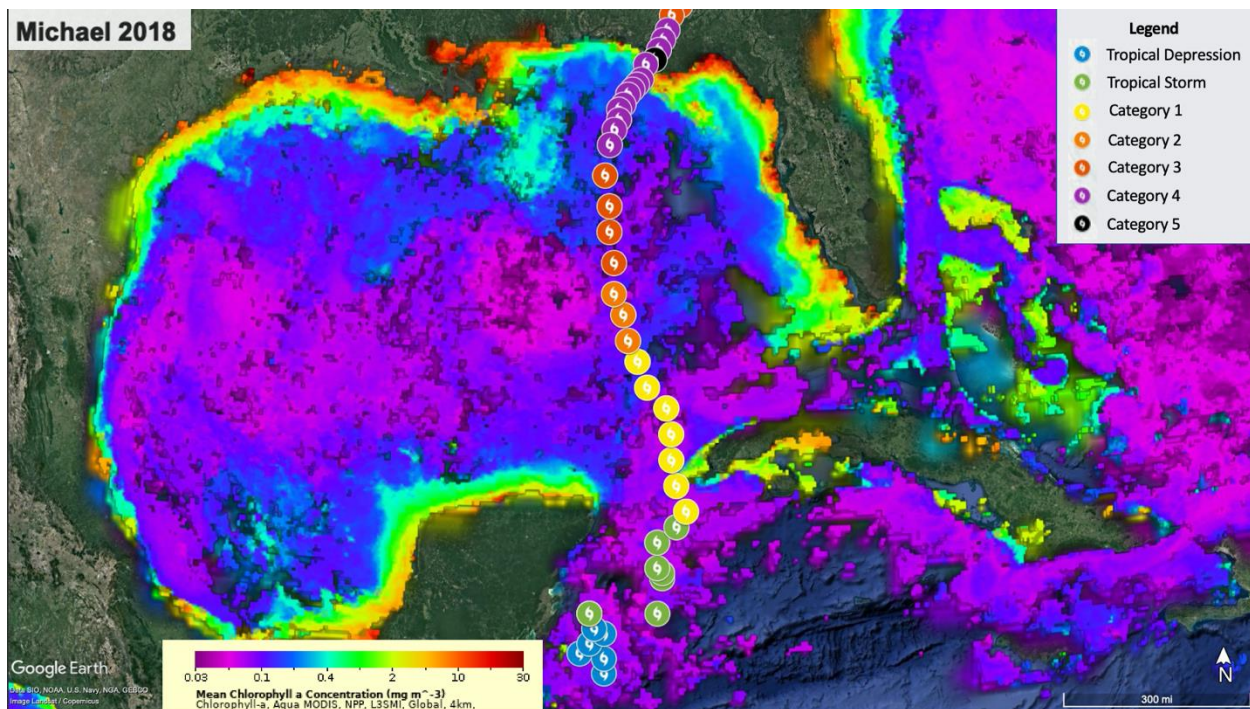


Figure 52. Aqua MODIS image of tropical cyclone Michael (2018) in the North Atlantic showing the increased chlorophyll concentration in areas the storm passed before intensifying into a Category 5 storm.

Tropical cyclone Maria (2017) was an extremely dangerous and deadly storm that devastated Dominica, St. Croix, and Puerto Rico after rapidly intensifying within 24 hours to a Category 5 storm on 9/18/2017. Before intensifying Maria passed over an area of higher ($\sim 0.15 \text{ mg m}^{-3}$) than usual chlorophyll concentration on 9/17/2017. Satellite data were taken beginning on 9/16/2017. Figure 53 shows a zoomed in image of Maria's path, traveling over many areas of increased chlorophyll levels as it made its way across the Caribbean. Before intensifying to a Category 5 storm, Maria passed over an area of $\sim 0.15 \text{ mg m}^{-3}$, and then it weakened as it made landfall in Dominica. It was able to regain strength after landfall, which could have been aided by the patch of water with increased chlorophyll levels it passed once again on 9/19/2017. Maria weakened to a Category 2 on 9/20/2017, but then regained strength to a Category 3 again, after passing an area with chlorophyll levels of $\sim 1 \text{ mg m}^{-3}$ on 9/21/2017.

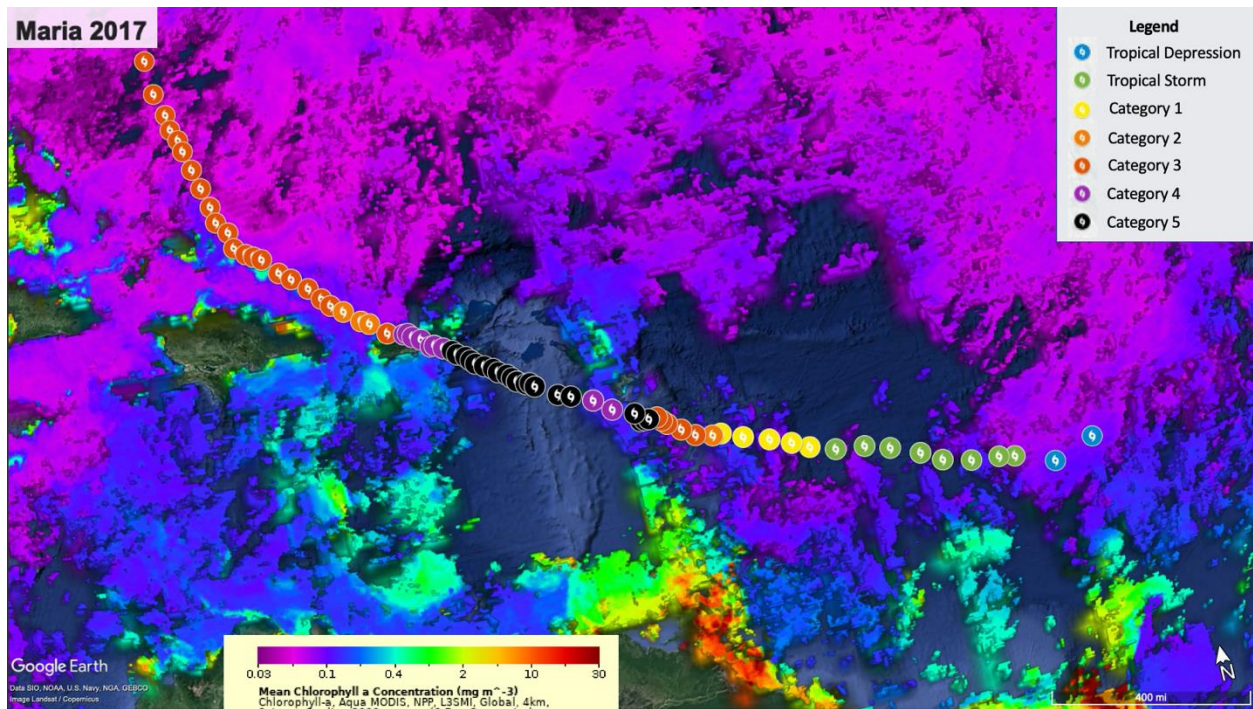


Figure 53. Aqua MODIS image of tropical cyclone Maria (2017) in the North Atlantic showing areas of higher than usual chlorophyll concentration the storm passed over before intensifying.

Only one storm out of ten in the Western Pacific showed any potential association between increased primary productivity and intensification. Tropical cyclone Wutip (2019) passed a large area of enhanced chlorophyll concentration of ~ 0.1 to 0.3 mg m^{-3} between 2/20/2019 and 2/22/2019 before intensifying into a Category 5 storm, as shown in Figure 54. Satellite data were taken beginning from 2/19/2019.

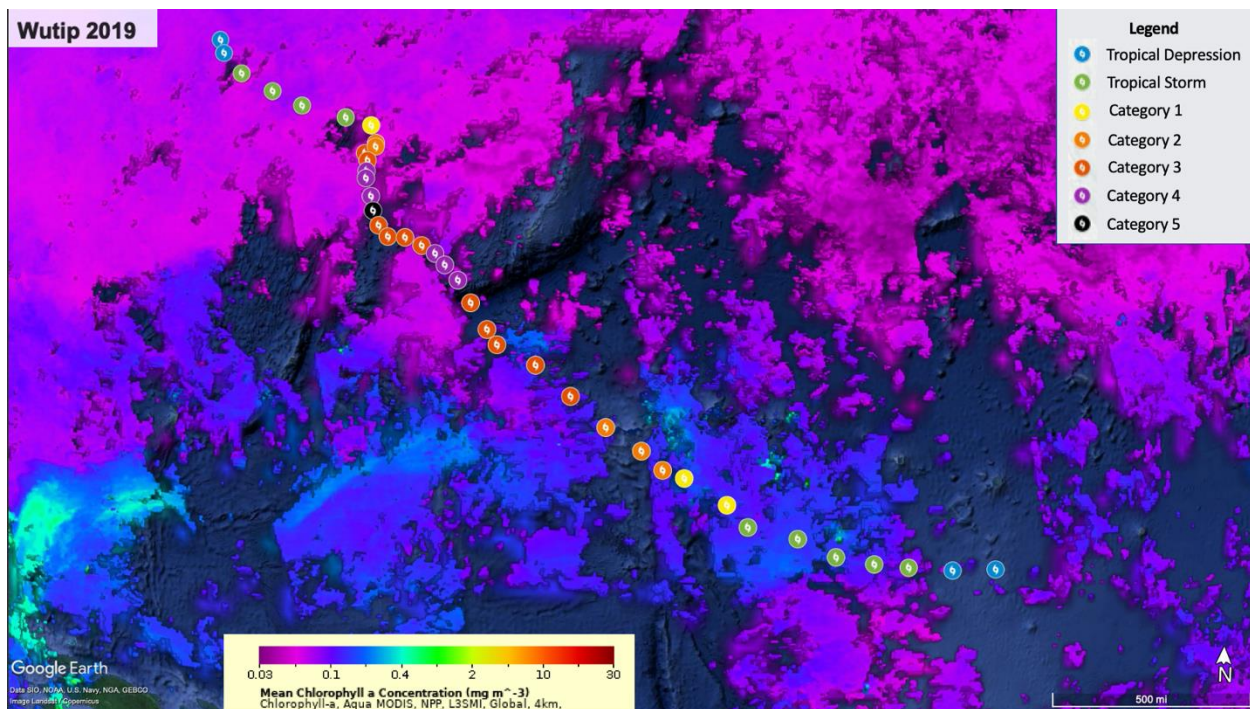


Figure 54. Tropical cyclone Wutip (2019) in the Western Pacific from MODIS on Aqua and Terra satellites.

Comparing tropical cyclone tracks to chlorophyll data from NASA Aqua MODIS and NOAA VIIRS revealed potential association between major tropical cyclones and high primary productivity levels, which are indicative of surfactant production. The difference in association between storm intensity and primary production between ocean basins could be due to the fact that different ocean basins have different primary productivity levels. The North Atlantic, which showed a high number of storms with a potential association has highly productive summers due to the deep winter mixed layer, which releases phytoplankton in the spring (Sigman 2012). Eastern parts of ocean basins are also highly productive due to coastal upwelling, which would help explain the high number of storms with potential associations found in the Eastern Pacific and many storms in the Eastern Atlantic. Meanwhile, Western areas of ocean basins are less productive, giving further evidence as to why the possible association in the Western Pacific may be so low. As for the low correspondence in the Indian Ocean, Roxy et al. 2016 found that there has been a decrease of up to 20% in primary productivity in the last 60 years caused by an increase in surface temperature that inhibits nutrient mixing, which could explain the low association found there.

This initial color satellite imagery analysis focused mainly on qualitative comparison but showed that there is potential for color satellite oceanography. A quantitative analysis moving forward would enhance this work dramatically. Future work includes calculating intensity changes based on the midpoint of the data, then comparing these locations to the history of the chlorophyll concentration along the track. This would allow quantitative calculations to correlate tropical cyclone strength changes and primary productivity levels. More research and analysis is needed here because many factors influence tropical cyclone intensity.

While various satellite imagery is often used to collect data on tropical cyclones, conventional satellites are limited by cloud cover. C-band SAR is an exception to this, as it is able to penetrate cloud cover while maintaining high resolution (Friedman & Li 2000; Katsaros et al. 2002). Zhang and Perrie (2012) specifically used a C-band Cross-Polarization Ocean (C-2PO) model to observe tropical cyclones from space. The presence of bio-surfactants, as well as anthropogenic surfactants (oil spills and dispersants), can also be identified from dual-polarimetric SAR imagery using the co-polarized phase difference filter (Wahl et al., 1996, Lu et al., 1999, 2000, Gade and Alpers, 1999, Migliaccio et al 2009, Soloviev et al. 2011, Velotto et al. 2013), which may contribute to better understanding the potential effect of surfactants on tropical cyclone intensity and intensification. The Taylor Energy Platform off the Louisiana Coast was damaged in 2004 by Hurricane Ivan, leading to the longest (15 year) oil spill in U.S. history. The spill can be seen in Figure 55 as a dark triangular area.

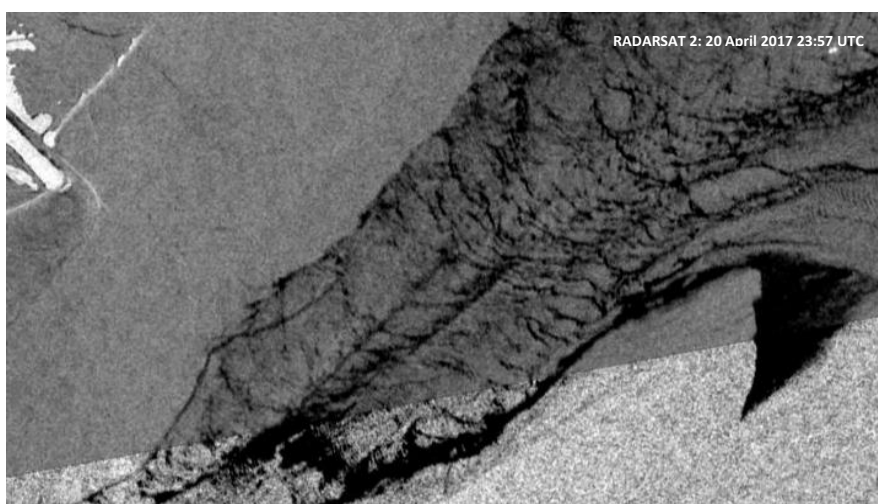


Figure 55. SAR satellite image of the Taylor Energy Platform off the Louisiana Coast.

Oil spills and areas where dispersants are applied affect sea surface tension. Based on the results from this work, this change of sea surface tension may result in a difference in sea spray generation and therefore an effect on tropical cyclone intensity. SAR imagery may be a useful tool not only to collect data on tropical cyclones, but also in predicting them in areas covered by oil spills, dispersants, or surfactant slicks, specifically in the Gulf of Mexico, where the Taylor Energy Platform oil leak and Deep Water Horizon oil spill have occurred in the last 15 years.

6. Conclusions

This work has demonstrated, for the first time, the increase of the sea spray generation and change in size distribution under tropical cyclone conditions in the presence of surfactants using a CFD model confirmed with laboratory experiments that resolved spray size distributions starting from a 100- μm radius. As surfactants increase spray generation and change the size distribution, they influence heat and momentum fluxes to the atmosphere, potentially affecting tropical cyclone intensity.

A complete investigation of the effect of bio-surfactants on the tropical cyclone intensity and intensification is not feasible at this point due to the complexity of the problem and scarcity of the field data and is beyond the scope of this thesis. The extent of the surfactant effect on tropical cyclones might be qualitatively estimated by correlating the tropical cyclone intensity changes and the presence of chlorophyll identified from color satellite imagery, assuming that primary productivity is favorable for the generation of bio-surfactants. The presence of bio-surfactants, as well as anthropogenic surfactants (oil spills and dispersants), can also be identified from dual-polarimetric synthetic aperture radar (SAR) imagery using the co-polarized phase difference filter, which may contribute to better understanding the potential effect of surfactants on tropical cyclone intensity and intensification.

Including evaporation and heat fluxes in our CFD modeling would greatly increase the understanding of these relationships, which are difficult to observe and measure in the field and laboratory. This work is currently in progress, since part of this work was to assess the feasibility of implementing evaporation and heat fluxes into the VOF-to-DPM model, which requires more time. Using the model to study the vertical distribution of spray would also provide a better understanding of spray's effects on heat and momentum fluxes. Expanding the domain used in

this work will also allow for more accurate results, as the small domain does not allow waves to mature, and waves influence both drag and spray at the air-sea interface. In the ocean under tropical cyclone conditions, surfactants on the sea surface affect heat, energy, and momentum exchange through altered size distributions of sea spray, with possible consequences for tropical cyclone intensification or decline, particularly in biologically productive areas and the areas affected by oil spills and dispersants. Improving the air-sea flux implementation in forecast models for enhanced tropical cyclone intensity forecasting is essential to prevent the loss of lives.

7. References

- Abtew, W. (2019). Hurricanes: Wind, rain, and storm surge. In *Extreme Hydrology and Climate Variability* (pp. 367-378). Elsevier.
- Alpers, W., & Espedal, H. A. (2004). "Oils and Surfactants" in *Synthetic Aperture Radar Marine User's Manual*, NOAA, 263–276.
- Andreas, E.L., 1992: Sea spray and the turbulent air-sea heat fluxes. *J. Geophys. Res.*, 97, 11, 429-11, 441.
- Andreas, E. L., & Emanuel, K. A. 2001. Effects of sea spray on tropical cyclone intensity. *J. Atmos. Sci.*, 58(24), 3741-3751.
- Andreas, E., Vlahos, P., & Monahan, E. (2017). Spray-Mediated Air-Sea Gas Exchange: The Governing Time Scales. *J. Mar. Sci.*, 5, 60.
- Alpers, W., & Hühnerfuss, H. (1988). Radar Signatures of Oil Films Floating on the Sea Surface and the Marangoni Effect. *J. Geophys. Res. Oceans*, 93 (C4): 3642–3648.
- ANSYS Fluent Theory Guide 19.2*. (2018). ANSYS, Inc.
https://ansyshelp.ansys.com/account/secured?returnurl=/Views/Secured/corp/v192/flu_th/flu_th.html/.
- Bai, Y. (2019). "Visible Infrared Imaging Radiometer Suite (VIIRS)." *National Oceanic and Atmospheric Administration*. <https://ncc.nesdis.noaa.gov/VIIRS/>.
- Bao, J.W., Wilczak, J. M., Choi, J.K., & Kantha, L. H. (2000). Numerical simulations of air–sea interaction under high wind conditions using a coupled model: A study of hurricane development. *Mon. Weather. Rev.*, 128, 2190–2210.

- Bao, J.W., Fairall, C. W., & Michelson, S. A. (2017). The Final Report of the Project Entitled “Evaluation and Improvement of Spray-Modified Air-Sea Enthalpy and Momentum Flux Parameterizations for Operational Hurricane Prediction”.
- Banner, M. L., & Phillips, O. M. (1974). On the incipient breaking of small-scale waves. *J. Fluid Mech.*, 65, 647– 656.
- Barnes, G. M. (2006). Thermodynamic structure of a hurricane’s lower cloud and subcloud layers. Preprints, 27th Conf. on Hurricanes and Tropical Meteorology, Monterey, CA, *Amer. Meteor. Soc.*, 5C.1.
- Bell, M. M., Montgomery, M. T., & Emanuel, K. A. (2012). Air-sea enthalpy and momentum exchange at major hurricane wind speeds observed during CBLAST. *J. Atmos. Sci.*, 69(11), 3197-3222.
- Bhatia, K. T., Vecchi, G. A., Knutson, T. R., Murakami, H., Kossin, J., Dixon, K. W., & Whitlock, C. E. (2019). Recent increases in tropical cyclone intensification rates. *Nat. Commun.*, 10(1), 1-9.
- Bianco, L., Bao, J.W., Fairall, C. W., & Michelson, S. A. (2011). Impact of sea spray on the surface boundary layer, *Bound-Lay. Meteorol.*, 140.
- Blanchard, D. C. (1963). The electrification of the atmosphere by particles from bubbles in the sea. *Prog. Oceanogr.*, 1, 73-202.
- Brackbill, J. U., Kothe, D. B., & Zemach, C. (1992). A continuum method for modeling surface tension. *J. Comput. Phys.*, 100(2), 335-354.
- Brockmann, U. H., Huhnerfuss, H., Kattner, G., Broecker, H. C., & Hentzschel, G. Artificial surface films in the sea area near Sylt 1. *Limnol. Oceanogr.*, 27(6), 1050-1058 (1982).
- Cangialosi, J. P. “National Hurricane Center Forecast Verification.” *National Hurricane Center Forecast Verification*, NOAA, 4 Apr. 2017, www.nhc.noaa.gov/verification/.
- Chen, H., Zhang, D. L., Carton, J., & Atlas, R. (2011). On the rapid intensification of Hurricane Wilma (2005). Part I: Model prediction and structural changes. *Weather Forecas.*, 26(6), 885-901.
- Davis, C., Wang, W., Cavallo, S., Done, J., Dudhia, J., Fredrick, S., & Torn, R. (2011). High-resolution hurricane forecasts. *Comput. Sci. Eng.*, 13(1), 22-30.
- DeMaria, M., Sampson, C. R., Knaff, J. A., & Musgrave, K. D. (2014). Is tropical cyclone intensity guidance improving? *Bull. Amer. Meteor. Soc.*, 95, 387–398.

- Donelan, M. A., Haus, B. K., Reul, N., Plant, W. J., Stiassnie, M., Graber, H. C., Brown, O. B., & Saltzman, E. S. (2004). On the limiting aerodynamic roughness of the ocean in very strong winds. *Geophys. Res. Lett.*, 31, L18306.
- Dong, C.M., & Huang, C.J. (2004). Generation and propagation of water waves in a two-dimensional numerical viscous wave flume. *J. Waterw., Port. C-ASCE*, 130(3), 143-153.
- Drennan, W. M., Zhang, J. A., French, J. R., McCormick, C., & Black, P. G. Turbulent fluxes in the hurricane boundary layer. Part II: Latent heat flux. *J. Atmos. Sci.*, 64(4), 1103-1115 (2007).
- Edson, J.B., & Fairall, C.W. Spray droplet modeling. I: Lagrangian model simulation of the turbulent transport of evaporating droplets. *J. Geophys. Res.*, 99, 25295-25311 (1994).
- Eggers, J. (1997). Nonlinear dynamics and breakup of free-surface flows. *Rev. Mod. Phys.*, 69(3), 865.
- Emanuel, K. A. (1997). Some aspects of hurricane inner-core dynamics and energetics. *J. Atmos. Sci.*, 54(8), 1014-1026.
- Emanuel, K. A., (1986). An air-sea interaction theory for tropical cyclones. Part I. *J. Atmos. Sci.*, 42, 1062-1071.
- Emanuel, K. A., (1995). Sensitivity of tropical cyclones to surface exchange coefficients and a revised steady-state model incorporating eye dynamics. *J. Atmos. Sci.*, 52, 3969-3976.
- Emanuel, K., & Zhang, F. (2016). On the predictability and error sources of tropical cyclone intensity forecasts. *J. Atmos. Sci.*, 73(9), 3739-3747.
- Fairall, C. W., Edson, J. B., & Miller, M. A. (1990). Heat fluxes, whitecaps, and sea spray, in *Surface Waves and Fluxes: Current Theory and Remote Sensing*, edited by G. Geernaert and W. Plant, 173–208, D. Reidel, Dordrecht, Netherlands.
- Fairall, C.W., Kepert, J.D., & Holland, G.H. (1994). The effect of sea spray on surface energy transports over the ocean. *Global Atmos. Ocean Syst.*, 2, 121-142.
- Fairall, C. W., Pezoa, S., Moran, K., & Wolfe, D. (2014). An observation of sea-spray microphysics by airborne Doppler radar. *Geophys. Res. Lett.*, 41(10), 3658-3665.
- Fenton J. D. (1985). A fifth-order Stokes theory for steady waves. *J. Waterw., Port. C-ASCE.*, 111, 216-234.
- Friedman, K. S., & Li, X. (2000). Monitoring hurricanes over the ocean with wide swath SAR. *J. Hopkins APL Tech. D.*, 21(1), 80-85.

- Fudeyasu, H., Ito, K., & Miyamoto, Y. (2018). Characteristics of tropical cyclone rapid intensification over the Western North Pacific. *J. Clim.*, 31(21), 8917-8930.
- Gade, M., & Alpers, W. (1999) Using ERS-2 SAR for routine observation of marine pollution in European coastal waters. *Sci. Total Environ.*, 237–238, 441–448.
- Gade, M., Byfield, V., Ermakov, S., Lavrova, O., and Mitnik, L. (2013). Slicks as Indicators for Marine Processes. *Oceanogr.*, 26 (2): 138–149.
- Gall, J. S., Frank, W. M., & Kwon, Y. (2008). Effects of sea spray on tropical cyclones simulated under idealized conditions. *Mon. Weather Rev.*, 136(5), 1686-1705.
- Goldenberg, S. B., & Shapiro, L. J. (1996). Physical mechanisms for the association of El Niño and West African rainfall with Atlantic major hurricane activity. *J. Clim.*, 9(6), 1169-1187.
- Gopalakrishnan, S. G., Goldenberg, S., Quirino, T., Zhang, X., Marks Jr, F., Yeh, K. S., & Tallapragada, V. (2012). Toward improving high-resolution numerical hurricane forecasting: Influence of model horizontal grid resolution, initialization, and physics. *Weather Forecast.*, 27(3), 647-666.
- Graham, S. (2019). “Aqua Earth-observing satellite mission”. *National Aeronautics and Space Administration*. <https://aqua.nasa.gov/>.
- Grodsky, S. *et al.* (2012). Haline hurricane wake in the Amazon/Orinoco plume: AQUARIUS/SACD and SMOS observations. *Geophys. Res. Lett.* 39.
- Hamza, S. B., Habli, S., Saïd, N. M., Bournot, H., & Le Palec, G. (2015). Numerical simulation of wave-structure interaction around an obstacle. In *Design and Modeling of Mechanical Systems-II* (pp. 683-691). Springer, Cham.
- Hirt, C.W., & Nichols, B.D. (1981). Volume of fluid (VOF) method for the dynamics of free boundaries. *J. Comput. Phys.*, 39(1), 201-225.
- Hoepffner, J., Blumenthal, R., Zaleski, S. (2011). Self-similar wave produced by local perturbation of the Kelvin-Helmholtz shear-layer instability. *Phys. Rev. Lett.*, 106, 104502-1– 104502-4.
- Holland, G. J., (1997). The Maximum Potential Intensity of Tropical Cyclones. *J. Atmos. Sci.*, 54, 2519–2541.
- Holthuijsen, L. H., Powell, M. D., & Pietrzak, J. D. (2012). Wind and waves in extreme hurricanes. *J. Geophys. Res. Oceans*, 117(C9).

- Jarosz, E., Mitchell, D. A., Wang, D. W., & Teague, W. J. (2007). Bottom-up determination of air-sea momentum exchange under a major tropical cyclone. *Science*, 315 (5819), 1707-1709.
- Jeong, D., Haus, B.K., & Donelan, M.A. (2012). Enthalpy transfer across the air-water interface in high winds including spray. *J. Atmos. Sci.*, 69, 2733–2748.
- Jessup, A. T., Zappa, C. J., & Yeh, H. (1997). Defining and quantifying microscale wave breaking with infrared imagery. *J. Geophys. Res. Oceans*, 102(C10), 23145-23153.
- Jiang, C., Liu, X., Yao, Y. & Deng, B. (2019). Numerical investigation of solitary wave interaction with a row of vertical slotted piles on a sloping beach. *Int. J. Nav. Archit. Ocean Eng.*, 11(1), 530-541.
- Jiang, H., & Ramirez, E. M. (2013). Necessary conditions for tropical cyclone rapid intensification as derived from 11 years of TRMM data. *J. Clim.*, 26(17), 6459-6470.
- Kao, H-Y., & Lagerloef, G.S.E. SMAP Sea Surface Salinity Validation and the Observations of the Plume of Hurricane Dorian. Ocean Sciences Meeting, 16-21 February 2020, San Diego, CA, USA. Abstract only (2020).
- Katsaros, K. B., Vachon, P. W., Liu, W. T., & Black, P. G. (2002). Microwave remote sensing of tropical cyclones from space. *J. Oceanogr.*, 58(1), 137-151.
- Katsir, Y., Goldstein, G. & Marmur, A. (2015). Bubble the wave or waive the bubble: Why seawater waves foam and freshwater waves do not? *Colloids Interface Sci. Commun.*, 6, 9.
- Kaplan, J., DeMaria, M., & J. A. Knaff, J. A. (2010). A revised tropical cyclone rapid intensification index for the Atlantic and Eastern North Pacific basins. *Weather Forecast.*, 25, 220–241.
- Keper, J. D. (1996). Comments on “The temperature of evaporating sea spray droplets.” *J. Atmos. Sci.*, 53, 1634–1641.
- Keper, J. D. (2018). The boundary layer dynamics of tropical cyclone rainbands. *J. Atmos. Sci.*, 75(11), 3777-3795.
- Keper, J., Fairall, C., & Bao, J. W. (1999). Modelling the interaction between the atmospheric boundary layer and evaporating sea spray droplets. In *Air-Sea Exchange: Physics, Chemistry and Dynamics*, 363-409.
- Kim, S. Y., Kim, K. M., Park, J. C., Jeon, G. M., & Chun, H. H. (2016). Numerical simulation of wave and current interaction with a fixed offshore substructure. *Int. J. Nav.*, 8(2), 188-197

- King, L., Roberts, I. J., Tinel, L., & Carpenter, L. J. (2019). The Determination of Surfactants at the Sea Surface. *Ocean Sci. Discuss.*, 1-30.
- Koga, M. (1981). Direct production of droplets from breaking wind-waves—its observation by a multi-colored overlapping exposure technique. *Tellus*, 33:552–563.
- Komori, S. *et al.* Laboratory measurements of heat transfer and drag coefficients at extremely high wind speeds. *J. Phys. Oceanogr.*, 48, 959–974 (2018).
- Kossin, J.S., Olander, T. L., & Knapp, K. R. (2013). Trend analysis with a new global record of tropical cyclone intensity. *J. Clim.*, 26, 9960-9976.
- Kulyakhtin, A., Shipilova, O., & Muskulus, M. (2014). Numerical simulation of droplet impingement and flow around a cylinder using RANS and LES models. *J. Fluid. Struct.*, 48, 280-294.
- Kurata, N., Vella, K., Hamilton, B., Shivji, M., Soloviev, A., Silvia, M., Tartar, A., & Perrie, W. (2016). Surfactant-associated bacteria in the near-surface layer of the ocean. *Sci. Rep.*, 6, 19123.
- Lee, W., Kim, S. H., Chu, P. S., Moon, I. J., & Soloviev, A. V. (2019). An index to better estimate tropical cyclone intensity change in the Western North Pacific. *Geophys. Res. Lett.*, 46(15), 8960-8968.
- Lehner, S., Horstmann, J., Koch, W., & Rosenthal, W. (1998). Mesoscale Wind Measurements Using Recalibrated ERS SAR Images. *J. Geophys. Res. Oceans*, 103 (C4): 7847–7856.
- Lighthill, J., G. Holland, W. Gray, C. Landsea, G. Craig, J. Evans, Y. Kurihara, & Guard, C. (1994). Global climate change and tropical cyclones. *Bull. Amer. Meteor. Soc.*, 75, 2147–2157.
- Lin, I. I., Black, P., Price, J. F., Yang, C. Y., Chen, S. S., Lien, C. C., & D'Asaro, E. A. (2013). An ocean coupling potential intensity index for tropical cyclones. *Geophys. Res. Lett.*, 40(9), 1878-1882.
- Lu, J., Lim. H., Liew, S.C., Bao, M., & Kwoh, L.K. (1999). Statistics in Southeast Asian waters compiled from ERS synthetic aperture radar imagery. *Earth Observation Quart.*, 621, 13–17.
- Lu, J., Kwoh, L.K., Lim, H., Liew, S.C., & Bao, M. (2000). Mapping oil pollution from space. *Backscatter*, 11, 23–26.
- Lukas, R., & Lindstrom, E. The mixed layer of the western equatorial Pacific Ocean. *J. Geophys. Res. Oceans*, 96(S01), 3343-3357 (1991).

- Maccherone, B. (2018). “MODIS”. *National Aeronautics and Space Administration*.
<https://modis.gsfc.nasa.gov/about/>.
- Malkus, J. S., & Riehl, H. (1960). On the dynamics and energy transformations in steady-state hurricanes. *Tellus*, 12(1), 1-20.
- Marks, F.D. (2003). Hurricanes. In *Encyclopedia of Atmospheric Sciences*, J. Holton, J. Pyle, and J. Curry (eds.). Elsevier Science Ltd., London, UK, 942-966.
- Masters, J. (2020). “The Most Reliable Hurricane Models, According to Their 2019 Performance.” *Yale Climate Connections*, Yale University.
- Mehta, S., Ortiz-Suslow, D. G., Smith, A. W., & Haus, B. K. (2019). A laboratory investigation of spume generation in high winds for fresh and seawater. *J. Geophys. Res. Atmos.*, 124(21), 11297-11312.
- Merrill, R. T. (1988). Environmental influences on hurricane intensification. *J. Atmos. Sci.*, 45, 1678–1687.
- Migliaccio, M., Nunziata, F., & Gambardella, A. (2009). On the copolarised phase difference for oil spill observation. *Int. J. Remote Sens.*, 30: 6, 1587-1602.
- Miles, J. W. (1959). On the generation of surface waves by shear flows. Part 3. Kelvin-Helmholtz instability. *J. Fluid Mech.*, 6, 583– 598.
- Miller, B. I. (1958). On the maximum intensity of hurricanes. *J. Meteor.*, 15, 184-195.
- Monahan, E.C., Fairall, C.W., Davidson, K.L., & Boyle, P.J. (1983). Observed inter-relations between 10 m winds, ocean whitecaps and marine aerosols. *Q. J. Roy. Meteor. Soc.* 109, 379-392.
- Moon, I. J., Ginis, I., Hara, T., & Thomas, B. (2007). A physics-based parameterization of air–sea momentum flux at high wind speeds and its impact on hurricane intensity predictions. *Mon. Weather Rev.*, 135(8), 2869-2878.
- Morsi, A.J. and Alexander, S.A. (1972) An Investigation of Particle Trajectories in Two-Phase Flow System. *J. Fluid Mech.*, 55, 193-208.
- Nayar, K. G., Panchanathan, D., McKinley, G. H., & Lienhard, J. H. (2014). Surface tension of seawater. *J. Phys. Chem. Ref. Data*, 43(4), 043103.
- NOAA (2020). What is the difference between a hurricane and a typhoon? National Ocean Service website, <https://oceanservice.noaa.gov/facts/cyclone.html>.
- Ortiz-Suslow, D. G., Haus, B. K., Mehta, S., & Laxague, N. J. (2016). Sea spray generation in very high winds. *J. Atmos. Sci.*, 73(10), 3975-3995.

- Parks, G. (2019). Microbial Analysis of Surfactant-Associated Bacteria in the Sea Surface Microlayer and Remote Sensing of Associated Slicks. *Int. J. Remote Sens.*, 41(10), 3886-3901.
- Perrie, W., Andreas, E. L., Zhang, W., Li, W., Gyakum, J., & McTaggart-Cowan, R. (2005). Sea spray impacts on intensifying midlatitude cyclones. *J. Atmos. Sci.*, 62, 1867–1883.
- Peng, T., & Richter, D. (2019). Sea spray and its feedback effects: Assessing bulk algorithms of air–sea heat fluxes via direct numerical simulations. *J. Phys. Oceanogr.*, 49(6), 1403-1421.
- Pielke, R. A., & Lee, T. J. (1991). Influence of sea spray and rainfall on the surface wind profile during conditions of strong wind. *Bound.-Layer Meteor.*, 55, 305–308.
- Powell, M. D., Vickery, P. J., & Reinhold, T. A. (2003). Reduced drag coefficient for high wind speeds in tropical cyclones. *Nature*, 422 (6929), 279-283.
- Price, J. F. (1981). Upper ocean response to a hurricane, *J. Phys. Oceanogr.*, 11, 153–175.
- Price, J. F., Morzel, J., and Niiler, P. P. (2008). Warming of SST in the cool wake of a moving hurricane, *J. Geophys. Res.*, 113, C07010, doi:10.1029/2007JC004393.
- Rappaport, E. N. (2014). Fatalities in the United States from Atlantic tropical cyclones: New data and interpretation. *Bull. Amer. Meteor.*, 95(3), 341-346.
- Rappaport, E. N., & Sheets, R. C. (1994). Hurricane Andrew. *Weather*, 49(2), 51-60.
- Rappaport, E. N., Franklin, J. L., Avila, L. A., Baig, S. R., Beven, J. L., Blake, E. S., & Landsea, C. W. (2009). Advances and challenges at the National Hurricane Center. *Weather Forecast.*, 24(2), 395-419.
- Richter, D. H., & Stern, D.P. Evidence of spray-mediated air-sea enthalpy flux within tropical cyclones. *Geophys. Res. Lett.*, 41, 2997–3003 (2014).
- Richter, D., & Sullivan, P. (2014) The sea spray contribution to sensible heat flux, *J. Atmos. Sci.*, 71, 640–654.
- Riehl, H. (1954). *Tropical Meteorology*. McGraw-Hill, 392 pp.
- Rogers, R. F., Aberson, S., Bell, M. M., Cecil, D. J., Doyle, J. D., Kimberlain, T. B., & Velden, C. (2017). Rewriting the tropical record books: The extraordinary intensification of Hurricane Patricia (2015). *Bulletin of the American Meteorological Society*, 98(10), 2091-2112.

- Roxy, M. K., Modi, A., Murtugudde, R., Valsala, V., Panickal, S., Prasanna Kumar, S., & Lévy, M. (2016). A reduction in marine primary productivity driven by rapid warming over the tropical Indian Ocean. *Geophys. Res. Lett.*, 43(2), 826-833.
- Shay, L. K., & Brewster, J. K. Oceanic heat content variability in the eastern Pacific Ocean for hurricane intensity forecasting. *Mon. Weather Rev.*, 138(6), 2110-2131 (2010).
- Shpund, J., Pinsky, M., & Khain, A. (2011). Microphysical structure of the marine boundary layer under strong wind and spray formation as seen from simulations using a 2D explicit microphysical model. Part II: The role of sea spray. *J. Atmos. Sci.*, 69, 3501-3514.
- Shpund, J., Khain, A., & Rosenfeld, D. Effects of sea spray on the dynamics and microphysics of an idealized tropical cyclone. *J. Atmos. Sci.*, 76(8), 2213-2234 (2019).
- Sigman, D. M. & Hain, M. P. (2012) The Biological Productivity of the Ocean. *Nature Education Knowledge* 3(10):21.
- Siddiqui, M. K., & Loewen, M. R. (2007). Characteristics of the wind drift layer and microscale breaking waves. *J. Fluid Mech.*, 573, 417-456.
- Siddiqui, M. K., Loewen, M. R., Richardson, C., Asher, W. E., & Jessup, A. T. (2001). Simultaneous particle image velocimetry and infrared imagery of microscale breaking waves. *Phys. Fluids*, 13(7), 1891-1903.
- Simpson, R. H. (1974) The Hurricane Disaster Potential Scale. *Weatherwise*, 27(169) 169-186.
- Sitkowski, M., & G. M. Barnes, 2009: Low-level thermodynamic, kinematic and reflectivity fields of Hurricane Guillermo (1997) during rapid intensification. *Mon. Weather Rev.*, 137, 645–663, <https://doi.org/10.1175/2008MWR2531.1>.
- Smith, R. K., & Montgomery, M. T. (2016). Understanding hurricanes. *Weather*, 71(9), 219-223.
- Soloviev, A. V., Lukas, R., Donelan, M. A., Haus, B. K., & Ginis, I. (2017). Is the state of the air-sea interface a factor in rapid intensification and rapid decline of tropical cyclones? *J. Geophys. Res. Oceans*, 122(12), 10174-10183.
- Soloviev, A. V. & Lukas R. (2010). Effects of Bubbles and Sea Spray on Air–Sea Exchange in Hurricane Conditions. *Bound.-Lay. Meteorol.*, 136, 365-376.
- Soloviev, A., & Lukas, R. (2014). *The near-surface layer of the ocean: structure, dynamics and applications* (Vol. 48). Springer Science & Business Media.
- Soloviev, A. V., Lukas, R., Donelan, M. A., Haus, Brian K., & Ginis, I. (2014). The air-sea interface and surface stress under tropical cyclones. *Sci. Rep.*, 4, 5306.

- Soloviev, A., Matt, S., Gilman, M., Hühnerfuss, H., Haus, B., Jeong, D., Savelyev, I., & Donelan, M. (2011). Modification of turbulence at the air-sea interface due to the presence of surfactants and implications for gas exchange. Part I: laboratory experiment. In: *Gas transfer at water surfaces*. Kyoto University Press, 245–258.
- Spiel, D.E. (1997). More on the births of jet drops from bubbles bursting on seawater surfaces. *J. Geophys. Res.*102, 5815-5821.
- Spiel, D.E. (1998). On the birth of film drops from bubbles bursting on seawater surfaces. *J. Geophys. Res.*103, 24,907-24,918.
- Stewart, R. (2002). *Introduction to Physical Oceanography*.
- Thorpe, S.A. (1986). Bubble clouds: A review of their detection by sonar, of realistic models, and of how may be determined. *Whitecaps and Their Role in Air-Sea Exchange Processes*. E.C. Monahan and G. MacNiocaill, Eds., 57-68, D. Reidel, Norwell, MA.
- Tory, K. J., Montgomery, M. T., & Davidson, N. E. (2006). Prediction and diagnosis of tropical cyclone formation in an NWP system. Part I: The critical role of vortex enhancement in deep convection. *J. Atmos. Sci.*, 63(12), 3077-3090.
- Troitskaya, Y., Kandaurov, A., Ermakova, O., Kozlov, D., Sergeev, D., & Zilitinkevich, S. (2017). Bag-breakup fragmentation as the dominant mechanism of sea-spray production in high winds. *Sci. Rep.*, 7, 1614.
- Tsai, W. T., & Liu, K. K. (2003). An assessment of the effect of sea surface surfactant on global atmosphere-ocean CO₂ flux. *J. Geophys. Res. Oceans*, 108(C4).
- Uang, C.L. (1999). Impacts of sea spray and oceanic response on the development of tropical cyclones. Preprints, 23rd Conf. on Hurricanes and Tropical Meteorology, Dallas, TX, *Amer. Meteor. Soc.*, 30–31.
- Uddin, M. N., Atkinson, M., & Opoku, F. (2020). A Computational Fluid Dynamics Investigation of a Numerically Simulated Wave Tank. *American Journal of Mechanical Engineering*, 8(1), 40-49.
- Velotto, D., Nunziata, F., Migliaccio, M., & Lehner, S. (2013). Dual-polarimetric TerraSAR-X SAR data for target at sea observation. *IEEE Geosci. Remote S.*, 10: 5, 1114-1118.
- Veron, F., Hopkins, C., Harrison, E. L., & Mueller, J. A. (2012). Sea spray spume droplet production in high wind speeds. *Geophys. Res. Lett.* 39.16.
- Vigh, J. L., Knaff, J. A., & Schubert, W. H. (2012). A climatology of hurricane eye formation. *Mon. Weather Rev.*, 140(5), 1405-1426.

- Wahl, T., Skøelv, Å., Pedersen, J. P., Seljelv, L. G., Andersen, J. H., Follum, O. A., & Hamnes, H. (1996). Radar satellites: A new tool for pollution monitoring in coastal waters. *Coastal Management*, 24(1), 61-71.
- Walker, N. D., Leben, R. R., & Balasubramanian, S. (2005). Hurricane-forced upwelling and chlorophyll a enhancement within cold-core cyclones in the Gulf of Mexico, *Geophys. Res. Lett.*, 32, L18610, doi:10.1029/2005GL023716.
- Wang, Y., Kepert, J. D., & Holland, G. J. (1999). The impact of sea spray evaporation on tropical cyclone intensification. Preprints, 23rd Conf. on Hurricanes and Tropical Meteorology, Dallas, TX, *Amer. Meteor. Soc.*, 26–29.
- Wu, J., (1973) Spray in the atmospheric surface layer: Laboratory study. *J. Geophys. Res.*, 78, 511–519.
- Wu, J., (1981) Evidence of sea spray produced by bursting bubbles. *Science*, 212, 324–326.
- Wurl, O., Wurl, E., Miller, L., Johnson, K., & Vagle, S. (2011). Formation and global distribution of sea surface microlayers. *Biogeosciences*, 8(1), 121-135.
- Wurl, O., Ekau, W., Landing, W. M., & Zappa, C. J. (2017). Sea surface microlayer in a changing ocean—A perspective. *Elem Sci Anth*, 5.
- Yau, M. K., Liu, Y., Zhang, D. L., & Chen, Y. (2004). A multiscale numerical study of Hurricane Andrew (1992). Part VI: Small-scale inner-core structures and wind streaks. *Mon. Weather Rev.*, 132(6), 1410-1433.
- Zhang, J. A., Black, P. G., French, J. R., & Drennan, W. M. First direct measurements of enthalpy flux in the hurricane boundary layer: The CBLAST results. *Geophys. Res. Lett.*, 35, L14813 (2008).
- Zhang, B., & Perrie, W. (2012). Cross-polarized synthetic aperture radar: A new potential measurement technique for hurricanes. *Bull. Amer. Meteor. Soc.*, 93(4), 531-541.
- Zhang, Y., Li, Y., & Lin, H. (2017). Chapter 2 Oil-Spill Pollution Remote Sensing by Synthetic Aperture Radar.
- Zutic, V., Cosovic, B., Marcenko, E., Bihari, N., & Krsinic, F. (1979). Surfactant production by marine phytoplankton. Field observations and laboratory culture experiments. *Rapports et Proces-Verbaux des Reunions-Commission Internationale pour l'Exploration Scientifique de la Mer Mediterranee (CIESM)*.
- Zhang, X., Simons, R., & Buldakov, E. (2016). A numerical study of wave-current interaction in the bottom boundary layer. In *Proceedings of 35th International Conference on Coastal Engineering* (Vol. 35). Coastal Engineering Proceedings.

9. Supplementary Material

Supplementary data available upon request.